Advances in PET

The Latest in Instrumentation, Technology, and Clinical Practice

Jun Zhang
Michael V. Knopp
Editors

Springer

Advances in PET

Jun Zhang • Michael V. Knopp
Editors

Advances in PET

The Latest in Instrumentation, Technology, and Clinical Practice

Springer

Editors
Jun Zhang
Department of Radiology
The Ohio State University
Columbus, OH
USA

Michael V. Knopp
Department of Radiology
The Ohio State University
Columbus, OH
USA

ISBN 978-3-030-43039-9 ISBN 978-3-030-43040-5 (eBook)
https://doi.org/10.1007/978-3-030-43040-5

This Springer imprint is published by the registered company Springer Nature Switzerland AG
The registered company address is: Gewerbestrasse 11, 6330 Cham, Switzerland

Preface

First and foremost, I sincerely welcome and greatly appreciate Dr. Suleman Surti and Dr. Joel S. Karp (Chaps. 1 and 7), Dr. Daniel A. Pryma (Chap. 2), Dr. Dennis R. Schaart (Chap. 3), Dr. David F.C. Hsu and Dr. Craig S. Levin (Chap. 4), Dr. Jun Zhang and Dr. Michael V. Knopp (Chap. 5), and Dr. Michael E. Casey and Dr. Dustin Osborne (Chap. 6) for their coauthorship and contribution to the first edition of this book.

For decades, researchers have been interested in replacing photomultiplier tubes with semiconductor photosensors. With the disruptive technology leap of solid state PET detectors, improvements in PET equipment are happening at a staggering pace in both PET/CT and PET/MRI. For the first time, clinical PET scanners have reached 200–400 ps for time-of-flight timing resolution, 3 mm for spatial resolution, and >20 cps/kBq for sensitivity. Research into innovative PET technologies, methodologies, and clinical practice is expanding, with the potentials of enabling better PET image quality, reduced PET dose, and accelerated PET scans.

This book is a guide to new and emerging PET technology, instrumentation, and its place in clinical practice to discover potential values of solid state PET and promote the growth of PET imaging. It is primarily addressed to medical physicists, nuclear medicine physicians, and technologists who wish to learn and acquire knowledge of solid state digital PET imaging including silicon photomultiplier-based PET detector technology, system characteristics and performance, as well as clinical practices. The basic principles of PET physics with elementary concepts are not dedicatedly described in this book.

We have tried to write the book in a concise and logical manner. It is organized into three categories: I. the basics of PET imaging, which focuses on the current status and future direction of PET technology and clinical practice (Chaps. 1 and 2); II. solid state digital PET instrumentation, technology, and clinical practice, which focuses on both the fundamentals of silicon photomultipliers for time-of-flight PET (Chap. 3) and the evaluation of emerging PET instrumentation and technologies across manufactures (Chaps. 4, 5, and 6); III. future prospective of PET/CT imaging, focusing on the EXPLORER family's long axial field-of-view total-body PET instrumentation and technologies (Chap. 7).

We believe that it is a new era for PET imaging. The new-generation solid state PET instrumentation and technologies have brought exciting times also evolving challenges to PET imaging. It has created new initiatives and opportunities in

low-dose PET, fast PET imaging, better lesion detectability, optimal imaging performance, novel tracer applications, as well as whole-body dynamic scans, which could revolutionize our understanding and treatment of disease through overall improved technologies and experiences.

In the end, it is a team's work. It has been my great pleasure and privilege to work together with all the coauthoring professionals in writing this book. A sincere appreciation to Dr. Michael V. Knopp for his great help and support to me in providing the solid state PET platform and fulfilling the book as the coeditor. A great and special appreciation to Dr. Joel S. Karp and Dr. Suleman Surti for their professional guidance and meaningful suggestions to me in the book design and write-ups. I am indebted to many of my peers and colleagues: Dr. Timothy Turkington, Dr. Nathan C. Hall, Dr. Osama Mawlawi, Dr. David Hintenlang, Dr. Mona Natwa, and more for their inspiration and support to me. Taking this opportunity, we are very grateful to Ms. Margaret Moore, Ms. Marie Felina, Ms. Kayalvizhi Eswaran, Mr. Prakash Marudhu, and other publishing staff of Springer for their various help and cooperation in bringing our labor to fruition.

To my wife, Zhaoxia, and my daughters, Grace and Rachel, with love and appreciation.

Columbus, OH, USA Jun Zhang

Contents

Contributors

Michael E. Casey, PhD Siemens Medical Solutions, Knoxville, TN, USA
University of Tennessee Graduate School of Medicine, Knoxville, TN, USA

David F. C. Hsu, PhD Electrical Engineering and Radiology at Stanford University, Stanford, CA, USA

Joel S. Karp, PhD University of Pennsylvania, Philadelphia, PA, USA

Michael V. Knopp, MD, PhD The Ohio State University, Columbus, OH, USA

Craig S. Levin, PhD Radiology/Physics/Electrical Engineering/Bioengineering at Stanford University, Stanford, CA, USA

Dustin R. Osborne, PhD, DABSNM Siemens Medical Solutions, Knoxville, TN, USA
University of Tennessee Graduate School of Medicine, Knoxville, TN, USA

Daniel A. Pryma, MD Perelman School of Medicine at the University of Pennsylvania, Philadelphia, PA, USA

Dennis R. Schaart, PhD Delft University of Technology, Radiation Science & Technology Department, Delft, The Netherlands

Suleman Surti, PhD University of Pennsylvania, Philadelphia, PA, USA

Jun Zhang, PhD The Ohio State University, Columbus, OH, USA

Abbreviations

APD	Avalanche photodiode
CQIE	Center for Quantitative Imaging Excellence
cPET	Conventional PET
CS	Compton scattering
DCR	Dark count rate
DOI	Depth of interaction
DPC	Digital photon counting
dPET	Digital PET
dSiPM	Digital silicon photomultiplier
FDG	18F-fluorodeoxyglucose
FOV	Field of view
FWHM	Full width at half maximum
FWTM	Full width at tenth maximum
HD	High definition
LOR	Line of response
Lu	Lutetium
LYSO	Lutetium-yttrium oxyorthosilicate
ML-EM	Maximum likelihood expectation maximization
MOS	Metal oxide semiconductor
NEC	Noise equivalent count
NECR	Noise equivalent count rate
NEMA	National Electrical Manufacturers Association
OS-EM	Ordered subsets expectation maximization
PDE	Photon detection efficiency
PDPC	Philips Digital Photon Counting
PE	Photoelectric absorption
PMT	Photomultiplier tube
PSF	Point spread function
PVE	Partial volume effect
QC	Quality check
RC	Recovery coefficient
SBR	Sphere-to-background ratio
SD	Standard definition
SiPM	Silicon photomultiplier

SNR	Signal-to-noise ratio
SPAD	Single-photon avalanche diode
SUV	Standardized uptake value
TDC	Time-to-digital converter
TOF	Time of flight
TSV	Through-silicon vias
UHD	Ultrahigh definition

Part I

Basics Science of Positron Emission Tomography

Current Status of PET Technology

1

Suleman Surti and Joel S. Karp

1.1 Introduction

In recent years, PET/CT imaging has played an important clinical role as a molecular imaging tool for diagnosis and staging of cancer in patients [1]. Used predominantly with ^{18}F-fluorodeoxyglucose (FDG) as the radiotracer that acts as a glucose analog, PET/CT has significantly influenced the management of cancer patients [2, 3] and is reimbursed for initial and follow-up imaging of most cancer types [4]. In addition, PET has also been shown to play an important role in guiding cancer treatment by characterizing the tumor biology as well as monitoring tumor response to therapy [1, 5]. A more thorough overview of the current status in clinical practice is given in Chap. 2. Modern time-of-flight (TOF) PET scanners provide sufficient sensitivity and signal-to-noise ratio (SNR) performance so that clinical FDG scans with excellent diagnostic quality can be completed in 10–15 min using bed translation to cover a patient from "eyes to thighs."

Beyond FDG, there are other tracers coming into more widespread use that have very different imaging characteristics. Some of these tracers have lower photon flux because of lower dose (^{68}Ga-labelled) and/or low positron emission branching fraction (^{89}Zr-labelled or ^{124}I-labelled), requiring increased PET system sensitivity to achieve reliable quantitative images especially for dose calibration. In addition, the quantitative performance of images from some of these tracers (e.g., ^{89}Zr-labelled or ^{124}I-labelled) will also require corrections for coincidence data acquired in the presence of additional single photons. Finally, increased positron energy will require improvements in the point spread function (PSF) model used during image reconstruction to better account for the increased range of the positrons for some of these non-^{18}F-labelled tracers. Hence, while modern PET

S. Surti (✉) · J. S. Karp
University of Pennsylvania, Philadelphia, PA, USA
e-mail: surti@pennmedicine.upenn.edu; joelkarp@pennmedicine.upenn.edu

J. Zhang, M. V. Knopp (eds.), *Advances in PET*,
https://doi.org/10.1007/978-3-030-43040-5_1

scanners may provide excellent quality and quantitative FDG images, moving PET in new areas requires continued technical improvements and capabilities.

1.2 Current Status of TOF PET/CT Scanners

TOF PET scanners were originally developed in the early 1980s [6–11] when the primary application was in brain and cardiac imaging using compounds tagged with short-lived radioisotopes, such as ^{15}O-water, ^{11}C-acetate, and ^{82}Rb. While providing good timing resolution as well as reduced dead time, the primary limitations of these systems were lower sensitivity due to the use of interplane septa for 2D imaging and poor spatial resolution arising due to the choice of scintillator and photosensor. With the development of new scintillators in the late 1990s and early 2000s, a new generation of TOF PET scanners, now all PET/CT, was introduced in the mid-2000s. These scanners were optimized for the primary application of detection and staging of cancer using ^{18}F-FDG. In addition to providing good system timing resolution and spatial resolution, these scanners overcame the limitations of low sensitivity by enabling fully 3D imaging (no interplane septa). All of these scanners use lutetium-based scintillators (LSO and LYSO) and utilize light-sharing detectors to achieve high spatial resolution (4–5 mm) with photomultiplier tubes (PMTs) of 25–39 mm size. Due to the detector design, the coincidence timing resolution of these scanners lies within the range of 450–600 ps – very similar to the scanners developed in the 1980s but with superior spatial resolution and sensitivity. Recent years have seen an introduction of a new solid-state-based photosensor (silicon photomultiplier, or SiPM) that provides excellent intrinsic timing performance on par or better than the conventional PMTs while providing flexibility in detector size that is not available with PMTs. This has led to the commercial development of a new generation of "digital" PET scanners using SiPM arrays with reduced or almost no light sharing in the detector design. These new scanners have much improved system coincidence timing resolution (210–390 ps) with similar or improved spatial resolution through the use of smaller crystals. The benefits of TOF for clinical imaging were well established [12–18], and so it is expected that improved TOF resolution will increase these benefits, particularly for patients with larger body mass index (BMI).

1.3 Hardware Design

1.3.1 Scintillator

As mentioned earlier, lutetium-based scintillators are currently being used in all modern commercial whole-body TOF PET scanners. This choice is driven by the combination of high stopping power, high light output, and fast decay time of these scintillators which leads to high system sensitivity as well as very good energy and spatial and timing resolutions – all necessary characteristics for a modern fully 3D

TOF PET system [19–21]. The two scintillators used most commonly are closely related: cerium-doped lutetium oxy-orthosilicate (Lu_2SiO_5(Ce) or LSO(Ce)) and lutetium-yttrium oxy-orthosilicate ($Lu_{1.8}Y_{0.2}SiO_5$(Ce) or LYSO(Ce)). In the early to mid-1990s, LSO(Ce), usually referred to as LSO, was first developed and introduced as a PET scintillator [22] as a replacement for BGO. At the time BGO was the primary scintillator being used in commercial PET but had limitations due to its poor light output and long decay time – less than ideal properties for fully 3D PET in comparison with NaI(Tl), which was also in use commercially [19]. While LSO was first used in a small animal PET scanner [23] and subsequently incorporated into a brain [24, 25] and a whole-body PET scanner [26], it was later recognized that it also had very good timing resolution that could be used in the development of TOF PET scanners [20, 21]. Following a similar trajectory, LYSO was first utilized in a dedicated small animal PET scanner [27] and subsequently used in the production of a new generation of commercial TOF PET/CT system [28]. While the current version of the Lu-based scintillators all uses varying levels of Ce doping, there have been efforts to change the dopant in order to achieve improved performance. For instance, a co-doped version of LSO using calcium has been developed with increased light output and shorter decay time than the LSO(Ce) scintillator [29], leading to further improvements in timing resolution [30]. Similarly, calcium and magnesium co-doped versions of LYSO have also been reported to produce higher light output than cerium-doped LYSO [31], implying improved timing performance. Thus, there is potential for improved lutetium-based scintillators that could be a direct replacement for the current versions of commercially used LSO and LYSO.

While BGO is relatively inexpensive and was a preferred PET scintillator prior to the development of LSO, the slow time scale of the luminescence process made it impossible to use it for TOF PET. However, it has been noted that the passage of charged electrons produced within BGO by the annihilation photons leads to the emission of Cherenkov light that can be detected by the SiPM devices (high quantum efficiency) [32]. The time scale of Cherenkov emission is very fast leading to a very fast signal and potential for fast timing resolution that is appropriate for TOF PET [33]. Several studies have been performed recently [34, 35] with best results indicating a coincidence timing resolution as good as 330 ps (FWHM) can be achieved with a 20-mm-long crystal [34]. However, the light output from Cherenkov emission is very low; thus, it is still necessary to utilize the (slower) scintillation light to determine both energy and spatial localization of the gamma interaction, and it remains to be seen how practical it is to use Cherenkov timing for TOF PET imaging with BGO.

1.3.2 Photosensor

Since the development of early PET scanners, PMTs have been the photosensor of choice for all clinical systems. The high gain and consequently high signal-to-noise ratio of the PMT signal lead to very good energy resolution, and plano-concave photocathodes combined with careful dynode design have made it possible to

achieve very fast timing with cost-effective PMTs in sizes suitable (25–39 mm diameter) to combine with multi-crystal PET detector arrays. The development of new super and ultra bialkali, plano-concave photocathodes with increased quantum efficiency (QE) and improved dynode structure to improve signal rise time has led to further improvements in the timing resolution achieved with PMTs. Single-channel PMTs have been the standard in PET systems where a light-sharing method is used to achieve spatial resolution significantly better than the PMT size. In addition to new photocathode materials, new fabrication methods have led to the development of fast multi-anode PMTs where a single photocathode is shared by several small anodes in a single PMT package. A fairly common multi-anode PMT design has a 5 × 5 cm^2 cross section with an 8 × 8 or 16 × 16 array of anodes for readout (Fig. 1.1). These PMTs provide additional flexibility in developing fast PET detectors with minimal light sharing to achieve high detector spatial resolution; however, their complex design makes them considerably more expensive than the single-channel PMT.

The last 15–20 years has seen the introduction of a new solid-state photosensor (SiPM) that is compact and fast, has high gain and low noise, and is insensitive to magnetic fields [36–40]. Although this technology was initially expensive, the cost has decreased as the devices become more widely used. Details about SiPM technology are discussed later in Chaps. 3–6.

Since SiPM devices can be fabricated in small sizes, as opposed to PMTs, they provide great flexibility in developing high-resolution PET detectors. They also operate at low bias voltage (few tens of volts) as opposed to PMTs (about thousand volts), and being solid-state technology can be made nonmagnetic that is necessary for PET/MR scanners that incorporate a PET detector ring inside the magnet bore

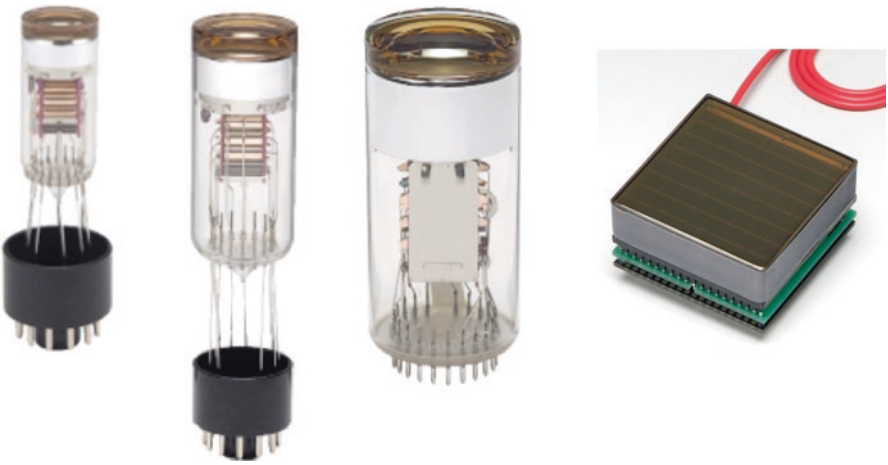

Fig. 1.1 From left to right, pictures of 25 mm diameter (R9800), 38 mm diameter (R9420), and 51 mm diameter (R7724) single-channel PMTs and a 64-channel H8500 MAPMT. All PMTs are manufactured by Hamamatsu. The H8500 is 5 × 5 cm^2 in size and the individual anodes are about 6.25 × 6.35 mm^2. (Images courtesy of Hamamatsu)

to enable simultaneous PET and MR scanning. Additional work to further improve the performance of SiPMs is ongoing, ranging from increase in photon detection efficiency (PDE) due to increased microcell density and quantum efficiency, as well as the development of 3D digital SiPMs (wafer-level integration of the SiPM and readout electronics). While the current version of digital SiPM technology [41, 42] has increased the flexibility and performance to some degree, there are some limitations in this design. For instance, a single time-to-digital converter (TDC) is used to obtain timing information for one or more SiPM channels. However, there is a timing skew attached to the signal from each microcell based on its location within the SiPM channel that leads to a degradation of the timing performance of the SiPM channel due to the use of a common TDC. One aspect of 3D digital SiPM development work is to fabricate a dedicated TDC for each microcell within a SiPM channel that will likely lead to a device with significantly improved intrinsic timing performance. Early SiPM devices were a few millimeters in size, but recent fabrication techniques have led to the development of larger arrays of these devices that are suitable for use in modern PET scanners by coupling to comparably sized scintillator arrays. Early SiPM arrays were fabricated using discrete SiPM devices connected via bond wires on a common printed circuit board that led to relatively large dead areas between each SiPM channel and hence a lower device PDE. More recent developments have led to the production of SiPM arrays using through-silicon vias (TSV) technology to interconnect the individual SiPM channels and significantly reduce the dead area due to classical wire bonding. An ideal solution will be to fabricate the entire SiPM array on common wafer to produce what are called monolithic arrays. However, a disadvantage of this method is that fabrication errors could lead to large variations in performance of individual channels on the device leading to suboptimal performance – a limitation that is not present in the discrete arrays where each channel can be chosen to provide a uniform performance.

1.3.3 Detector Design

The properties of the chosen scintillator and photosensor define the best intrinsic performance that can be achieved by the PET detector. In particular, the crystal size determines the detector spatial resolution (cross section) and sensitivity (thickness) as well as light output that in turn affects the detector energy and timing resolution. Standard commercial PET detectors have used Lu-based crystals that are 4–5 mm wide and 18–25 mm thick. Until the recent advent of SiPM, PET detectors were comprised of rectangular crystal arrays coupled to large PMTs (25–39 mm in diameter) via a light-sharing technique such as that utilized in block detectors [43], quadrant sharing block detectors [44], or the pixelated Anger-logic detectors [45] (see examples in Fig. 1.2). These types of detector designs are still in use in modern PET/CT systems from all major manufacturers [46–49]. While all of these systems provide very good overall performance, their TOF performance (coincidence timing resolution in the range of 400–550 ps) is limited due to the practical choices made in the detector design: light loss and transit time dispersion of scintillation photons

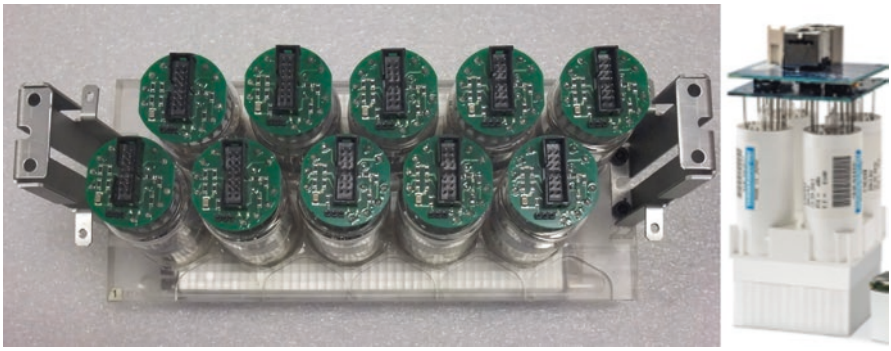

Fig. 1.2 Picture of a single detector module from a Philips Gemini TF scanner using a pixelated Anger-logic detector design (left) and a Siemens Biograph mCT scanner using a block detector. The Gemini TF (and newer Ingenuity TF) detector consists of a 23 × 44 array of 4 × 4 × 22 mm^3 LYSO crystals coupled to a hexagonal array of 39-mm-diameter single-channel PMTs. The open crystal area visible along the lower edge of the detector module would be read out with another row of PMTs that are not shown here which will straddle this and the neighboring module to form a continuous detector ring in the scanner. The mCT detector consists of a 13 × 13 array of 4 × 4 × 20 mm^3 LSO crystals coupled to a 2 × 2 square array of 25-mm-diameter single-channel PMTs. Compared to the Gemini TF detector, each mCT detector is completely independent of neighboring detector modules. (Pictures courtesy of Philips Healthcare and Siemens Healthineers)

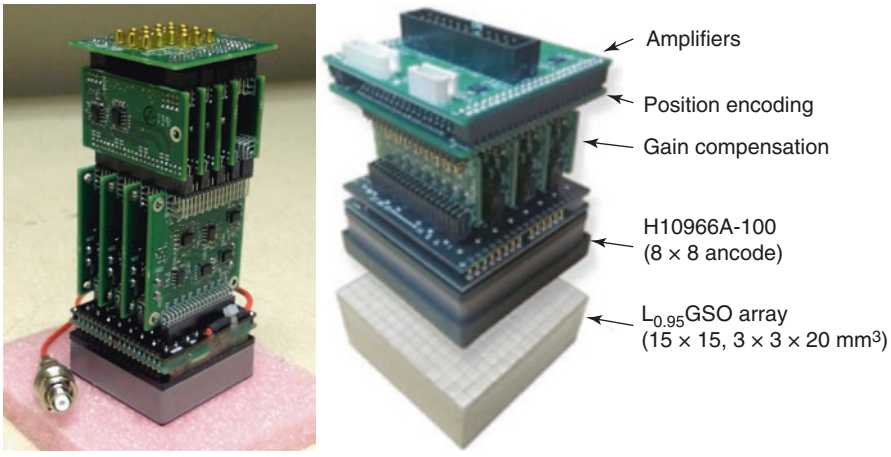

Fig. 1.3 Pictures of two multi-anode PMT-based PET detectors used in a dedicated breast imaging PET/tomosynthesis system under development at the University of Pennsylvania and a research whole-body PET scanner. The detector on the left uses a 32 × 32 array of 1.5 × 1.5 × 15 mm^3 LYSO crystals, while the one on the right uses a 15 × 15 array of 3 × 3 × 20 mm^3 LGSO crystals. (The figures are reprinted with permission from [51] (left) and [52] (right))

as they undergo multiple reflections within a long, narrow crystal [20] and the degrading effects due to the light-sharing mechanism of these PMT-based detectors [50]. Some of these limitations can be mitigated with the use of multi-anode PMTs (MAPMT) that require minimal or no light sharing due to small size of the individual anodes (Fig. 1.3) [51]. As shown in Fig. 1.3, one can also appreciate the

significant overhead of associated electronics per detector, although a commercial implementation would reduce the size of this prototype design. Nevertheless, a complete prototype TOF PET system has been recently developed with these electronics incorporated and with coincidence timing resolution of 340 ps [52]. A bigger drawback of MAPMT-based detectors is that the cost of the MAPMTs is significantly high compared to single-channel PMTs. The advent of SiPM arrays with cost approaching that of single-channel PMTs per unit detector area has therefore made the use of MAPMTs in TOF PET scanners less likely since they are not cost-effective with the existing technology. Compared to the multi-anode PMTs, SiPM arrays also present a more flexible and practical alternative to achieving excellent detector performance. For SiPM arrays, all the electronics as shown in Fig. 1.3 can be replaced by developing a dedicated ASIC where all the electronics are placed on a chip. While this can be a very costly development, it is easy to make copies for use with multiple detectors. Alternately, for the digital SiPM array from Philips (Philips Digital Photon Counter, or PDPC), most of the event processing is done in a field-programmable gate arrays (FPGA). While the ideal detector design will match each SiPM channel to a single crystal (Fig. 1.4), commercial detectors using some light sharing have already shown excellent overall performance. Commercial, digital PET/CT using SiPM devices is already available from the major manufacturer providing coincidence timing resolution of the PET system in the range of 210–390 ps.

In the future, new detectors with improved scintillators or photosensors promise additional improvements. For instance, 22-mm-thick LYSO scintillators 1-1 coupled to a new generation of SiPMs with improved PDE have shown benchtop measurements of <150 ps coincidence timing resolution [53]. A commercial PET scanner comprises tens of thousands of individual crystals, and a similar number of

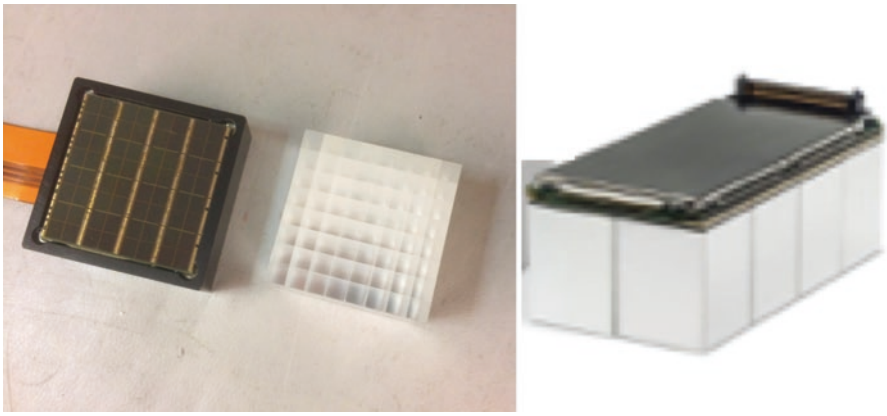

Fig. 1.4 (Left) Picture of PDPC digital SiPM array (8 × 8 array, 3.6 cm × 3.6 cm) placed next to an 8 × 8 array of LYSO crystals. The LYSO crystal cross section is matched to individual channels of the PDPC array, and 360 of such detector arrays are used in the complete Philips Vereos PET/CT scanner. (Right) A 4 × 2 array (6.4 cm × 3.2 cm) of mini-blocks configured as a detector in the Siemens Biograph Vision PET/CT scanner (a total of 304 detectors are present in the scanner). Each mini-block consists of a 4 × 4 channel (1.6 cm × 1.6 cm) SiPM array coupled to a 5 × 5 array of LSO crystals. A dedicated ASIC array is coupled to the top (back of SiPM array) in the Siemens detector. (Pictures courtesy of Philips Healthcare and Siemens Healthineers)

electronic channels (including TDCs) will be needed in a 1-1 coupled detector design. Even if some signal multiplexing is utilized, the number of electronic channels is still very large, requiring careful calibrations in order to maintain the benchtop performance. An intriguing option is the use of a single monolithic scintillation detector instead of an array of long, narrow crystals coupled to a SiPM array. These detectors reduce or remove the degrading effect of multiple reflections of scintillation photons within a long, narrow crystal while also simplifying the need for assembling large crystal arrays and show great promise in achieving both good spatial resolution with depth-of-interaction (DOI) measurement and timing resolution [54, 55]. Recent work has shown that spatial resolution of <1.5 mm (FWHM) and coincidence timing resolution of <150 ps can be achieved in such a detector design with crystals similar in thickness to those used commercially (~2 cm) [56]. While the spatial resolution at the FWHM level is the best reported value for detectors of this thickness, the spatial response is non-Gaussian with long tails suggesting that imaging performance will be somewhat compromised relative to a detector achieving similar FWHM with a Gaussian response function. A potential drawback is the need for significant detector calibrations and the complexity of position and timing estimation algorithm. Despite these limitations, these measurements demonstrate potential for further improvement in performance of full systems. It is notable that a PET scanner based on 8-mm-thick monolithic detectors is commercially available for small animal imaging [50]. This system provides very high spatial resolution with DOI correction that allows a PET scanner with a small diameter detector ring to achieve uniform spatial resolution of ~ 1 mm throughout the imaging field of view.

1.4 Software Algorithms

In the last two decades, significant progress has been made in the implementation of statistical ordered subset expectation maximization (OS-EM) algorithms for routine use in clinical PET. Compared to analytical algorithms, these provide better noise characteristics in the image, which is especially relevant for the lower sensitivity of clinical PET scanners. The advent of new TOF PET scanners in the mid- to late 2000s led to an extension of these algorithms to TOF-assisted OS-EM algorithms where each collected event along an LOR is back-projected over a limited LOR length (determined by the TOF difference of the coincident photons and the system timing resolution) instead of its entire extent within the patient or imaging object leading to reduced noise propagation during image reconstruction [57, 58]. Regularization techniques can lead to a further reduction in reconstructed image noise [59] and have been implemented commercially. While noise reduction is an important component of optimizing image quality, it is also important to maintain quantitative accuracy with these techniques. Spatial resolution modeling (also referred to as PSF modeling) within the reconstruction algorithm can also improve image quality since it corrects for degrading effects, such as detector resolution, positron range, and parallax error, and effectively leads to improved spatial

resolution in the reconstructed images [60, 61]. Finally, joint estimation of emission and attenuation images has been investigated for many years [62], with an eye toward avoiding the use of the CT images for attenuation correction. For non-TOF PET data, this approach does not provide robust results, since the cross talk between the two reconstructions makes it impossible to uniquely determine both attenuation and emission distributions independently. With TOF information, simultaneous attenuation-emission reconstruction approaches have been revisited [63] with great promise [62, 64, 65]. Although there is still a need for a relative scaling of the emission and transmission reconstructions, the cross talk between them is significantly reduced by incorporating the TOF information into the joint estimation. While it is unlikely that PET will be used routinely without CT for clinical purposes, there are situations that would benefit from being able to provide quantitative images without the radiation dose from the CT, such as pediatric imaging.

1.5 Conclusion

The last 20 years has seen significant improvements in PET instrumentation leading to greatly enhanced imaging performance. These improvements have been driven by technological hardware advancements beginning with improved scintillator characteristics and new photosensors leading to new digital detector designs using primarily SiPMs. A consequence of these advancements has been an improvement in intrinsic system sensitivity while acquiring data exclusively in fully 3D mode and a commercial implementation of TOF imaging with both PET/CT and PET/MR systems. In parallel, software developments utilizing the advantages of improved or expanded information present in PET data have led to image reconstruction methods that lead to greatly improved signal-to-noise ratio in the images. Consequently, routine clinical exams can be performed in <10 min while also opening new avenues for PET imaging utilizing either new radiotracers or using new imaging protocols.

References

1. Kircher MF, Hricak H, Larson SM. Molecular imaging for personalized cancer care. Mol Oncol. 2012;6(2):182–95.
2. Von Schulthess GK, Steinert HC, Hany TF. Integrated PET/CT: current applications and future directions. Radiology. 2006;238(2):405–22.
3. Juweid ME, Cheson BD. Positron-emission tomography and assessment of cancer therapy. N Engl J Med. 2006;354(5):496–507.
4. Buck AK, et al. Economic evaluation of PET and PET/CT in oncology: evidence and methodologic approaches. J Nucl Med. 2010;51(3):401–12.
5. Mankoff DA, et al. Development of companion diagnostics. Semin Nucl Med. 2016;46(1):47–56.
6. Ter-Pogossian MM, et al. PETT VI: a positron emission tomograph utilizing cesium fluoride scintillation detectors. J Comput Assist Tomogr. 1982;6:125–33.
7. Ter-Pogossian M, et al. Super PETT I: a positron emission tomograph utilizing photon time-of-flight information. IEEE Trans Med Imaging. 1982;M1-1(3):179–87.

8. Gariod R, et al. The "LETI" positron tomograph architecture and time-of-flight improvements. In: Proceedings of IEEE workshop on time-of-flight emission tomography. St. Louis: Washington University; 1982.
9. Wong WH, et al. Performance characteristics of the University of Texas TOF PET-I Camera. J Nucl Med. 1984;25(5):46–7.
10. Lewellen TK, et al. Performance measurements of the SP3000/UW time-of-flight positron emission tomograph. IEEE Trans Nucl Sci. 1988;35(1):665–9.
11. Mazoyer B, et al. Physical characteristics of TTV03, a new high spatial resolution time-of-flight positron tomograph. IEEE Trans Nucl Sci. 1990;37(2):778–82.
12. Daube-Witherspoon ME, et al. Determination of accuracy and precision of lesion uptake measurements in human subjects with time-of-flight PET. J Nucl Med. 2014;55:602–7.
13. Karp JS, et al. Benefit of time-of-flight in PET: experimental and clinical results. J Nucl Med. 2008;49(3):462–70.
14. Surti S, et al. Impact of TOF PET on whole-body oncologic studies: a human observer detection and localization study. J Nucl Med. 2011;52:712–9.
15. Conti M. Why is TOF PET reconstruction a more robust method in the presence of inconsistent data? Phys Med Biol. 2011;56:155–68.
16. Kadrmas DJ, et al. Impact of time-of-flight on PET tumor detection. J Nucl Med. 2009;50(8):1315–23.
17. Kadrmas DJ, et al. Effect of scan time on oncologic lesion detection in whole-body PET. IEEE Trans Nucl Sci. 2012;59:1940–7.
18. Lois C, et al. An assessment of the impact of incorporating time-of-flight information into clinical PET/CT imaging. J Nucl Med. 2010;51:237–45.
19. Muehllehner G, Karp JS, Surti S. Design considerations for PET scanners. Q J Nucl Med. 2002;46(1):16–23.
20. Moses WW, Derenzo SE. Prospects for time-of-flight PET using LSO scintillator. IEEE Trans Nucl Sci. 1999;46(3):474–8.
21. Moses WW. Time of flight in PET revisited. IEEE Trans Nucl Sci. 2003;50(5):1325–30.
22. Melcher CL, Schweitzer JS. Cerium-doped lutetium oxyorthosilicate - a fast, efficient new scintillator. IEEE Trans Nucl Sci. 1992;39(4):502–5.
23. Cherry SR, et al. MicroPET: a high resolution PET scanner for imaging small animals. IEEE Trans Nucl Sci. 1997;44:1161–6.
24. Schmand M, et al. Performance results of a new DOI detector block for a high resolution PET-LSO research tomograph HRRT. IEEE Trans Nucl Sci. 1998;45(6):3000–6.
25. Wienhard K, et al. The ECAT HRRT: performance and first clinical application of the new high resolution research tomograph. IEEE Trans Nucl Sci. 2002;49(1):104–10.
26. Spinks TJ, Bloomfield PM. A comparison of count rate performance for 15-O-water blood flow studies in the CTI HR+ and Accel tomographs in 3D mode. In: IEEE nuclear science symposium and medical imaging conference. Norfolk; 2002.
27. Surti S, et al. Imaging performance of A-PET: a small animal PET camera. IEEE Trans Med Imaging. 2005;24(7):844–52.
28. Surti S, et al. Performance of Philips Gemini TF PET/CT scanner with special consideration for its time-of-flight imaging capabilities. J Nucl Med. 2007;48(3):471–80.
29. Spurrier MA, et al. Effects of Ca2+ Co-doping on the scintillation properties of LSO:Ce. IEEE Trans Nucl Sci. 2008;55(3):1178–82.
30. Szczesniak T, et al. Timing resolution and decay time of LSO crystals Co-doped with calcium. IEEE Trans Nucl Sci. 2010;57(3):1329–34.
31. Blahuta S, et al. Evidence and consequences of Ce in LYSO: Ce, Ca and LYSO: Ce, Mg single crystals for medical imaging applications. IEEE Trans Nucl Sci. 2013;60(4):3134–41.
32. Brunner SE. Fast single photon detection for scintillation and cherenkov applications using silicon photomultipliers. 2014, TU Vienna.
33. Brunner SE, et al. Studies on the Cherenkov effect for improved time resolution of TOF-PET. IEEE Trans Nucl Sci. 2014;61:443–7.

34. Brunner SE, Schaart DR. BGO as a hybrid scintillator / Cherenkov radiator for cost-effective time-of-flight PET. Phys Med Biol. 2017;62(11):4421–39.
35. Kwon SI, et al. Bismuth germanate coupled to near ultraviolet silicon photomultipliers for time-of-flight PET. Phys Med Biol. 2016;61:L38.
36. Buzhan P, et al. An advanced study of silicon photomultiplier. ICFA Instrum Bullet. 2001;23:28.
37. Buzhan P, et al. Silicon photomultiplier and its possible applications. Nucl Inst Methods Phys Res A. 2003;504(1–3):48–52.
38. Bisello D, et al. Metal-Resistive layer-Silicon (MRS) avalanche detectors with negative feedback. Nucl Inst Methods Phys Res A. 1995;360(1–2):83–6.
39. Golovin V, Saveliev V. Novel type of avalanche photodetector with Geiger mode operation. Nucl Inst Methods Phys Res A. 2004;518(1–2):560–4.
40. Renker D. Geiger-mode avalanche photodiodes, history, properties and problems. Nucl Inst Methods Phys Res A. 2006;567(1):48–56.
41. Frach T, et al. The digital silicon photomultiplier: principle of operation and intrinsic detector performance. In: IEEE nuclear science symposium and medical imaging conference. Orlando; 2009.
42. Degenhardt C, et al. The digital silicon photomultiplier ; a novel sensor for the detection of scintillation light. In: IEEE nuclear science symposium and medical imaging conference. Orlando; 2009.
43. Casey ME, Nutt R. A multicrystal two dimensional BGO detector system for positron emission tomography. IEEE Trans Nucl Sci. 1986;33(1):460–3.
44. Wong WH, et al. A 2-dimensional detector decoding study on BGO arrays with quadrant sharing photomultipliers. IEEE Trans Nucl Sci. 1994;41(4):1453–7.
45. Surti S, et al. Optimizing the performance of a PET detector using discrete GSO crystals on a continuous lightguide. IEEE Trans Nucl Sci. 2000;47:1030–6.
46. Jakoby BW, et al. Physical and clinical performance of the mCT time-of-flight PET/CT scanner. Phys Med Biol. 2011;56(8):2375–89.
47. Bettinardi V, et al. Physical performance of the new hybrid PET/CT Discovery-690. Med Phys. 2011;38(10):5394–411.
48. Kolthammer JA, et al. Performance evaluation of the ingenuity TF PET/CT scanner with a focus on high count-rate conditions. Phys Med Biol. 2014;59(14):3843–59.
49. Burr KC, et al. A new modular and scalable detector for a time-of-flight PET scanner. In: IEEE nuclear science symposium and medical imaging conference. Anaheim; 2012.
50. Moses WW, Ullisch M. Factors influencing timing resolution in a commercial LSO PET camera. IEEE Trans Nucl Sci. 2006;53(1):78–85.
51. Krishnamoorthy S, et al. Design and performance of a high spatial-resolution, time-of-flight PET detector. IEEE Trans Nucl Sci. 2014;61:1092–8.
52. Son J-W, Ko GB, Won JY, Yoon HS, Lee JS. Development and performance evaluation of a time-of-flight positron emission tomography detector based on a high-quantum-efficiency multi-anode photomultiplier tube. IEEE Trans Nucl Sci. 2014;63:44–51.
53. Ferri A, et al. 100ps coincidence time resolution with LYSO coupled to NUV-HD SiPMs. In: IEEE nuclear science symposium and medical imaging conference. San Diego; 2015.
54. van Dam HT, et al. Sub-200 ps CRT in monolithic scintillator PET detectors using digital SiPM arrays and maximum likelihood interaction time estimation. Phys Med Biol. 2013;58(10):3243–58.
55. Seifert S, et al. First characterization of a digital SiPM based time-of-flight PET detector with 1 mm spatial resolution. Phys Med Biol. 2013;58(9):3061–74.
56. Borghi G, et al. A 32 mm × 32 mm × 22 mm monolithic LYSO:Ce detector with dual-sided digital photon counter readout for ultrahigh-performance TOF-PET and TOF-PET/MRI. Phys Med Biol. 2016;61(13):4929–49.
57. Popescu LM. Iterative image reconstruction using geometrically ordered subsets with list-mode data. In: IEEE nuclear science symposium and medical imaging conference. Rome; 2004.
58. Daube-Witherspoon ME, et al. Comparison of list-mode and DIRECT approaches for time-of-flight PET reconstruction. IEEE Trans Med Imaging. 2012;31:1461–71.

59. Asma E, et al. Accurate and consistent lesion quantitation with clinically acceptable penalized likelihood images. In: 2012 IEEE nuclear science symposium and medical imaging conference. Anaheim; 2012.
60. Panin VY, et al. Fully 3-D PET reconstruction with system matrix derived from point source measurements. IEEE Trans Med Imaging. 2006;25(7):907–21.
61. Tong S, Alessio AM, Kinahan PE. Noise and signal properties in PSF-based fully 3D PET image reconstruction: an experimental evaluation. Phys Med Biol. 2010;55(5):1453–73.
62. Panin VY, Aykac M, Casey ME. Simultaneous reconstruction of emission activity and attenuation coefficient distribution from TOF data, acquired with external transmission source. Phys Med Biol. 2013;58:3649–69.
63. Defrise M, Rezaei A, Nuyts J. Time-of-flight PET data determine the attenuation sinogram up to a constant. Phys Med Biol. 2012;57:885–99.
64. Rezaei A, et al. Simultaneous reconstruction of activity and attenuation in time-of-flight PET. IEEE Trans Med Imaging. 2012;31:2224–33.
65. Nuyts J, Rezaei A, Defrise M. ML-reconstruction for TOF-PET with simultaneous estimation of the attenuation factors. In: 2012 IEEE nuclear science symposium and medical imaging conference. Anaheim: IEEE; 2012.

Current Status and Future Directions of PET in Clinical Practice

2

Daniel A. Pryma

2.1 FDG PET/CT

2.1.1 Neuroimaging

The first human experience with FDG investigated brain glucose metabolism [1] and clinical use in neurology continues today. The two primary indications for neurologic FDG PET/CT in current practice are (1) the differentiation of frontotemporal from Alzheimer dementia in patients with clinical evidence of cognitive impairment and (2) localization of an interictal seizure focus in patients with refractory epilepsy. For dementia imaging, there is evidence and consensus opinion that FDG PET/CT can play an important role in identifying the underlying dementia subtype in cases when it is unclear but that the strongest evidence is limited to patients who already have dementia rather than mild cognitive impairment [2–7]. While the treatment approaches in various causes of dementia are different, overall treatment efficacy and outcome are limited, thus somewhat limiting the role of imaging. If more effective treatments are developed, particularly for early-stage disease, the potential need for imaging may increase.

Imaging in epilepsy is generally focused on patients with refractory seizure disorder being considered for surgical intervention. In these cases, the primary role of imaging is to determine the laterality of the seizure initiating focus in order to guide invasive electrical monitoring prior to resection [8–10]. Because the uptake of FDG takes several minutes, seizure imaging is generally limited to the interictal period when a seizure focus is hypometabolic relative to normal gray matter; interictal imaging with FDG PET/CT can be paired with ictal SPECT imaging using a blood flow radiopharmaceutical. However, ictal imaging is logistically complicated and quite expensive. Therefore, its use is limited to specialized centers. FDG PET/CT

D. A. Pryma (✉)
Perelman School of Medicine at the University of Pennsylvania, Philadelphia, PA, USA
e-mail: dpryma@pennmedicine.upenn.edu

J. Zhang, M. V. Knopp (eds.), *Advances in PET*,
https://doi.org/10.1007/978-3-030-43040-5_2

has been described in many other neurologic conditions such as traumatic brain injury and encephalitis. However, these uses remain largely in the realm of research rather than clinical use.

2.1.2 Cardiac Imaging

While the brain uses glucose exclusively for its energy needs, the heart can utilize a variety of substrates to meet its energy demands, and this can be exploited to answer specific clinical questions. Under normal physiologic conditions in a person following mixed diet, the myocardium will utilize a mix of glucose and fatty acids. During prolonged fasting or if following a ketogenic diet, the myocardium will generally use fatty acids exclusively. Conversely, when given a high-carbohydrate diet (coupled with insulin), the myocardium will utilize glucose.

Myocardial sarcoidosis is an important cause of life-threatening arrhythmias, but it is difficult to diagnose, and, therefore, imaging plays a considerable role. While MRI is frequently used to detect evidence of myocardial scarring caused by sarcoidosis, MRI is unable to distinguish active from prior sarcoidosis. Interestingly, active sarcoidosis uses glucose exclusively for energy and typically has a high glucose metabolic rate. By placing the patient on a ketogenic diet prior to a prolonged fasting period (at least 12 hours), glucose (and FDG) uptake in the normal myocardium will be suppressed, but any areas of active sarcoidosis will continue to exhibit high glucose uptake.

While normal myocardium can use multiple energy sources, ischemic myocardium is more constrained and can only use glucose. In patients with significant coronary artery disease, only areas of myocardium that remain viable could benefit from revascularization therapy. Therefore, FDG PET/CT can be used to detect areas of myocardium that may have considerably impaired perfusion but remain viable. In these cases, efforts are made to enhance myocardial glucose utilization through the administration of glucose and insulin.

2.1.3 Oncologic Imaging

Far and away the most common indication for FDG PET/CT (and, indeed, all PET/CT) in current clinical practice is oncologic imaging. This spans the natural history of cancer from searching for a cancer in a patient with symptoms or a paraneoplastic syndrome through response assessment in advanced-stage disease and detection of recurrent disease after therapy. For example, one of the first widely accepted and reimbursed indications for FDG PET/CT was for the characterization of solitary pulmonary nodules [11–13].

FDG PET/CT is important in oncologic imaging for two primary reasons: (1) based on the Warburg hypothesis that cancer cells obtain their energy primarily from glycolysis, cancers have broadly high utilization of glucose [14, 15] and, therefore, FDG, so imaging is quite sensitive for the detection of cancer very

broadly; (2) many cancer treatments rapidly alter glucose utilization, and therefore FDG PET/CT is very sensitive for the detection of response to therapy. FDG PET/CT is perhaps most tightly integrated into the care of patients with Hodgkin and aggressive non-Hodgkin lymphoma wherein scans at baseline and after two cycles of therapy are standard with frequent treatment adaptations based on the results of the interim scan [16–18].

There are two major limitations in the use of FDG PET/CT in oncology: (1) there are cancers that have mixed or low FDG uptake including some of the most common causes of cancer morbidity and mortality worldwide such as prostate cancer and hepatocellular cancer; (2) high glucose metabolic rate is not specific to cancer, and so there are many other diseases that can cause a positive FDG PET/CT limiting diagnostic accuracy in patients with multiple ongoing processes.

2.1.4 Infection/Inflammation

As relates to oncologic imaging, the most common cause of false-positive findings on FDG PET/CT is infection/inflammation. However, in the appropriate clinical setting, the high FDG uptake seen in many infections and inflammatory conditions may be utilized for diagnostic and prognostic value (as evidenced in the section on myocardial sarcoidosis identification with FDG PET/CT). However, this remains controversial with most uses for infection/inflammation not being widely reimbursed in the United States. There is, however, compelling evidence for the role of FDG PET/CT in conditions such as fever of unknown origin and cardiac device infections [19–23]. Utilization in other conditions such as arteritis and suspected post-traumatic osteomyelitis is more controversial and less widely utilized [24, 25].

2.1.5 Myocardial Perfusion Imaging

Myocardial perfusion imaging with ^{99m}Tc-based flow agents and SPECT has been a mainstay of nuclear medicine. There has been great interest in utilizing the sensitivity and quantitative accuracy afforded by PET/CT for myocardial perfusion imaging. While many radiopharmaceuticals have been investigated for this purpose, the most common in current clinical use are ^{13}nitrogen-ammonia and ^{82}rubidium (Rb) chloride [26–29]. The former is cyclotron produced with a 10-minute half-life, resulting in considerable logistical difficulties, and it is therefore used in a small number of centers. The latter has a 75-second half-life but is generator produced; the generator is eluted and the dose infused directly into the patient—it can be eluted every 10 minutes. This allows for widespread availability, though ^{82}Rb has other less favorable characteristics, chiefly a high positron energy that degrades the spatial resolution of the images. Furthermore, the short half-life necessitates injecting the patient while lying on the imaging table precluding physiologic exercise testing.

Myocardial perfusion PET/CT with dynamic imaging allows absolute quantification of regional myocardial blood flow, providing important prognostic and diagnostic information. Newer PET/CT devices with high sensitivity and excellent timing resolution further improve this quantitative accuracy across a broad range of patient sizes—current commercially available scanners permit up to 227 kg (500 lb) patients. Patients at the table weight limit can be imaged with acceptable, even excellent, image quality, something impossible with SPECT techniques.

2.1.6 Amyloid Imaging

While FDG PET/CT is useful to differentiate forms of dementia, there has been great interest in identifying the specific underlying causes of dementia particularly at an earlier stage when interventions may have better quality of life outcomes. Because of the amyloid hypothesis for Alzheimer dementia, there has been considerable work in developing amyloid PET radiopharmaceuticals, and three agents are currently FDA approved in the United States, all labeled with ^{18}F: florbetaben, florbetapir, and flutemetamol [30–33]. These have excellent negative predictive value such that a negative scan essentially excludes Alzheimer disease as the cause of a patient's cognitive impairment. However, not all patients with abnormal amyloid deposition suffer from Alzheimer disease, and so the positive predictive value of the scans is low. Because of this and concerns regarding the current lack of effective therapies for dementia amyloid, PET/CT is not generally reimbursed in the United States, and its role in patient management remains unclear. Research is ongoing to more fully understand the potential role of these imaging agents. Furthermore, other dementia imaging agents are under active development, for example, to image the tau proteins that are also part of Alzheimer pathogenesis.

2.1.7 Somatostatin Receptor Imaging

Neuroendocrine tumors are a broad spectrum of cancers with certain features in common, one of which is high expression of the somatostatin receptor. These cancers often also have low glucose metabolic rates, and so FDG PET/CT has low sensitivity for the detection of disease. Somatostatin receptor scintigraphy with ^{111}In-pentetreotide has long been a mainstay of imaging this disease, but it has been largely replaced by a PET/CT analog ^{68}Ga-DOTATATE (currently this is the only agent FDA approved in the United States, but many other PET somatostatin analog radiopharmaceuticals have been described) [34–37]. A generator-produced positron emitter, ^{68}Ga, has a 68-minute half-life with a relatively long-lived parent allowing a generator life span of 6–9 months with up to three elutions per day. Interestingly, there can be interplay between uptake on FDG and DOTATATE PET/CT scans in a given patient with more aggressive neuroendocrine cancer with important prognostic implications [35].

2.2 PET/MR

The above sections have focused solely on PET/CT which remains the most widely utilized hybrid scanner design. However, there has been interest in combining PET with MR, and commercially available hybrid PET/MR devices are available on the market. With MR-compatible photomultiplier tubes, the PET components can be inserted into the MR bore allowing simultaneous PET and MR acquisition. As with most new advanced imaging devices, initial work focused on neuroimaging [38]. There are, unfortunately, compromises made in PET/MR compared to PET/CT. First, attenuation correction using CT is relatively straightforward but is much more difficult given that MR cannot so easily measure the likelihood of photon attenuation in tissue. While methods to achieve this have been largely worked out, there are still some limitations compared to CT in certain body areas as well as in the time required to acquire an attenuation map [39]. Furthermore, in order to achieve an acceptable bore size with the PET componentry within the MR bore, the MR must have a wide bore, and this, combined with the effects of the PET componentry within the bore, can have negative implications on image quality compared to a stand-alone MR.

There remain potential advantages to PET/MR compared with PET/CT. For example, there is no ionizing radiation exposure from the MR, whereas there is a dose from the CT. This is considered particularly important in pediatric imaging and may become more important as research continues in potential PET applications outside of life-threatening diseases such as cancer. However, it must be noted that with iterative reconstruction techniques and a focus on dose reduction, the radiation exposure from a CT component of PET/CT optimized solely for attenuation correction is very modest.

The ability to perform simultaneous acquisitions is likely the greatest potential advantage of PET/MR with the most compelling work to date focused on real-time motion correction in PET/MR myocardial imaging [40–44]. This could potentially result in high diagnostic accuracy in a way that cannot be achieved with separate PET/CT and MR devices, as opposed to most other previously described potential applications for PET/MR.

The major disadvantages of PET/MR, in addition to the technical considerations, are cost and uncertain synergy. Because of the complexities in the system, a PET/MR device costs considerably more than purchasing separate PET/CT and MR devices (albeit with a savings in room space needed). However, more important is the potential lack of synergy. Probably the greatest advantage of PET/CT, particularly in oncology, is being able to relatively quickly sample the entire patient to detect disease, whereas probably the greatest advantage of MR is exquisite focused tissue characterization. Therefore, an optimized PET acquisition will image most of the body as quickly as possible, whereas an optimized MR acquisition will thoroughly sample a smaller area. Therefore, it is very unclear how to best optimize PET/MR acquisitions. Furthermore, PET and MR can both perform specific tissue characterization, albeit very differently. Therefore, they have partially overlapping strengths, whereas PET and CT are almost entirely nonoverlapping.

While PET/MR appears to have niches with potentially important clinical utility, it is likely that it will remain a much smaller market segment compared to PET/CT.

2.3 Future Directions

Because of the high sensitivity and spatial resolution of PET compared with other functional imaging modalities, there are innumerable ongoing trials testing PET radiopharmaceuticals. These range from elemental salts such as ^{124}I-sodium iodide to radiolabeled intact antibodies or nanoparticles. The majority of agents in later phase clinical trials are small molecules or peptides, most of which are labeled with the relatively short-lived isotopes ^{18}F and ^{68}Ga, though some are labeled with longer-lived isotopes such as ^{64}Cu ($T_{½}$ 12.7 hours), ^{89}Zr ($T_{½}$ 3.3 days), or ^{124}I ($T_{½}$ 4.2 days).

Most agents under development seek to detect or characterize some specific aspect of disease such as receptor status or antigen expression for one of two reasons. Specific cancer detection agents have been developed for diseases that have low FDG uptake. Alternatively, many agents have been developed more for disease characterization and to evaluate the patient for a specific targeted therapy than for detection. This is a reasonable approach given the high sensitivity but lower specificity of FDG PET/CT. However, because FDG PET/CT is imperfect with malignant diseases that are poorly FDG avid and many benign processes that result in false positives, general cancer detection radiopharmaceuticals have been developed as potential FDG replacements. Finally, while oncologic imaging is the primary current use of FDG PET/CT and the focus of much research, there is also a great deal of work on PET radiotracers for non-oncologic diseases.

Fibroblast activation protein (FAP) is a protein associated with the fibroblasts that are overexpressed in the vast majority of epithelial cancer stroma. Thus, it can be possible to detect the tumor stroma rather than the tumor itself using a target that should be more cancer-specific than FDG. Therefore, among potential targets for a general cancer imaging radiotracer, FAP agents appear to be the most promising [45, 46]. However, it is important to note that they are still very early in development and also that the bar to supersede FDG PET/CT is quite high since FDG PET/CT has excellent diagnostic accuracy despite its limitations.

Among agents developed for detection of poorly FDG avid diseases, radiopharmaceuticals to detect prostate-specific membrane antigen (PSMA) are certainly the closest to clinical use and most widely investigated, with two agents nearing likely FDA approval [47–50]. These agents appear to have much higher sensitivity for detection of disease than other available imaging techniques while preserving very high specificity. They are also paired with PSMA-targeted therapeutics and so will likely be used for both diagnostic and theranostic purposes.

Outside of oncology, there is a great deal of ongoing research on neurologic and cardiac imaging. For example, given the ongoing opioid crisis, there is a great deal of effort to use PET to help understand and, hopefully, develop treatments for addiction [51, 52]. Additionally, development of tracers specific for the neurodegeneration seen in Parkinson disease has been an ongoing effort [53, 54]. In cardiology,

two myocardial perfusion PET tracers are currently available (^{13}N ammonia and ^{82}Rb rubidium chloride); as discussed previously, there has been significant effort to develop ^{18}F myocardial perfusion tracers that could potentially be more widely available to sites that do not have a cyclotron to produce ammonia or enough volume to warrant the cost of a rubidium generator. Chief among these is ^{18}F flurpiridaz which is in late phase clinical trials and may become available in the coming years [55, 56]. Additionally, there is interest in developing more specific PET tracers for cardiac sarcoidosis or amyloid, with most efforts focused on repurposing existing tracers for these indications [57–59].

Finally, given the improving sensitivity of PET/CT devices, particularly with long axial field of view, there is increasing potential to image patients quickly with relatively low administered activity resulting in low radiation exposure. While most current indications for PET are for diseases conferring a limited life expectancy (cancer, coronary artery disease, neurodegeneration), a low radiation exposure increasingly allows consideration of PET for diseases that may not impact on life expectancy. For example, infection imaging is an area of growth [60, 61]. While this has been done with FDG, the inherent lack of specificity limits its role, and there are new approaches that could exploit the sensitivity of PET to improve upon prior insufficient performance of single-photon imaging.

Overall, there are a seemingly infinite number of targets for PET imaging whose development will be limited only by researchers' imaginations. Those that are found to be useful may translate into routine clinical availability. However, in the United States, reimbursement for imaging with novel radiotracers is likely to be among the most significant barriers to widespread growth. It is very likely, though, that the role of PET/CT in the care of patients will expand over the coming decade and beyond.

2.4 Conclusion

PET/CT is widely used clinically, but the vast majority of current clinical use remains in oncologic imaging utilizing FDG. However, multiple additional radiopharmaceuticals are currently available with many, many more in development across a broad spectrum of diseases. While FDG PET/CT is likely to remain the mainstay of PET imaging, its relative market share will almost certainly decrease over time as tracers for new indications come into wider use. However, it is unlikely that a single tracer will ever exceed the broad applicability of FDG.

References

1. Reivich M, Kuhl D, Wolf A, et al. Measurement of local cerebral glucose metabolism in man with 18F-2-fluoro-2-deoxy-d-glucose. Acta Neurol Scand Suppl. 1977;64:190–1.
2. Agosta F, Altomare D, Festari C, et al. Clinical utility of FDG-PET in amyotrophic lateral sclerosis and Huntington's disease. Eur J Nucl Med Mol Imaging. 2018;45(9):1546–56.
3. Arbizu J, Festari C, Altomare D, et al. Clinical utility of FDG-PET for the clinical diagnosis in MCI. Eur J Nucl Med Mol Imaging. 2018;45(9):1497–508.

4. Bouwman F, Orini S, Gandolfo F, et al. Diagnostic utility of FDG-PET in the differential diagnosis between different forms of primary progressive aphasia. Eur J Nucl Med Mol Imaging. 2018;45(9):1526–33.
5. Caminiti SP, Sala A, Iaccarino L, et al. Brain glucose metabolism in Lewy body dementia: implications for diagnostic criteria. Alzheimers Res Ther. 2019;11(1):20.
6. Drzezga A, Altomare D, Festari C, et al. Diagnostic utility of 18F-Fluorodeoxyglucose positron emission tomography (FDG-PET) in asymptomatic subjects at increased risk for Alzheimer's disease. Eur J Nucl Med Mol Imaging. 2018;45(9):1487–96.
7. Nestor PJ, Altomare D, Festari C, et al. Clinical utility of FDG-PET for the differential diagnosis among the main forms of dementia. Eur J Nucl Med Mol Imaging. 2018;45(9):1509–25.
8. Cahill V, Sinclair B, Malpas CB, et al. Metabolic patterns and seizure outcomes following anterior temporal lobectomy. Ann Neurol. 2019;85(2):241–50.
9. Mayoral M, Ninerola-Baizan A, Marti-Fuster B, et al. Epileptogenic zone localization with (18)FDG PET using a new dynamic parametric analysis. Front Neurol. 2019;10:380.
10. Perissinotti A, Ninerola-Baizan A, Rubi S, et al. PISCOM: a new procedure for epilepsy combining ictal SPECT and interictal PET. Eur J Nucl Med Mol Imaging. 2018;45(13):2358–67.
11. Dewan NA, Gupta NC, Redepenning LS, Phalen JJ, Frick MP. Diagnostic efficacy of PET-FDG imaging in solitary pulmonary nodules. Potential role in evaluation and management. Chest. 1993;104(4):997–1002.
12. Gupta NC, Frank AR, Dewan NA, et al. Solitary pulmonary nodules: detection of malignancy with PET with 2-[F-18]-fluoro-2-deoxy-D-glucose. Radiology. 1992;184(2):441–4.
13. Patz EF Jr, Lowe VJ, Hoffman JM, et al. Focal pulmonary abnormalities: evaluation with F-18 fluorodeoxyglucose PET scanning. Radiology. 1993;188(2):487–90.
14. Hofmann P. Cancer and exercise: Warburg hypothesis, tumour metabolism and high-intensity anaerobic exercise. Sports (Basel). 2018;6(1):10.
15. Weinhouse S. The Warburg hypothesis fifty years later. Z Krebsforsch Klin Onkol Cancer Res Clin Oncol. 1976;87(2):115–26.
16. Adams HJA, Kwee TC. An evidence-based review on the value of interim FDG-PET in assessing response to therapy in lymphoma. Semin Oncol. 2017;44(6):404–19.
17. Berriolo-Riedinger A, Becker S, Casasnovas O, Vander Borght T, Edeline V. Role of FDG PET-CT in the treatment management of Hodgkin lymphoma. Cancer Radiother. 2018;22(5):393–400.
18. Burggraaff CN, de Jong A, Hoekstra OS, et al. Predictive value of interim positron emission tomography in diffuse large B-cell lymphoma: a systematic review and meta-analysis. Eur J Nucl Med Mol Imaging. 2019;46(1):65–79.
19. Al-Zaghal A, Raynor WY, Seraj SM, Werner TJ, Alavi A. FDG-PET imaging to detect and characterize underlying causes of fever of unknown origin: an unavoidable path for the foreseeable future. Eur J Nucl Med Mol Imaging. 2019;46(1):2–7.
20. Bharucha T, Rutherford A, Skeoch S, et al. Diagnostic yield of FDG-PET/CT in fever of unknown origin: a systematic review, meta-analysis, and Delphi exercise. Clin Radiol. 2017;72(9):764–71.
21. Bhoil A, Vinjamuri S. Role of 18F-FDG PET/CT in infection of cardiovascular implantable electronic devices: review of the literature and initial experience. Nucl Med Commun. 2019;40:555.
22. Schonau V, Vogel K, Englbrecht M, et al. The value of (18)F-FDG-PET/CT in identifying the cause of fever of unknown origin (FUO) and inflammation of unknown origin (IUO): data from a prospective study. Ann Rheum Dis. 2018;77(1):70–7.
23. Sethi I, Baum YS, Grady EE. Current status of molecular imaging of infection: A primer. AJR Am J Roentgenol Apr. 2019;23:1–9.
24. Direskeneli H. Clinical assessment in Takayasu's arteritis: major challenges and controversies. Clin Exp Rheumatol. 2017;35 Suppl 103(1):189–93.
25. Govaert GA, IJpma FF, McNally M, McNally E, Reininga IH, Glaudemans AW. Accuracy of diagnostic imaging modalities for peripheral post-traumatic osteomyelitis - a systematic review of the recent literature. Eur J Nucl Med Mol Imaging. 2017;44(8):1393–407.

26. deKemp RA, Renaud JM, Klein R, Beanlands RS. Radionuclide tracers for myocardial perfusion imaging and blood flow quantification. Cardiol Clin. 2016;34(1):37–46.
27. Juneau D, Erthal F, Ohira H, et al. Clinical PET myocardial perfusion imaging and flow quantification. Cardiol Clin. 2016;34(1):69–85.
28. Moody JB, Lee BC, Corbett JR, Ficaro EP, Murthy VL. Precision and accuracy of clinical quantification of myocardial blood flow by dynamic PET: A technical perspective. J Nucl Cardiol. 2015;22(5):935–51.
29. Renaud JM, Mylonas I, McArdle B, et al. Clinical interpretation standards and quality assurance for the multicenter PET/CT trial rubidium-ARMI. J Nucl Med. 2014;55(1):58–64.
30. Bloudek LM, Spackman DE, Blankenburg M, Sullivan SD. Review and meta-analysis of biomarkers and diagnostic imaging in Alzheimer's disease. J Alzheimers Dis. 2011;26(4): 627–45.
31. Fantoni ER, Chalkidou A, O'Brien JT, Farrar G, Hammers A. A systematic review and aggregated analysis on the impact of amyloid PET brain imaging on the diagnosis, diagnostic confidence, and management of patients being evaluated for Alzheimer's disease. J Alzheimers Dis. 2018;63(2):783–96.
32. Hellwig S, Frings L, Bormann T, Vach W, Buchert R, Meyer PT. Amyloid imaging for differential diagnosis of dementia: incremental value compared to clinical diagnosis and [(18) F]FDG PET. Eur J Nucl Med Mol Imaging. 2019;46(2):312–23.
33. Schilling LP, Pascoal TA, Zimmer ER, et al. Regional amyloid-beta load and white matter abnormalities contribute to hypometabolism in Alzheimer's dementia. Mol Neurobiol. 2018;56:4916.
34. Galne A, Almquist H, Almquist M, et al. A prospective observational study to evaluate the effects of long-acting somatostatin analogs on (68)Ga-DOTATATE uptake in patients with neuroendocrine tumors. J Nucl Med. 2019;60:1717.
35. Jiang Y, Hou G, Cheng W. The utility of 18F-FDG and 68Ga-DOTA-Peptide PET/CT in the evaluation of primary pulmonary carcinoid: A systematic review and meta-analysis. Medicine (Baltimore). 2019;98(10):e14769.
36. Komek H, Can C, Urakci Z, Kepenek F. Comparison of (18F)FDG PET/CT and (68Ga) DOTATATE PET/CT imaging methods in terms of detection of histological subtype and related SUVmax values in patients with pulmonary carcinoid tumors. Nucl Med Commun. 2019;40(5):517–24.
37. Tierney JF, Kosche C, Schadde E, et al. (68)Gallium-DOTATATE positron emission tomography-computed tomography (PET CT) changes management in a majority of patients with neuroendocrine tumors. Surgery. 2019;165(1):178–85.
38. Anazodo UC, Finger E, Kwan BYM, et al. Using simultaneous PET/MRI to compare the accuracy of diagnosing frontotemporal dementia by arterial spin labelling MRI and FDG-PET. Neuroimage Clin. 2018;17:405–14.
39. Lassen ML, Rasul S, Beitzke D, et al. Assessment of attenuation correction for myocardial PET imaging using combined PET/MRI. J Nucl Cardiol. 2019;26:1107.
40. Beitzke D, Rasul S, Lassen ML, et al. Assessment of myocardial viability in ischemic heart disease by PET/MRI: comparison of left ventricular perfusion, hibernation, and scar burden. Acad Radiol. 2019;27:188.
41. Lucke C, Oppolzer B, Werner P, et al. Comparison of volumetric and functional parameters in simultaneous cardiac PET/MR: feasibility of volumetric assessment with residual activity from prior PET/CT. Eur Radiol. 2017;27(12):5146–57.
42. Munoz C, Kunze KP, Neji R, et al. Motion-corrected whole-heart PET-MR for the simultaneous visualisation of coronary artery integrity and myocardial viability: an initial clinical validation. Eur J Nucl Med Mol Imaging. 2018;45(11):1975–86.
43. Sgard B, Brillet PY, Bouvry D, et al. Evaluation of FDG PET combined with cardiac MRI for the diagnosis and therapeutic monitoring of cardiac sarcoidosis. Clin Radiol. 2019;74(1):81 e89–81 e18.
44. Wisenberg G, Thiessen JD, Pavlovsky W, Butler J, Wilk B, Prato FS. Same day comparison of PET/CT and PET/MR in patients with cardiac sarcoidosis. J Nucl Cardiol. 2019.

45. Giesel FL, Kratochwil C, Lindner T, et al. (68)Ga-FAPI PET/CT: biodistribution and preliminary dosimetry estimate of 2 DOTA-containing FAP-targeting agents in patients with various cancers. J Nucl Med. 2019;60(3):386–92.
46. Loktev A, Lindner T, Burger EM, et al. Development of fibroblast activation protein-targeted radiotracers with improved tumor retention. J Nucl Med. 2019;60(10):1421–9.
47. Calais J, Ceci F, Eiber M, et al. (18)F-fluciclovine PET-CT and (68)Ga-PSMA-11 PET-CT in patients with early biochemical recurrence after prostatectomy: a prospective, single-centre, single-arm, comparative imaging trial. Lancet Oncol. 2019;20(9):1286–94.
48. Rousseau C, Le Thiec M, Ferrer L, et al. Preliminary results of a (68) Ga-PSMA PET/CT prospective study in prostate cancer patients with occult recurrence: diagnostic performance and impact on therapeutic decision-making. Prostate. 2019;79(13):1514–22.
49. Rousseau E, Wilson D, Lacroix-Poisson F, et al. A prospective study on (18)F-DCFPyL PSMA PET/CT imaging in biochemical recurrence of prostate cancer. J Nucl Med. 2019;60:1587.
50. Wondergem M, Jansen BHE, van der Zant FM, et al. Early lesion detection with (18) F-DCFPyL PET/CT in 248 patients with biochemically recurrent prostate cancer. Eur J Nucl Med Mol Imaging. 2019;46(9):1911–8.
51. Dubroff JG, Doot RK, Falcone M, et al. Decreased nicotinic receptor availability in smokers with slow rates of nicotine metabolism. J Nucl Med. 2015;56(11):1724–9.
52. Martinez D, Slifstein M, Matuskey D, et al. Kappa-opioid receptors, dynorphin, and cocaine addiction: a positron emission tomography study. Neuropsychopharmacology. 2019;44(10):1720–7.
53. Hsieh CJ, Xu K, Lee I, et al. Chalcones and five-membered heterocyclic Isosteres bind to alpha synuclein fibrils in vitro. ACS Omega. 2018;3(4):4486–93.
54. Laforest R, Karimi M, Moerlein SM, et al. Absorbed radiation dosimetry of the D3-specific PET radioligand [(18)F]FluorTriopride estimated using rodent and nonhuman primate. Am J Nucl Med Mol Imaging. 2016;6(6):301–9.
55. Berman DS, Maddahi J, Tamarappoo BK, et al. Phase II safety and clinical comparison with single-photon emission computed tomography myocardial perfusion imaging for detection of coronary artery disease: flurpiridaz F 18 positron emission tomography. J Am Coll Cardiol. 2013;61(4):469–77.
56. Maddahi J, Bengel F, Czernin J, et al. Dosimetry, biodistribution, and safety of flurpiridaz F 18 in healthy subjects undergoing rest and exercise or pharmacological stress PET myocardial perfusion imaging. J Nucl Cardiol. 2019;26:2018.
57. Abulizi M, Sifaoui I, Wuliya-Gariepy M, et al. (18)F-sodium fluoride PET/MRI myocardial imaging in patients with suspected cardiac amyloidosis. J Nucl Cardiol. 2019.
58. Anzola LK, Glaudemans A, Dierckx R, Martinez FA, Moreno S, Signore A. Somatostatin receptor imaging by SPECT and PET in patients with chronic inflammatory disorders: a systematic review. Eur J Nucl Med Mol Imaging. 2019;46:2496.
59. Dietemann S, Nkoulou R. Amyloid PET imaging in cardiac amyloidosis: a pilot study using (18)F-flutemetamol positron emission tomography. Ann Nucl Med. 2019;33(8):624–8.
60. Ordonez AA, Sellmyer MA, Gowrishankar G, et al. Molecular imaging of bacterial infections: overcoming the barriers to clinical translation. Sci Transl Med. 2019;11(508).
61. Sellmyer MA, Lee I, Hou C, et al. Bacterial infection imaging with [(18)F]fluoropropyl-trimethoprim. Proc Natl Acad Sci U S A. 2017;114(31):8372–7.

Part II

Solid State Digital PET Instrumentation, Technology and Clinical Practice

Introduction to Silicon Photomultipliers for Time-of-Flight PET

3

Dennis R. Schaart

3.1 Introduction

The development of PET scintillation detectors with optimum timing characteristics requires the use of photosensors with single-photon detection capability. The PMT has long been the device of choice in PET scanners, as they offer excellent photon counting performance at moderate costs per unit sensitive area. However, the high-end systems of essentially all commercial manufacturers are now being equipped with silicon photomultipliers (SiPMs), resulting in TOF-PET images of unparalleled quality. This chapter offers a brief introduction into silicon photomultipliers, with particular attention for the factors that determine the time resolution of SiPM-based scintillation detectors.

3.2 TOF-PET Photosensor Requirements

It is well understood that photosensors must have internal gain in order to be capable of counting single photons near room temperature [17]. The photosensor should furthermore have the highest possible photon detection efficiency (PDE), defined as the percentage of photons incident on the photosensor that gives rise to a measurable electronic signal. It should also have excellent single-photon time resolution (SPTR), that is, the timing uncertainty when one photon is being detected per measurement.

The ideal single-photon sensor should furthermore facilitate efficient optical coupling with scintillation crystals. For example, dead regions in the photosensitive surface should be reduced to a minimum, and the refractive index of the entrance

D. R. Schaart (✉)
Delft University of Technology, Radiation Science & Technology Department, Delft, The Netherlands
e-mail: d.r.schaart@tudelft.nl

J. Zhang, M. V. Knopp (eds.), *Advances in PET*,
https://doi.org/10.1007/978-3-030-43040-5_3

window should match that of the scintillator as closely as possible. The ideal sensor design should furthermore be compact and scalable in order to facilitate an optimum geometrical arrangement of crystals and sensors.

Uniformity of parameters such as the PDE, internal gain, and pulse propagation time over the active area of the sensor, as well as between sensors, helps to achieve a constant response throughout a PET system. This reduces the magnitude of the corresponding correction factors to be applied during signal processing, which in turn reduces the influence of the corresponding uncertainties on the image quality. Finally, aspects such as the device lifetime, stability of operation, and cost per unit area are important considerations for commercial manufacturers of TOF-PET equipment.

3.3 Vacuum Photomultipliers

The vacuum photomultiplier tube (PMT) has been the workhorse for reading out scintillation signals since the early days of PET development. Invented during the interbellum, it is still being used in many PET systems installed in clinics today. The principles of operation and properties of PMTs are well understood and documented, for example, by Wright [50]. The timing theory of PMT-based scintillation detectors has been studied in depth in the 1960s and 1970s. The theory by Hyman [23] in particular has found widespread use, and it can be shown that it is a special case of the Seifert model developed more recently [42].

The PDE of a PMT equals the product of the quantum efficiency (QE) of its photocathode and the photoelectron collection efficiency of the first dynode. It is common practice, however, to loosely refer to the PDE of a PMT as the "QE of the photomultiplier." PMTs with a standard bi-alkali photocathode typically have a QE of ~25% around 400 nm, but PMTs with a so-called super bi-alkali or ultra bi-alkali photocathodes may have a QE of up to ~35% and ~43%, respectively [24, 32].

The SPTR of a PMT is commonly referred to as its transit time spread (TTS), which is primarily determined by the variation in the transfer times of the photoelectrons between the photocathode and the first dynode. Manufacturers have developed a variety of PMTs optimized for fast timing applications. While the SPTR of classic PM tubes is in the order of ~ns, fast PMTs may have values better than 200 ps FWHM [30, 43, 49].

The electronic properties of PMTs are favorable for obtaining good time resolution: they have high internal gain (~10^6–10^8), low dark current, and low capacitance (typically ~10 pF), and the anode has the equivalent circuit of a current source with high bandwidth (~GHz). PMT front-end electronics typically load the anode with a 50 Ω input resistance, sufficiently low to maintain high bandwidth while matching the impedance of standard coaxial cables. The output pulse shape of typical PMT-based scintillation detectors is such that optimum time resolution is obtained when the trigger threshold is set between about 10% and 30% of the average pulse height. Such a relatively high threshold makes the time pickoff susceptible to pulse height variations, which inevitably occur due to the finite energy

resolution of the scintillator and the gain dispersion of the PMT. A constant-fraction discriminator remedies this problem by triggering on a fixed fraction of the actual pulse height [4, 20, 27].

Since 2006, a variety of TOF-PET systems based on PMTs and L(Y)SO:Ce crystals have been brought to the market. These devices typically have coincidence resolving time (CRT) between about 400 and 700 ps FWHM at system level.

3.4 Solid-State Photomultipliers

3.4.1 Introduction to Silicon Photomultipliers

PET detector developers have been interested to replace PMTs by semiconductor photosensors for several decades. Advantages of solid-state light sensors over PMTs include a potentially high PDE, small size, flexibility in sensor geometric design, ruggedness, and unperturbed performance in strong magnetic fields (enabling MRI compatibility).

PET detectors based on (p-i-n) photodiodes and avalanche photodiodes (APDs) were explored by various authors in the 1990s and early 2000s [8, 22, 26, 34]. Whereas photodiodes lack internal amplification, APDs operate at a large reverse bias voltage (typically several hundreds of volts), resulting in a high electric field strength in the depletion region of the diode. This field accelerates the charge carriers created upon the absorption of a scintillation photon, resulting in the creation of an avalanche. APDs may have a gain in the order of 100–1000 and their PDE can exceed 90%.

APDs were used in the first commercial whole-body clinical PET/MRI system [15]. Unfortunately, due to the large diode capacitance, the response of APDs tends to be relatively slow (typically exhibiting a ~10 ns signal rise time). In combination with the relatively modest gain, this makes it difficult to achieve a time resolution sufficiently good for TOF-PET using APDs.

A more recent development in the field of solid-state photosensors is the silicon photomultiplier. These devices are of great interest for TOF-PET as they offer a high PDE, a high internal gain, and a relatively fast response. Figure 3.1 provides examples of a single SiPM and a SiPM array. SiPMs can be fabricated using CMOS technology, opening up the possibility of low-cost production when made in large quantities. Moreover, SiPMs operate at bias voltages of several tens of volt only. The history of development and the principles of operation of (analog) SiPMs have been reviewed by various authors, for example, Acerbi and Gundacker [3], Bisogni and Morrocchi [5], Donati and Tambosso [17], Renker [36], Renker and Lorenz [37], and Roncali and Cherry [38].

The presently most common implementation of the SiPM comprises a large number (typically 10^2–10^5) of ADPs operated in Geiger mode and connected in parallel (see Fig. 3.2). Devices with this topology are sometimes called analog SiPMs to distinguish them from their digital counterparts, which will be discussed in Sect. 3.4.5. The Geiger-mode APDs (GM-APDs), also called single-photon avalanche diodes (SPADs) or microcells, are operated at a reverse bias voltage V_{bb} that

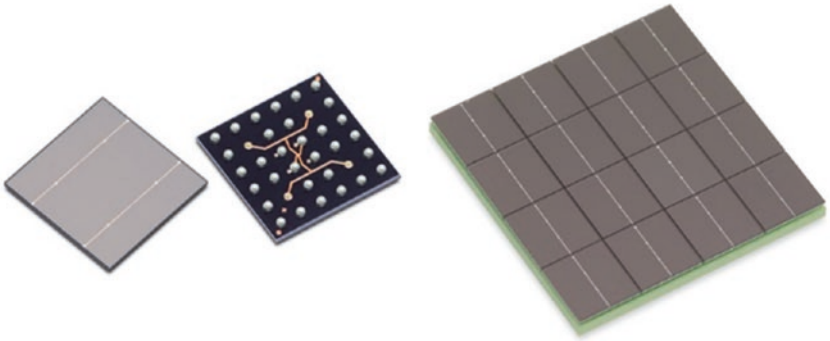

Fig. 3.1 Photographs of (left) a 6 mm × 6 mm single SiPM chip (Broadcom AFBR-S4N66C013) and (right) a SiPM array comprising 4 × 4 SiPM pixels of 4 mm × 4 mm each (Broadcom AFBR-S4N44P163). Dead space between the SiPM chips is minimized due to the use of through-silicon via (TSV) technology; the middle image shows the soldering balls on the backside of the 6 mm × 6 mm chip. (Photographs kindly provided by Dr. S.E. Brunner, Broadcom Inc.)

exceeds the breakdown voltage V_{bd} by a few volts. The avalanche becomes self-sustaining in this regime and continues until it is quenched. In the simplest case, this is achieved by means of a quench resistor R_q placed in series with the diode.

The gain of a SPAD typically is in the order of 10^5–10^7. The total charge released in a discharge is independent on the number of initial charge carriers [35]. Thus, a SPAD can detect only a single photon at a time; it is indeed a single-photon counter. The massive parallel connection of many SPADs in a SiPM allows for a nearly proportional response if the light intensity is sufficiently low, that is, if there is negligible probability that more than one photon hits a single SPAD within its recovery time.

SiPMs have a number of non-idealities that can significantly affect the performance of a PET detector. For example, the gain is a function of the voltage over breakdown $V_{ob} = V_{bb} - V_{bd}$, where V_{bd} depends on temperature. To achieve stable gain, the SiPM temperature may need to be controlled, and/or V_{bb} may need to be adjusted continuously to the device temperature. Furthermore, dark counts occur due to the triggering of avalanches by thermally generated electron-hole pairs and field-assisted generation of free electrons. Thermal generation is dominant at room temperature, and the resulting dark count rate (DCR) typically increases with a factor of about two for every 8 K temperature increase. The DCR of a SiPM furthermore increases with increasing V_{ob} and device area. Room-temperature DCR values of commercial SiPMs have decreased from the ~MHz mm^{-2} level to less than 100 kHz mm^{-2} for some devices. Fortunately, because of the relatively short (<1 μs) signal integration times used in PET, the influence of dark counts on the detector energy resolution can usually be kept very small.

A fundamental non-ideality of any SiPM is that its response $\chi = N_f/\eta_{pd}N_{ph}$, with N_f the number of fired SPADs, N_{ph} the number of photons incident on the SiPM, and η_{pd} its PDE under sparse illumination conditions, is inherently nonproportional due to the combined effects of saturation, afterpulsing, and crosstalk. Saturation occurs if the SPADs are illuminated by more than one photon during their recovery time.

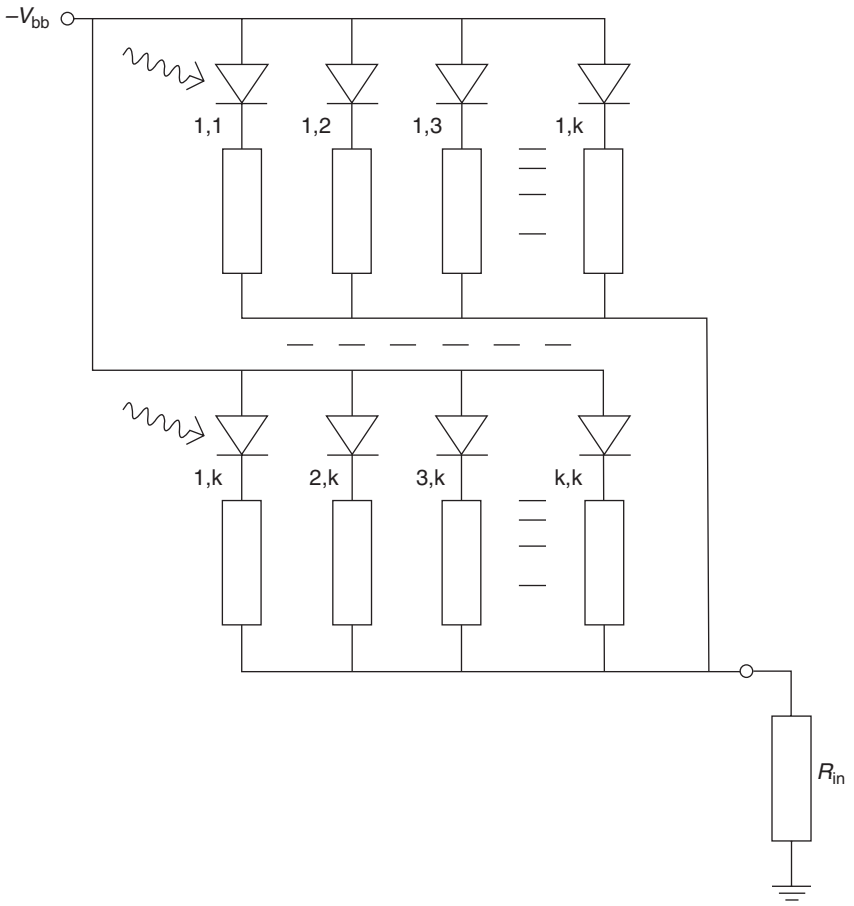

Fig. 3.2 Schematic representation of a SiPM, consisting of a large number of single-photon avalanche diodes connected in parallel. The symbol V_{bb} denotes the bias voltage and R_{in} is the input resistance of the readout circuit

Afterpulses are generated by charge carriers that are trapped during a Geiger discharge and released after some time, triggering a new avalanche. The probability of afterpulsing is a function of the SPAD recovery time, overvoltage, and temperature and may have a value in the order of 0.1–10% at room temperature. Crosstalk between SPADs is caused by the optical photons produced within an avalanche, which may trigger discharges in neighboring SPADs. The crosstalk probability is influenced by the structure of the device and the overvoltage. It may be in the order of 1–20%.

A simple model of the influence of saturation on the response of SiPMs is applicable to instantaneous light pulses only and furthermore assumes that crosstalk, afterpulsing, and dark counts are absent. Under these conditions, the lower limit of the SiPM response is reached. For a SiPM that consists of N_{spads} SPADs, this lower limit can be written as:

$$\chi_{\text{lower}} = \frac{N_{\text{spads}}}{\eta_{\text{pd}} N_{\text{ph}}} \left(1 - e^{-\frac{\eta_{\text{pd}} N_{\text{ph}}}{N_{\text{spads}}}} \right) \tag{3.1}$$

This simple model may not be sufficiently accurate if the influences of crosstalk and afterpulsing are not negligible and/or the light pulse is not instantaneous, such as in PET scintillation detectors. A fully analytical model of the SiPM response that is applicable to exponentially decaying as well as instantaneous light pulses has been developed by Van Dam et al. [45].

3.4.2 SiPM Single-Photon Signal Shape

Figure 3.3 shows an equivalent electronic circuit commonly used to simulate the discharge of a single SPAD in a SiPM. The active SPAD comprises a reverse-biased photodiode with capacitance C_d. This diode is placed in series with a quench resistor R_q that has a parasitic or intentional parallel capacitance C_q. The $N_{spads} - 1$ remaining SPADs are represented by the corresponding quantities in the "passive" section of the equivalent circuit. The capacitance C_g equals the sum of the parasitic capacitances of all microcells connected in parallel.

The closing of the switch S in the active SPAD represents the triggering of a discharge by a photon [40]. At the moment t_0 at which the switch is closed, the difference between V_{bb} and V_{bd}, that is, V_{ob}, appears instantly across R_d, which represents the internal resistance of the diode space-charge region. This gives rise to a current through R_d given by [29]:

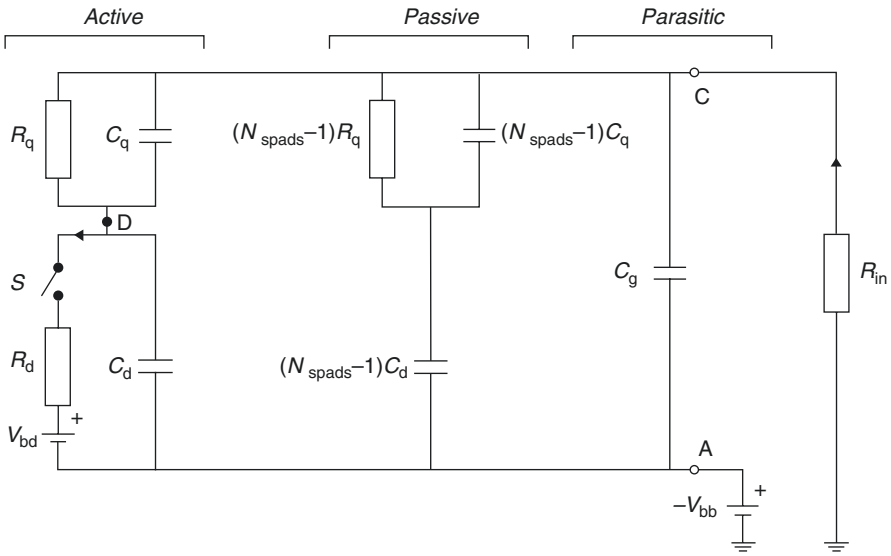

Fig. 3.3 SiPM equivalent electrical circuit

$$i_d(t) = I_0 e^{-t/\tau_d} \tag{3.2}$$

where $I_0 = V_{ob}/R_d$ and

$$\tau_d \approx R_d \left(C_d + C_q \right) \tag{3.3}$$

The current $i_d(t)$ causes the voltage at the node D between the diode and the quench resistor to decrease exponentially from the bias voltage V_{bb} to V_{bd} (relative to the anode). To hold the cathode at V_{bb}, the bias supply must deliver a correspondingly increasing current, which ultimately passes through the input resistance R_{in}. In the ideal case in which the measured signal is not affected by bandwidth or slew-rate limitations, its rise-time constant therefore equals τ_d, which can be in the range of tens of picoseconds.

The switch remains closed until $i_d(t)$ reaches the threshold value I_q below which the avalanche is no longer self-sustaining. At that point, the switch opens to mimic the quenching of the avalanche. The SPAD will now return to its initial state, and, consequently, the SiPM output current will return to zero. This process is governed by two time constants, corresponding with the two real poles of the small-signal transfer function of the equivalent circuit depicted in Fig. 3.3. Marano et al. [29] showed that the SiPM output signal can thus be modeled as a triple-exponential pulse with a rise-time constant τ_d and fall-time constants τ_{p1} and τ_{p2}. Figure 3.4

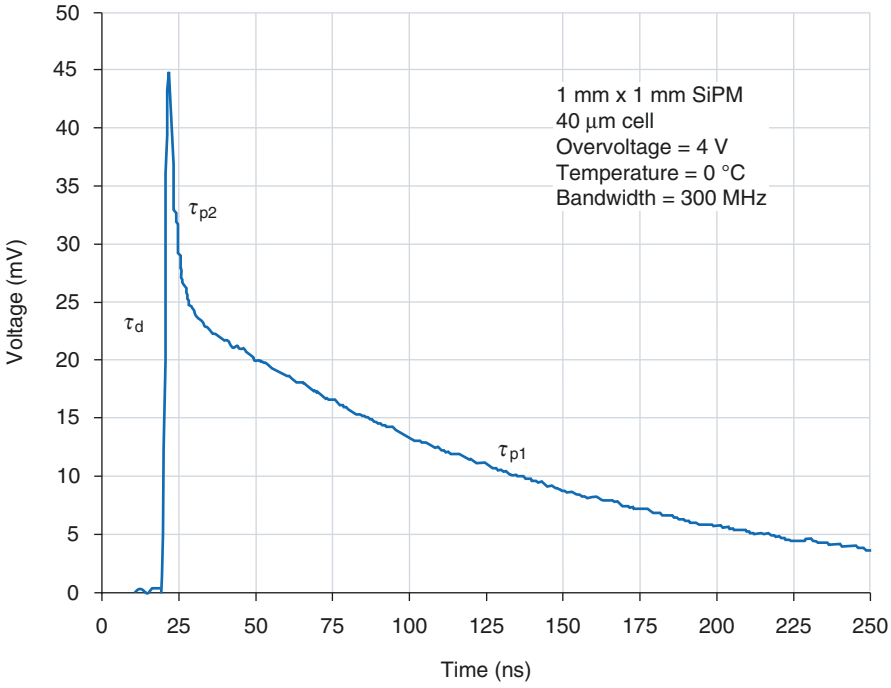

Fig. 3.4 Single-photon pulse of an analog SiPM. (Data from Acerbi and Gundacker [3], data kindly provided by Dr. F. Acerbi, Fondazione Bruno Kessler)

indicates how these time constants govern the different parts of the measured single-photon response of a 1 mm × 1 mm SiPM. One often speaks of τ_{p1} and τ_{p2} as the "slow" and "fast" components of the SiPM output signal, respectively. The slow time constant τ_{p1} is also called the SiPM recovery time and reaches a minimum value when the input impedance of the SiPM readout electronics approaches zero:

$$\begin{aligned} R_{in} &\to 0 \\ \tau_{pl} &\approx R_q \left(C_d + C_q \right) \end{aligned} \tag{3.4}$$

The recovery time τ_{p1} essentially parameterizes the recharging of C_d (and the corresponding discharging of C_q) through R_q. Typical values are in the order of 10–100 ns. A fast recovery time is beneficial for obtaining good time resolution with scintillators.

SiPM Timing Characteristics

The high internal gain and relatively fast response of SiPMs make them attractive for use in TOF-PET detectors. As with any type of photosensor, this requires that the first photons arriving at the sensor have a high chance of being detected. The PDE of a SiPM is often described as the product of its so-called fill factor (FF), the QE of the SPADs, and the trigger probability P_{trig}. The FF simply equals the sum of the SPAD active areas divided by the total device area. SiPMs typically have a FF in the range of 20–80%. The QE of a SPAD equals the probability that a photon incident on its active area creates an electron-hole (e-h) pair capable of initiating an avalanche. It may reach values above 90% within a limited range of wavelengths if proper antireflection coatings are applied. The QE curve can be matched with the scintillator emission spectrum by adapting the SPAD design. Finally, P_{trig} is the probability that an e-h pair triggers a pulse of adequate gain to be counted [12], which depends on the position at which the e-h pair is generated as well as the electric field shape and strength. It always increases with increasing V_{ob}.

SiPMs are currently available that (at sufficiently high V_{ob}) have a PDE larger than 50%, significantly exceeding that of vacuum photomultipliers. It is noted that the accurate measurement of SiPM PDE curves is not trivial and the results may depend on the method used. In particular, care should be taken to eliminate the influence of crosstalk and afterpulsing; these effects do not contribute to the efficiency of the sensor but represent sources of (correlated) noise.

In first-order approximation, the single-photon time resolution of a SiPM equals the SPTR of the SPADs it is made of. The SPTR of a SPAD improves with increasing V_{ob}. Values in the range of 20–50 ps FHWM are achievable [1, 7, 10, 11, 21, 33]. Several additional factors affect the SPTR of a SiPM. For example, spreads in V_{bd} and R_q give rise to SPAD gain dispersion and pulse shape variation, respectively. Different lengths and impedances of the metal traces that connect the SPADs to the SiPM output pad may cause additional pulse shape variation as well as a spread in pulse propagation delays [2, 16, 31, 40]. The DCR, which is proportional to the total number of SPADs, is another phenomenon that worsens the SPTR of a SiPM

compared to a single SPAD. Finally, unfavorable shaping of the single-photon signal due to SiPM parasitic impedances is an important complicating factor in SiPM SPTR measurements. In particular, the slower rise time and reduced amplitude of a SiPM compared to a single SPAD make the results more sensitive to electronic noise [25].

Cates et al. [10] recently measured the SPTR of a single 40 μm SPAD as well as 1 mm × 1 mm, 3 mm × 3 mm, and 4 mm × 4 mm SiPMs based on the same SPAD, using a front-end electronic readout design that minimized the influence of electronic noise. They obtained "intrinsic" SPTR values of about ~50 ps FWHM for both the single SPAD and the 1 mm × 1 mm SiPM. The corresponding values for the 3 mm × 3 mm and 4 mm × 4 mm SiPMs were somewhat larger but still well below 100 ps FWHM. In the same study, the SPTR of 3 mm × 3 mm SiPMs of other brands of SiPMs were found to be <150 ps FWHM in all cases.

3.4.3 Time Resolution of SiPM-Based Scintillation Detectors

The PDE and SPTR of contemporary SiPMs (see Sect. 3.4.2) are considerably better than those of vacuum photomultipliers (see Sect. 3.3), making SiPMs highly attractive single-photon sensors for use in TOF-PET devices. Yet, achieving optimum timing performance from a SiPM-based scintillation detector imposes a number of interesting challenges.

An important difference between SiPMs and PMTs is the shape of the single-photon signal. Whereas a PMT has a fall time in the order of ~ns, the recovery time of a SiPM typically is one or two orders of magnitude larger (see Fig. 3.4). For a PMT and a SiPM with equal gain, this implies that the amplitude of the SiPM output current is much lower. Moreover, when a given scintillator is coupled to both devices, the light signal is convoluted with the single-photon signal; therefore, the rise time at the output of the SiPM-based detector will be much slower.

Other factors that need to be taken into account include the SPAD gain spread, dark counts, and crosstalk. The theory of scintillation detector time resolution by Seifert et al. [42] attempts to incorporate all relevant properties of the photosensor and readout electronics, as well as the scintillation pulse shape, light yield, and energy resolution. This model can be applied to any type of scintillation crystal and photosensor.

Figure 3.5, taken from the original paper, compares the predicted and measured CRT of two SiPM-based LYSO:Ce detectors as a function of the trigger threshold and for different values of V_{ob}. The curves indicate that the threshold level and V_{ob} need to be jointly optimized. As the PDE and SPTR improve with increasing V_{ob}, the best CRT is found at $V_{ob} = 2.12$ V. The optimum threshold level appears to be only a few times higher than the single-SPAD pulse amplitude. As a result, the influence of amplitude walk on the time resolution is very small, favoring the use of simple, low-noise time-pickoff solutions such as a leading-edge discriminator for time pickoff.

Even though the Seifert model attempts to account for all factors influencing the time resolution of a SiPM-based scintillation detector, it appears that the shape of the curves in Fig. 3.5 is dominated by photon counting statistics, which have been

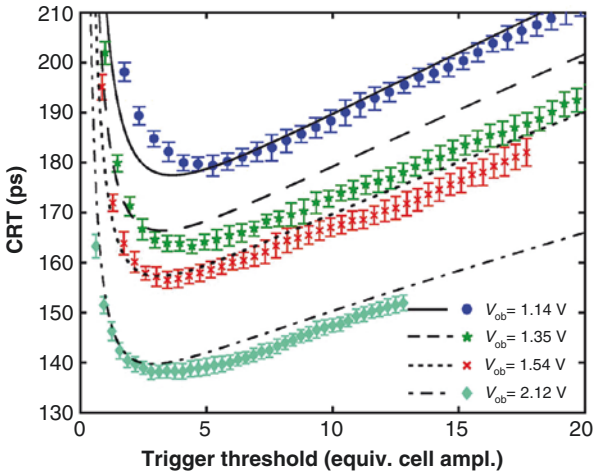

Fig. 3.5 Comparison between predicted (lines) and measured (symbols) CRT of two 3 mm × 3 mm × 5 mm LYSO:Ce crystals coupled to Hamamatsu MPPC-S10362-33-50C SiPMs, as a function of the trigger threshold and for different V_{ob}. (From Seifert et al. [42])

discussed in depth by the same authors in another paper [41]. This finding implies that the use of SiPMs allows TOF-PET detector developers to achieve CRT values close to the physical limit, as determined by the light yield and pulse shape of the scintillator, the transfer of the optical signal, and the PDE and SPTR of the SiPM. Indeed, it has been shown that CRT values of about 200 ps FWHM are feasible at whole-body system level when SiPMs are used to read out L(Y)SO:Ce crystals with a thickness of 20 mm or more [6, 46].

Achieving such excellent CRT values requires the use of optimized readout electronics to read out the SiPM signals. Most SiPM-based TOF-PET systems utilize application-specific integrated circuits (ASICs) for this purpose. A variety of ASICs has been developed in recent years, offering functionalities such as signal amplification, time pickoff, and energy determination, as well as secondary functions such as gain and offset regularization. Calo et al. [9] have recently reviewed the state of the art in ASIC development for SiPMs.

3.4.4 Digital SiPMs

Similar to analog SiPMs, digital SiPMs (dSiPMs) essentially consist of a two-dimensional array of SPADs. Instead of a passive quench resistor, however, an active quenching and recharge circuit is locally integrated with each SPAD, as indicated schematically in Fig. 3.6. Moreover, electronic circuits for the fully digital acquisition, processing, and readout of optical signals are integrated into the sensor. Several types of dSiPM have been developed in recent years, and first imaging devices based on dSiPMs have been realized. A comprehensive review of the main dSiPM technologies and their use in PET devices has been published by Schaart et al. [39].

The so-called SPAD/TDC arrays are among the earliest examples of photosensor chips based on microcells that integrate a SPAD and CMOS circuitry [47]. In such

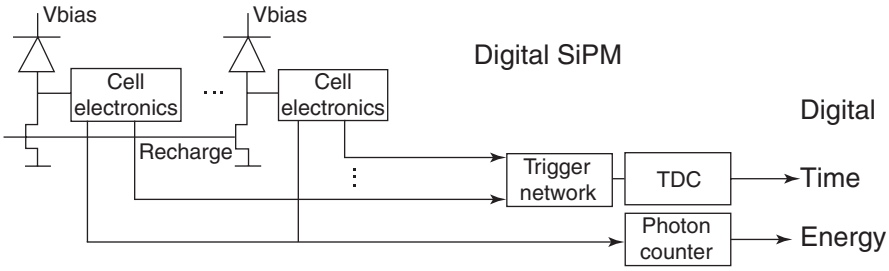

Fig. 3.6 Schematic representation of a digital SiPM circuit. (From Frach et al. [18], figure kindly provided by Dr. T. Frach, Philips Healthcare)

SPAD/TDC arrays, each SPAD is connected to its own time-to-digital converter (TDC), and the PDE of such devices is limited because of the large number of TDCs that take up most of the available area on the chip. Whereas SPAD/TDC arrays are useful in certain imaging applications, such as time-of-flight three-dimensional (3D) optical imaging, this makes them less suitable for the readout of scintillation crystals.

The first dSiPM for PET, introduced by Frach et al. [13, 18], reached a fill factor of ~50% by connecting a large group of SPADs via a trigger network to a single TDC, in such a way that it was possible to time stamp either the first, second, third, or fourth registered photon of a scintillation pulse. This early proof of concept was later used to develop the Philips Digital Photon Counter (DPC-3200), in which the fill factor was increased to more than 70% [14, 19].

Similar to analog SiPMs, the response of dSiPMs is nonproportional to the number of incident photons. The response of dSiPMs is not affected by afterpulsing, but saturation, crosstalk, and dark counts still play a role. The lower limit of the response of a dSiPM is equal to that of an analog SiPM and is given by Eq. (3.1). Van Dam et al. [44] derived and experimentally validated a more comprehensive model of the expected value as well as the variance of the number of counted scintillation photons in response to a given amount of energy deposited in a scintillator coupled to a dSiPM.

The breakdown of a SPAD in a dSiPM is detected locally, that is, by means of a discriminator integrated in the immediate vicinity of the SPAD. Compared to triggering on the output current of an analog SiPM, this makes the response of the timing circuit faster and less sensitive to the gain of the individual SPADs. This can be exploited to achieve more accurate timing, better sensor uniformity, and lower sensitivity to temperature drifts. Moreover, the local integration of each SPAD with logic circuitry enables the implementation of functionality to switch off noisy SPADs in order to reduce the overall DCR.

On the other hand, new factors that influence the device SPTR come into play in dSiPMs. Examples are the resolution of the on-chip TDC and its nonlinearity, which needs to be minimized through calibration. Furthermore, the SPTR may be affected by propagation time differences (skews) in the trigger network. Careful balancing of the trigger network therefore is required to obtain high time resolution [19, 28].

Brunner et al. [7] characterized the timing performance of complete sensor chips, single pixels, and individual SPADs of the DPC-3200 digital photon counting chip using a femtosecond laser. The SPTR of single SPADs was found to be 48 ps FWHM. Furthermore, the SPTR values of a single dSiPM pixel and an entire sensor chip were found to be equal to ~100 ps FWHM and ~170 ps FWHM, respectively, when the 20% noisiest cells were switched off.

Given the PDE and SPTR of a dSiPM, the time resolution that can be achieved when it is used to read out a scintillation detector is influenced by the rank(s) as well as the number of detected photon(s) used to derive the time stamp [42, 48]. Whereas for analog SiPMs the threshold level of the time-pickoff circuit attached to its output must be carefully optimized, in a dSiPM, this is the case for the logic operations applied to the digital timing signals produced by the microcells.

In summary, dSiPMs offer excellent low-level light-sensing properties in combination with many practical advantages, if properly designed for a given application. The on-chip integration of the light-sensing components with (near-) real-time data processing and readout circuits intrinsically makes the dSiPM a highly application-specific device, requiring careful optimization of the sensor design to the application of interest. Once optimized, an important advantage of the dSiPM concept is that the intrinsic sensor performance is relatively easily maintained at the system level, for example, when dSiPMs are used to read out a PET scanner consisting of tens of thousands of channels.

References

1. Acerbi F, Ferri A, Gola A, Cazzanelli M, Pavesi L, Zorzi N, Piemonte C. Characterization of single-photon time resolution: from single SPAD to silicon photomultiplier. IEEE Trans Nucl Sci. 2014;61:2678–86.
2. Acerbi F, Gola A, Ferri A, Zorzi N, Paternoster G, Piemonte C. Analysis of transit time spread on FBK silicon photomultipliers. J Instrum. 2015;10:P07014.
3. Acerbi F, Gundacker S. Understanding and simulating SiPMs. Nucl Instrum Methods Phys Res, Sect A. 2019;926:16–35.
4. Bengtson B, Moszynski M. Timing properties of scintillation counters. Nucl Instrum Methods Phys Res, Sect A. 1970;81:109–20.
5. Bisogni MG, Morrocchi M. Development of analog solid-state photo-detectors for positron emission tomography. Nucl Instrum Methods Phys Res, Sect A. 2016;809:140–8.
6. Borghi G, Tabacchini V, Bakker R, Schaart DR. Sub-3 mm, near-200 ps TOF/DOI-PET imaging with monolithic scintillator detectors in a 70 cm diameter tomographic setup. Phys Med Biol. 2018;63:155006.
7. Brunner SE, Gruber L, Hirtl A, Suzuki K, Marton J, Schaart DR. A comprehensive characterization of the time resolution of the Philips digital photon counter. J Instrum. 2016;11:P11004.
8. Budinger TF. PET instrumentation: what are the limits? Semin Nucl Med. 1998;28:247–67.
9. Calo PP, Ciciriello F, Petrignani S, Marzocca C. SiPM readout electronics. Nucl Instrum Methods Phys Res, Sect A. 2019;926:57–68.
10. Cates JW, Gundacker S, Auffray E, Lecoq P, Levin CS. Improved single photon time resolution for analog SiPMs with front end readout that reduces influence of electronic noise. Phys Med Biol. 2018;63:185022.
11. Cova S, Lacaita A, Ghioni M, Ripamonti G, Louis TA. 20-Ps timing resolution with single-photon avalanche-diodes. Rev Sci Instrum. 1989;60:1104–10.

12. Dautet H, Deschamps P, Dion B, Macgregor AD, Macsween D, McIntyre RJ, Trottier C, Webb PP. Photon counting techniques with silicon avalanche photodiodes. Appl Opt. 1993;32:3894–900.
13. Degenhardt C, Prescher G, Frach T, Thon A, de Gruyter R, Schmitz A, Ballizany R. The digital silicon photomultiplier - a novel sensor for the detection of scintillation light. IEEE nuclear science conference R 2383-6, 2009.
14. Degenhardt C, Zwaans B, Frach T, de Gruyter R. Arrays of digital silicon photomultipliers - intrinsic performance and application to Scintillator readout. 2010 IEEE nuclear science symposium conference record (Nss/Mic) 1954-6, 2010.
15. Delso G, Furst S, Jakoby B, Ladebeck R, Ganter C, Nekolla SG, Schwaiger M, Ziegler SI. Performance measurements of the Siemens mMR integrated whole-body PET/MR scanner. J Nucl Med. 2011;52:1914–22.
16. Dolinsky S, Fu G, Ivan A. Timing resolution performance comparison of different SiPM devices. Nucl Instrum Methods Phys Res, Sect A. 2015;801:11–20.
17. Donati S, Tambosso T. Single-photon detectors: from traditional PMT to solid-state SPAD-based technology. IEEE J Sel Top Quantum Electron. 2014;20.
18. Frach T, Prescher G, Degenhardt C, de Gruyter R, Schmitz A, Ballizany R. The digital silicon photomultiplier - principle of operation and intrinsic detector performance. IEEE nuclear science conference R 1959-65, 2009.
19. Frach T, Prescher G, Degenhardt C, Zwaans B. The digital silicon photomultiplier - system architecture and performance evaluation. 2010 IEEE nuclear science symposium conference record (Nss/Mic) 1722-7, 2010.
20. Gedcke DA, Mcdonald WJ. Design of constant fraction of pulse height trigger for optimum time resolution. Nucl Instrum Methods Phys Res, Sect A. 1968;58:253–60.
21. Ghioni M, Gulinatti A, Rech I, Zappa F, Cova S. Progress in silicon single-photon avalanche diodes. IEEE J Sel Top Quantum Electron. 2007;13:852–62.
22. Humm JL, Rosenfeld A, Del Guerra A. From PET detectors to PET scanners. Eur J Nucl Med Mol Imaging. 2003;30:1574–97.
23. Hyman LG. Time resolution of photomultiplier systems. Rev Sci Instrum. 1965;36:193.
24. Kapusta M, Lavoute P, Lherbet F, Rossignol E, Moussant C, Fouche F. Breakthrough in quantum efficiency of bi-alkali photocathodes PMTs. 2007 IEEE nuclear science symposium conference record, Vols 1–11, 73–7, 2007.
25. Knoll GF. Radiation detection and measurement. Hoboken: Wiley; 2010.
26. Lewellen TK. Recent developments in PET detector technology. Phys Med Biol. 2008;53:R287–317.
27. Lynch FJ. Basic limitation of scintillation-counters in time measurements. IEEE Trans Nucl Sci. 1975;22:58–64.
28. Mandai S, Charbon E. Timing optimization of a H-tree based digital silicon photomultiplier. J Instrum. 2013;8:P09016.
29. Marano D, Belluso M, Bonanno G, Billotta S, Grillo A, Garozzo S, Romeo G, Catalano O, La Rosa G, Sottile G, Impiombato D, Giarrusso S. Silicon photomultipliers electrical model extensive analytical analysis. IEEE Trans Nucl Sci. 2014;61:23–34.
30. Moszyński M, Kapusta M, Nassalski A, Szczęśniak T, Wolski D, Eriksson L, Melcher CL. New prospects for time-of-flight PET with LSO scintillators. IEEE Trans Nucl Sci. 2006;53: 2484–8.
31. Nagano T, Sato K, Ishida A, Baba T, Tsuchiya R, Yamamoto K. Timing resolution improvement of MPPC for TOF-PET imaging. IEEE nuclear science conference R 1577-80, 2012.
32. Nakamura K, Hamana Y, Ishigami Y, Matsui T. Latest bialkali photocathode with ultra high sensitivity. Nucl Instrum Methods Phys Res, Sect A. 2010;623:276–8.
33. Nemallapudi MV, Gundacker S, Lecoq P, Auffray E. Single photon time resolution of state of the art SiPMs. J Instrum. 2016;11:P10016.
34. Peng H, Levin CS. Recent developments in PET instrumentation. Curr Pharm Biotechnol. 2010;11:555–71.

35. Popova E, Buzhan P, Pleshko A, Vinogradov S, Stifutkin A, Ilyin A, Besson D, Mirzoyan R. Amplitude and timing properties of a Geiger discharge in a SiPM cell. Nucl Instrum Methods Phys Res, Sect A. 2015;787:270–4.
36. Renker D. Geiger-mode avalanche photodiodes, history, properties and problems. Nucl Instrum Methods Phys Res, Sect A. 2006;567:48–56.
37. Renker D, Lorenz E. Advances in solid state photon detectors. J Instrum. 2009;4:P04404.
38. Roncali E, Cherry SR. Application of silicon photomultipliers to positron emission tomography. Ann Biomed Eng. 2011;39:1358–77.
39. Schaart DR, Charbon E, Frach T, Schulz V. Advances in digital SiPMs and their application in biomedical imaging. Nucl Instrum Methods Phys Res, Sect A. 2016;809:31–52.
40. Seifert S, van Dam HT, Huizenga J, Vinke R, Dendooven P, Lohner H, Schaart DR. Simulation of silicon photomultiplier signals. IEEE Trans Nucl Sci. 2009;56:3726–33.
41. Seifert S, van Dam HT, Schaart DR. The lower bound on the timing resolution of scintillation detectors. Phys Med Biol. 2012;57:1797–814.
42. Seifert S, Van Dam HT, Vinke R, Dendooven P, Löhner H, Beekman FJ, Schaart DR. A comprehensive model to predict the timing resolution of SiPM-based scintillation detectors: theory and experimental validation. IEEE Trans Nucl Sci. 2012;59:190–204.
43. Szczęśniak T, Moszyński M, Świderski L, Nassalski A, Lavoute P, Kapusta M. Fast photomultipliers for TOF PET. IEEE Trans Nucl Sci. 2009;56:173–81.
44. Van Dam HT, Seifert S, Schaart DR. The statistical distribution of the number of counted scintillation photons in digital silicon photomultipliers: model and validation. Phys Med Biol. 2012;57:4885–903.
45. Van Dam HT, Seifert S, Vinke R, Dendooven P, Löhner H, Beekman FJ, Schaart DR. A comprehensive model of the response of silicon photomultipliers. IEEE Trans Nucl Sci. 2010;57:2254–66.
46. van Sluis JJ, de Jong J, Schaar J, Noordzij W, van Snick P, Dierckx R, Borra R, Willemsen A, Boellaard R. Performance characteristics of the digital biograph vision PET/CT system. J Nucl Med. 2019;60:1031.
47. Veerappan C, Richardson J, Walker R, Day-Uey L, Fishburn MW, Maruyama Y, Stoppa D, Borghetti F, Gersbach M, Henderson RK, Charbon E, Unabbreviated VC, Richardson J, Walker R, Fishburn MW, Maruyama Y, Stoppa D, Borghetti F, Gersbach M, Henderson RK, Charbon E. 2011 IEEE international solid-state circuits conference (ISSCC 2011). Piscataway, NJ: IEEE; 2011. p. 312–4.
48. Venialgo E, Mandai S, Gong T, Schaart DR, Charbon E. Time estimation with multichannel digital silicon photomultipliers. Phys Med Biol. 2015;60:2435–52.
49. Wiener RI, Kaul M, Surti S, Karp JS. Signal analysis for improved timing resolution with scintillation detectors for TOF PET imaging. 2010 IEEE nuclear science symposium conference record (Nss/Mic) 1991-5, 2010.
50. Wright T. The photomultiplier handbook. New York: Oxford University Press; 2017.

New-Generation Silicon Photomultiplier-Based Clinical PET/CT and PET/MR Systems

4

David F. C. Hsu and Craig S. Levin

4.1 Introduction to Multimodal PET Imaging Systems

Positron emission tomography (PET) is a functional imaging modality that enables the noninvasive interrogation of cellular and molecular signatures of diseases in living subjects [1]. It is commonly used in cancer management, where specific radiotracers are used to visualize and quantify regions of high uptake that are indicative of cancerous lesions [1–5].

Up until the year 2000, PET systems were used as standalone functional imaging systems. However, clinical studies have shown that the fusion of functional and structural imaging can help the diagnostic sensitivity and specificity beyond using each imaging modality alone [6]. In addition, PET image correction methods such as scatter and attenuation correction require structural information of the body that is not directly provided by PET emission data alone. Researchers have incorporated PET with structural imaging modalities such as CT and MRI in order to boost the diagnostic sensitivity and specificity over using PET alone [7, 8]. While separate PET and CT or MRI scans could provide both structural and functional information, maintaining the same patient alignment between the different scanners and associated image registration/fusion tasks was challenging. This led to the development of multimodal PET systems within a single scanner [9].

The first PET/CT system was developed by CTI PET Systems (now Siemens Healthineers), which mounted the BGO-based ECAT ART PET detectors on the same rotating gantry as a single-slice spiral CT scanner [10]. Simultaneous PET/

D. F. C. Hsu
Electrical Engineering and Radiology at Stanford University, Stanford, CA, USA
e-mail: fcdh@stanford.edu

C. S. Levin (✉)
Radiology/Physics/Electrical Engineering/Bioengineering at Stanford University, Stanford, CA, USA
e-mail: cslevin@stanford.edu

J. Zhang, M. V. Knopp (eds.), *Advances in PET*,
https://doi.org/10.1007/978-3-030-43040-5_4

MR systems were also first developed by Siemens with the avalanche photodiode (APD)-based Biograph mMR system [11]. However, these systems were incapable of time-of-flight (TOF) performance. GE introduced the first TOF-capable simultaneous PET/MR system with the SIGNA, which is based on silicon photomultiplier (SiPM) technology [12, 13].

The focus of this chapter is to describe the time-of-flight-capable SiPM-based detector module architecture and the role it plays in the next generation of multimodality PET systems. To demonstrate its benefits, we will focus on the design and performance of the state-of-the-art GE Discovery MI PET/CT system, whose design is based on this architecture. Finally, we will examine some clinical imaging comparisons and discuss some implications of this technology development in the clinical setting.

4.2 Clinically Driven PET System Design Trends

Nuclear medicine clinics are the major customers of commercial PET systems. The demands emerging from these clinics guide the design trends used in the development of commercial PET systems. For clinical applications, clinics want to reduce the amount of dose that the patients are exposed to for the patient well-being while reducing the scan time as much as possible in order to maximize throughput. Clinics that use PET systems for longitudinal cancer studies, dynamic/kinetic modeling studies, or neuroscience research require the PET system to be stable and quantitatively accurate over a long period of time. Finally, price demands drive developments toward reducing the cost of PET systems. In this section, we will relate the PET system development trends to their relevance to these market demands, which will serve as a foundation for the discussion of the SiPM-based PET detector architecture in the next section.

4.2.1 Time-of-Flight Performance

The most significant development focus of most current commercial PET systems being developed today is their time-of-flight (TOF) imaging capabilities. This is not surprising, because the image SNR boost offered by TOF is significant and allows for a reduction in patient dose or acquisition time while maintaining the same image quality [14]. In addition, new image reconstruction algorithms such as GE's Q. Clear block-sequential regularized expectation maximization can combine TOF information with regularization in order to produce a denoised image that is quantitatively accurate [15]. Currently, new commercial PET systems are released with sub-400 ps coincidence timing resolution performance.

Achieving TOF performance requires bright scintillation crystals with fast-decay times, as well as photodetectors with low jitter. BGO, which is a slow-decay crystal that has been historically used due to its cheap price and high 511 keV photon stopping power, has been gradually replaced by fast-decay, high light-yield crystals such

as LYSO. All of GE's TOF-capable multimodal PET systems, including the state-of-the-art Discovery MI PET/CT and SIGNA PET/MR systems, utilize lutetium-based scintillation crystals. On the photodetector side, SiPMs are solid-state photodetectors that can help to optimize time-of-flight performance.

4.2.2 Multimodality PET Detector Modules

The superior diagnostic performance of simultaneous multimodal PET/CT or PET/MR systems over standalone PET systems has made it necessary to develop PET detector modules that are compatible with either CT or MR systems in the same imaging bore. Even though they can be used in PET/CT systems, traditional vacuum-tube photodetector technology such as PMTs does not work in a magnetic field, making their integration into PET/MR systems challenging. The emergence of solid-state photodetectors operated in avalanche mode (APDs) and Geiger mode (SiPMs) has led to the development of detector modules that can work in PET/MR systems in addition to PET/CT systems.

Prior to the integration of SiPMs in PET block detectors, APDs were used as the magnetic-compatible photodetectors in simultaneous PET/MR systems such as the Siemens Biograph mMR [11]. However, APDs have challenges achieving fast timing performance, which limits their PET image quality compared to previous-generation TOF-capable PMT-based systems. GE's development of the SiPM-based TOF PET detector made it the first commercially available PET detector that was both magnetic compatible and TOF capable. Furthermore, the same basic detector module design could be used in both PET/CT and PET/MR systems, which reduced the overall system development costs.

4.2.3 Temperature Stability

Solid-state photodetectors such as APDs and SiPMs have signal gains that are heavily dependent on the device temperature in addition to their operating voltage. Because solid-state photodetectors have a smaller form factor and are more densely packed and usually also employ close-proximity power-consuming integrated readout electronics, heat dissipation and temperature stability in APD- or SiPM-based PET system designs become a larger issue compared to PMTs. Therefore, newer-generation PET systems need to be designed with cooling systems that are capable of stable temperature control over a long period of time [16, 17].

4.2.4 Improving Noise-Equivalent Count Rates

To reduce patient dose or acquisition time while maintaining the same image quality, the noise-equivalent count rate of the system needs to increase. One way to increase the number of recorded true events is to use fast-decay crystals like LYSO, which

have higher light yield that allows for better energy resolution, better time resolution, and slightly smaller crystal element size compared to a BGO-based system. This enables features such as 3D acquisition for higher sensitivity and TOF, both of which improve NECR. The fast decay also leads to reduction in the charge integration time and detector dead time, which reduces the probability of losing true events that arrive during the period of time when the detector is processing a given event.

We can see the NECR improvements offered by fast-decay crystals by comparing GE's lutetium-based Discovery MI and BGO-based Discovery IQ PET/CT systems. While both of these systems have a detector ring diameter of 74 cm, the Discovery IQ has a longer axial FOV of 260 mm and a crystal length of 30 mm, compared to the Discovery MI's nominal axial FOV of 200 mm and crystal element length of 25 mm. However, despite having a shorter axial FOV and a shorter crystal element, the Discovery MI has a peak NECR of 193.4 kcps, which is 56.4% higher than the 123.6 kcps NECR offered by the Discovery IQ [18, 19]. This example illustrates the NECR improvements offered by using fast-decay crystals such as the lutetium-based crystals used in the Discovery MI.

Another way to increase the NECR is to increase the solid angle coverage of the patient inside the PET system. This will yield a higher probability of capturing both annihilation photons that are emitted from the patient per radioactive decay, leading to a higher sensitivity. This can be accomplished in one of two ways: shrinking the PET ring diameter or increasing the axial FOV of the PET system. PET ring diameter has been decreasing over time as septa for 2D acquisition have been removed from systems. As an example, GE reduced the ring diameter between its Discovery STE and Discovery 600 PET/CT systems by 9% while keeping most of the other design parameters and components the same. This led to a 6.8% increase in sensitivity, 11.2% increase in the peak NECR, and a significant improvement in the contrast recovery capabilities of the system while reducing the number of crystals needed by 8.6% [20].

The lengthening of the axial FOV comes with increased cost, but the modular nature of PET detector blocks allows PET systems to offer customizable axial FOVs, which enable nuclear medicine clinics to select the axial FOV that they desire. The recently released SiPM-based Discovery MI PET/CT system offers three possible axial FOV configurations that nuclear medicine clinics can pick between depending on their needs. For example, by choosing the 15/20/25 cm axial FOV Discovery MI system, the sensitivity is 7.5/13.7/21.7 cps/kBq, while NECR is 100/181/283 kcps [21].

4.2.5 Summary

In summary, the SiPM-based block detector and fast-decay scintillation crystals can deliver improved PET imaging performance, through its TOF capabilities, stable detector gain through temperature control, and the improved NECR performance. Its modularity allows easy customization of axial FOVs, while it can be integrated into both PET/CT and PET/MR scanners to reduce development costs for the PET system manufacturers.

4.3 SiPM-Based Block Detector Architecture

In the SiPM block detector used in the GE Discovery MI PET/CT and SIGNA PET/MR systems, a 4 × 9 element LYSO crystal array is multiplexed to three arrays of Hamamatsu SiPMs, each with 3 × 2 pixels. Each crystal element is 3.95 mm (transaxial) by 5.3 mm (axial) by 25 mm (length), while each SiPM pixel is 2 × 2 mm in size. This detector architecture utilizes scintillation crystals coupled to a tapered light guide in order to achieve light-sharing multiplexing in their block detectors. By using light-sharing multiplexing, the number of photodetectors and readout channels needed for the readout of the block is reduced. Figure 4.1 shows an illustration of the different components of GE's SiPM-based block detector.

In the 20 cm axial FOV version of the D-MI system [18], 16 block detectors are packaged together to make one detector module, as shown in Fig. 4.2. GE also

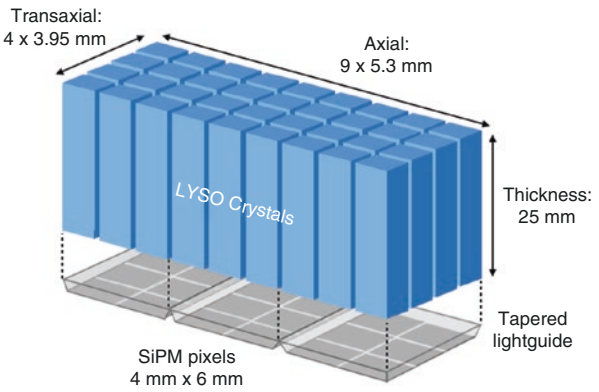

Fig. 4.1 A new-generation PET detector module. Each block detector is composed of 4 × 9 LYSO crystals arranged in an array, each of which is 3.95 mm × 5.3 mm × 25 mm, coupled to 3 SiPM Hamamatsu arrays through a tapered light guide. Each SiPM array has 3 × 2 pixels, and each pixel is 2 mm × 2 mm

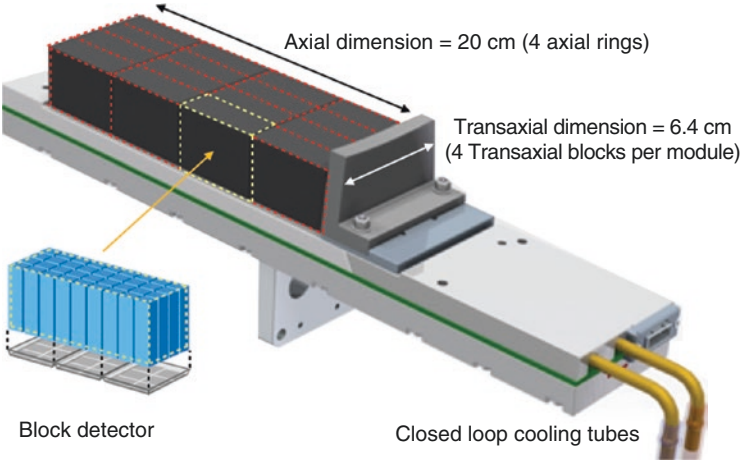

Fig. 4.2 PET detector module for the 20 cm axial FOV GE Discovery MI system. Each detector module is composed of 16 block detectors, arranged 4 by 4 in the axial and transaxial directions

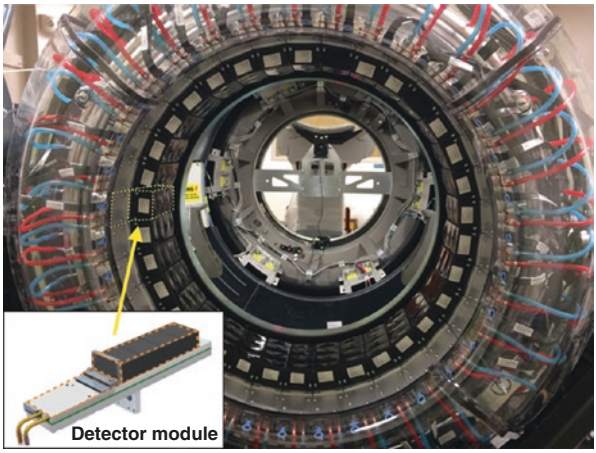

Fig. 4.3 The 20 cm axial FOV D-MI system is composed of 34 detector modules for a 74.4 cm inner detector ring diameter

offers the 15 cm and 25 cm axial FOV configurations of its D-MI system, which are composed of 3 and 5 block detectors, respectively, in the axial dimension. Each detector module shares one set of cooling tubes that help keep the SiPMs at a constant temperature of 19 degrees Celsius.

In the D-MI system, each PET ring is made up of 34 detector modules, with an overall detector ring diameter of 74.4 cm [18], while there are 28 detector modules in the PET ring of the SIGNA system, with a detector ring diameter of 62.4 cm [12]. Figure 4.3 shows the overall layout of the GE Discovery MI PET system.

4.4 Performance Characterization and Discussion

4.4.1 NEMA Characterization

The NEMA performance standard measures and characterizes important aspects of a PET system such as spatial resolution, sensitivity, noise-equivalent count rate, and image quality metrics like contrast recovery. These metrics are dependent on many factors such as the scintillation crystal and photodetector characteristics, ring diameter, axial FOV, crystal size and type, reconstruction algorithm, and image correction algorithms.

Table 4.1 presents the NEMA NU-2012 testing results of the Discovery MI PET/CT and the SIGNA PET/MR systems [12, 18], which are the two systems that utilize the SiPM-based block detector architecture as described above. The NEMA results of the previous-generation Discovery 690 PET/CT system are also included in the table as comparison [22]. The exact NEMA NU-2 testing methodology used for the results is presented elsewhere [23].

4.4.2 Clinical Instrumentation and Imaging Comparisons

Although the GE Discovery MI and SIGNA systems are both the first systems to use analog SiPM technology as the photodetector, much of the rest of the system block detector architecture remains the same as previous generations of PMT-based systems.

Table 4.1 NEMA NU-2 performance measurements of commercial multi-modality PET scanners

NEMA NU-2 measurement	GE Discovery MI [18]	GE SIGNA [12]	GE Discovery 690 [22]
System geometry			
Axial FOV (cm)	20 (15)	25	15.7
Transverse FOV (cm)	70	60	70 cm
Detector ring diameter (an)	74.4	62.4	81 cm
Crystal and photodetector details			
Crystal, transaxial dimension (mm)	3.95	3.95	4.2
Crystal, axial dimension (mm)	5.3	5.3	6.3
Crystal, thickness (mm)	25	25	25
Total number of crystals	19,584 (14,688)	20,160	13,824
Photodetector	SiPM	SiPM	PMT
Spatial resolution FWHM, FBF reconstruction			
Radial, 1 cm	4.10	4.46	4.7[a]
Tangential, 1 cm	4.9	4.08	4.7[a]
Axial, 1 cm	4.48	5.35	4.74
Radial, 10 cm	5.47	5.81	5.34
Tangential, 10 cm	4.49	4.44	4.79
Axial, 10 cm	6.01	6.75	5.55
Radial, 20 cm	7.53	8.42	NA
Tangential, 20 cm	4.90	5.27	NA
Axial, 20 cm	6.10	7.30	NA
Sensitivity			
Center of FOV (cps/kBq)	13.7 (7.5)	22.9	7.4
Count rate statistics			
Peak NECR (kcps)	193.4 (100)	214.8	139.1
Peak NEC activity (kBq/mL)	21.9 (20.6)	17.6	29.0
Peak NEC scatter fraction (%)	40.6	42.5	37
Accuracy of corrections			
Maximum absolute error (%)	3.14	3.5	2.09
Image quality, measured contrast recovery in spheres			
10 mm	53.7	36.5	44
13 mm	64.0	50.6	56
17 mm	73.1	60.0	65
22 mm	82.7	68.6	75
28 mm	86.8	80.7	87
37 mm	90.7	88.6	89
Timing and energy resolution			
Timing resolution (ps)	375.4	390	544.3
Energy resolution (%)	9.40	10.5	12.4

[a]Radial and tangential values are averaged together

By looking at the comparison of the D-MI and SIGNA systems with the older PMT-based Discovery 690 system which also employed lutetium-based crystals, we can isolate the effects of using the SiPM as the photodetector instead of using PMTs.

From the NEMA comparison between the 15 cm axial FOV D-MI and the D-690 systems shown in Table 4.1, we can see that the spatial resolution and sensitivity between

the two systems are similar, while the NECR and contract recovery coefficients are different. Even though the D-MI system has a lower peak NECR than the D-690, it requires a lower activity concentration level to reach peak NECR compared to the D-690. This indicates that the D-MI system is potentially better for low-dose clinical imaging than the D-690 system, which is consistent with the clinical trends of decreasing patient dose for scans. The contrast recovery coefficient of the image quality is better in the D-MI system compared to the D-690 system, which could be attributed to the improved timing resolution of the D-MI, leading to a better TOF SNR gain in the image quality.

For clinical comparisons, patients with clinical histories of melanoma and non-small cell lung cancer were scanned back-to-back on both the Discovery 690 and the 20 cm axial FOV Discovery MI systems for the purpose of restaging and metastatic evaluation [18]. Figures 4.4 and 4.5 show the resulting clinical images from

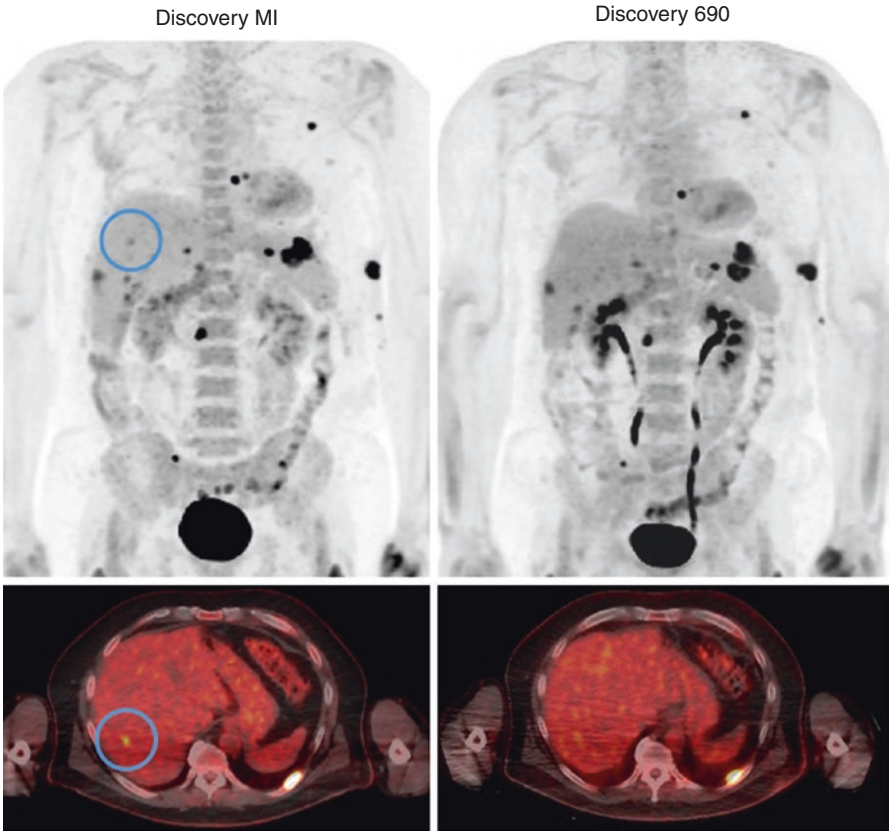

Fig. 4.4 Comparative clinical images from a patient with a clinical history of melanoma, injected with 298 MBq, 96-minute uptake, and scanned for 33 minutes on, first, the D-690 and then the D-MI system (without time adjustment for activity decay). Top row shows MIP images; bottom row shows transaxial fused slice images

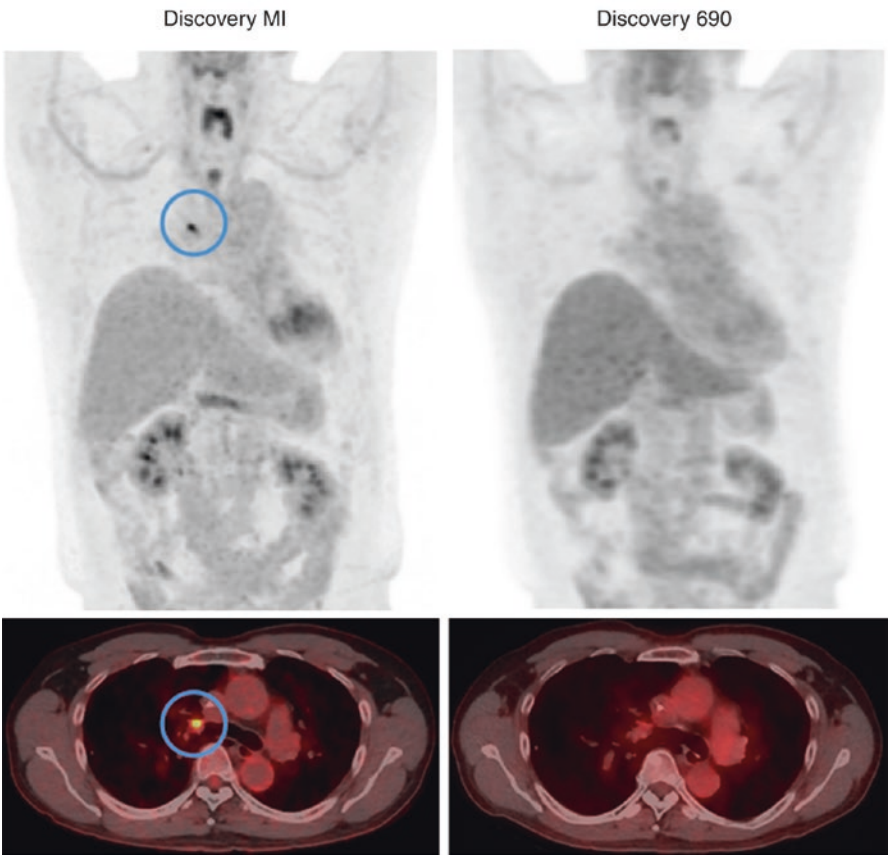

Fig. 4.5 Comparative clinical images from a patient with a clinical history of NSCLC, injected with 362 MBq, 84-minute uptake, and scanned for 12 minutes on, first, the D-690 and then the D-MI system (without time adjustment for activity decay). Top row shows MIP images; bottom row shows transaxial fused slice images

these scans. A visual observation of the two figures shows several lesions, shown by the blue circles, that are only visible in the Discovery MI image regardless of the reconstruction method used. This is an interesting observation, since the NEMA results suggest that both systems should have similar spatial resolution numbers. Although direct comparisons cannot be made due to different tracer uptake times and patient alignments, it is likely the improved performance is due to the Discovery MI's higher sensitivity, NECR, improved timing resolution, and CR of small lesions when compared to the 690. This improvement can help in diagnostics, surgery, radiotherapy planning, or quantitative studies on treatment effectiveness.

4.5 Conclusion

In this chapter, we have covered the historical trends in PET system and detector development and discussed the specific detector and system architecture of the SiPM-based GE Discovery MI PET/CT and SIGNA PET/MR systems. The results show that the incorporation of SiPMs in the block detector architecture of PET systems can reduce development costs and yield significant improvements in clinical image quality.

References

1. Bailey DL, Townsend DW, Valk PE, Maisey MN, editors. Positron emission tomography: basic sciences. London: Springer-Verlag; 2005.
2. Pimlott SL, Sutherland A. Molecular tracers for the PET and SPECT imaging of disease. Chem Soc Rev. 2011;40(1):149–62.
3. Schirrmeister H, Glatting G, Hetzel J, Nussle K, Arslandemir C, Buck AK, Dziuk K, Gabelmann A, Reske SN, Hetzel M. Prospective evaluation of the clinical value of planar bone scans, SPECT, and 18f-labeled NaF PET in newly diagnosed lung cancer. J Nucl Med. 2001;42(12):1800–4.
4. Fass L. Imaging and cancer: a review. Mol Oncol. 2008;2(2):115–52.
5. Schirrmeister H, Kuhn T, Guhlmann A, Santjohanser C, Horster T, Nussle K, Koretz K, Glatting G, Rieber A, Kreienberg R, Buck AC, Reske SN. Fluorine-18 2-deoxy-2-fluoro-D-glucose PET in the preoperative staging of breast cancer: comparison with the standard staging procedures. Eur J Nucl Med. 2001;28(3):351–8.
6. Eubank WB, Mankoff DA, Schmiedl UP, Winter TC, Fisher ER, Olshen AB, Graham MM, Eary JF. Imaging of oncologic patients: benefit of combined CT and FDG PET in the diagnosis of malignancy. Am J Roentgenol. 1998;171(4):1103–10.
7. Gerth HU, Juergens KU, Dirksen U, Gerss J, Schober O, Franzius C. Significant benefit of multimodal imaging: PET/CT compared with PET alone in staging and follow-up of patients with Ewing tumors. J Nucl Med. 2007;48(12):1932–9.
8. Pichler BJ, Kolb A, Naegele T, Schlemmer H-P. PET/MRI: paving the way for the next generation of clinical multimodality imaging applications. J Nucl Med. 2010;51(3):333–6.
9. Beyer T, Townsend DW, Brun T, Kinahan PE, Charron M, Roddy R, Jerin J, Young J, Byars L, Nutt R. A combined PET/CT scanner for clinical oncology. J Nucl Med. 2000;41(8):1369–79.
10. Townsend DW. Combined PET/CT: the historical perspective. Semin Ultrasound CT MR. 2008;29(4):232–5.
11. Delso G, Furst S, Jakoby B, Ladebeck R, Ganter C, Nekolla SG, Schwaiger M, Ziegler SI. Performance measurements of the Siemens mMR integrated whole-body PET/MR scanner. J Nucl Med. 2011;52(12):1914–22.
12. Grant AM, Deller TW, Khalighi MM, Maramraju SH, Delso G, Levin CS. NEMA NU 2-2012 performance studies for the SiPM-based ToF-PET component of the GE SIGNA PET/MR system. Med Phys. 2016;43(5):2334–43.
13. Levin CS, Maramraju SH, Khalighi MM, Deller TW, Delso G, Jansen F. Design features and mutual compatibility studies of the time-of-flight PET capable GE SIGNA PET/MR system. IEEE Trans Med Imaging. 2016;35(8):1907–14.
14. Karp JS, Surti S, Daube-Witherspoon ME, Muehllehner G. The benefit of time-of-flight in PET imaging: experimental and clinical results. J Nucl Med. 2008;49(3):462–70.
15. Lantos J, Mittra ES, Levin CS, Iagaru A. Standard OS-EM vs. regularized PET image reconstruction: qualitative and quantitative comparison using phantom data and various clinical radiopharmaceuticals. Am J Nucl Med Mol Imaging. 2018;8(2):110–8.

16. Yamamoto S, Satomi J, Watabe T, Watabe H, Kanai Y, Imaizumi M, Shimosegawa E, Hatazawa J. A temperature-dependent gain control system for improving the stability of Si-PM-based PET systems. Phys Med Biol. 2011;56(9):2873.
17. Freese DL, Vandenbroucke A, Innes D, Lau FWY, Hsu DFC, Reynolds PD, Levin CS. Thermal regulation of tightly packed solid state photodetectors in a 1 mm3 resolution clinical PET system. Med Phys. 2015;42(1):305–13.
18. Hsu DFC, Ilan E, Peterson WT, Uribe J, Lubberink M, Levin CS. Studies of a next-generation silicon-photomultiplier-based time-of-flight PET/CT system. J Nucl Med. 2017;58(9):1511–8.
19. Reynés-Llompart G, Gamez-Cenzano C, Romero-Zayas I, Rodriguez-Bel L, Vercher-Conejero JL, Marti-Climent JM. Performance characteristics of the whole-body discovery IQ PET/CT system. J Nucl Med. 2017;58(7):1155–61.
20. De Ponti E, Morzenti S, Guerra L, Pasquali C, Arosio M, Bettinardi V, Crespi A, Gilardi MC, Messa C. Performance measurements for the PET/CT Discovery-600 using NEMA NU 2-2007 standards. Med Phys. 2011;38(2):968–74.
21. Levin C, Peterson W, Ross S, Stearns C, Uribe J. PET performance as a function of axial field of view for a new silicon photomultiplier-based whole body TOF PET/CT system. J Nucl Med. 2016;57(supplement 2):200.
22. Bettinardi V, Presotto L, Rapisarda E, Picchio M, Gianolli L, Gilardi MC. Physical performance of the new hybrid PET/CT Discovery-690. Med Phys. 2011;38(10):5394–411.
23. National Electrical Manufacturers Association. NEMA NU-2 2012: performance measurement of positron emission tomographs, 2013.

Solid-State Digital Photon Counting PET/CT

5

Jun Zhang and Michael V. Knopp

5.1 Introduction

Vereos is the new-generation solid-state DPC PET/CT utilizing digital SiPMs (dSiPMs) for photon detection. The system was first introduced as a pre-commercial product at 2013 RSNA by Philips and has been released as commercial system since 2018. Different to analog SiPM detectors of which the pulses generated by multiple single-photon avalanche photodiodes (SPADs) are combined into one analog output signal requiring off-chip processing and Anger logic decoding [1], the Vereos system utilizes 1:1 coupling between scintillators and their own dSiPM detector sensors which removes the need of Anger logic position decoding [1–4]. Figure 5.1 shows an image of the Vereos system.

5.2 Architecture

5.2.1 Hardware

The Vereos PET/CT uses SiPM-based DPC technology for PET being coupled with a 64-slice helical CT of the Ingenuity PET/CT class. The CT portion uses a 40 mm axial field of view (FOV) with 3D dose modulation for low-dose CT capabilities integrated with both FBP reconstruction and an iterative reconstruction technique (iDose^4) as well as the metal artifact reduction for orthopedic implants (O-MAR) algorithm. The PET portion has 764 mm in diameter for the detector ring, with an axial FOV of 164 mm and an overlap of 64 mm (39%) between subsequent bed positions in axial. Compared to its previous PMT PET/CT systems (Ingenuity & Gemini, 180 mm axial FOV, 53% overlap), Vereos increases 16 mm

J. Zhang (✉) · M. V. Knopp
The Ohio State University, Columbus, OH, USA
e-mail: jun.zhang@osumc.edu; knopp.16@osu.edu

J. Zhang, M. V. Knopp (eds.), *Advances in PET*,
https://doi.org/10.1007/978-3-030-43040-5_5

Fig. 5.1 Philips Vereos PET/CT

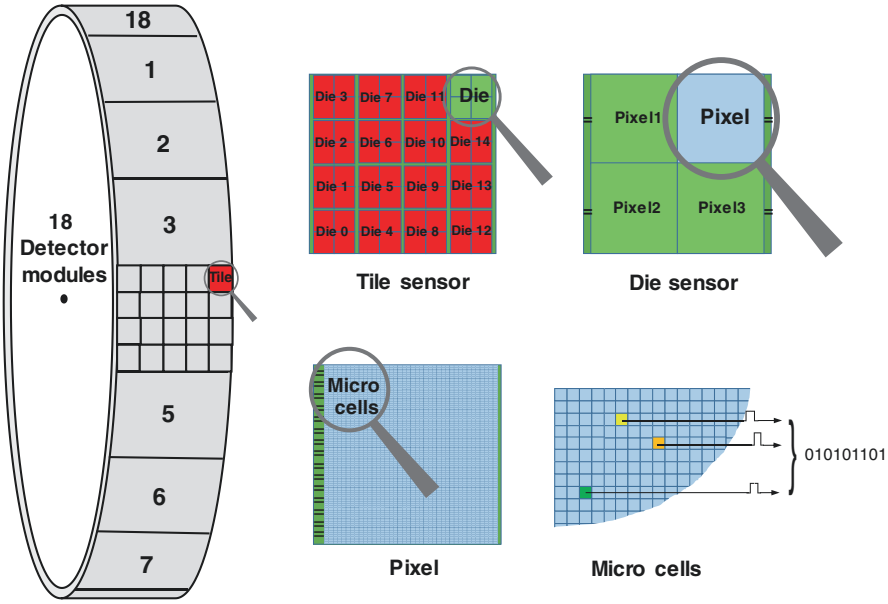

Fig. 5.2 An overview of the layout and architectural design of Vereos DPC PET detector

more in length of axial coverage when adding every one more bed position during scanning (e.g., 1 bed, 16 mm less; 2 beds, equal; 3 beds, 16 mm more; 4 beds, 32 mm more; etc.).

Figures 5.2 and 5.3 show an overview of the Vereos PET detector design. The PET ring is composed of 18 flat detector modules with 4 by 5 array dSiPM detector tiles on each module. There are 4 by 4 matrix of silicon sensor dies (chip) on each tile and 2 by 2 matrix of DPC detector cells (silicon pixels) on each die, with 3200 SPAD (microcells) integrated on each silicon pixel. Every pixel on the die couples

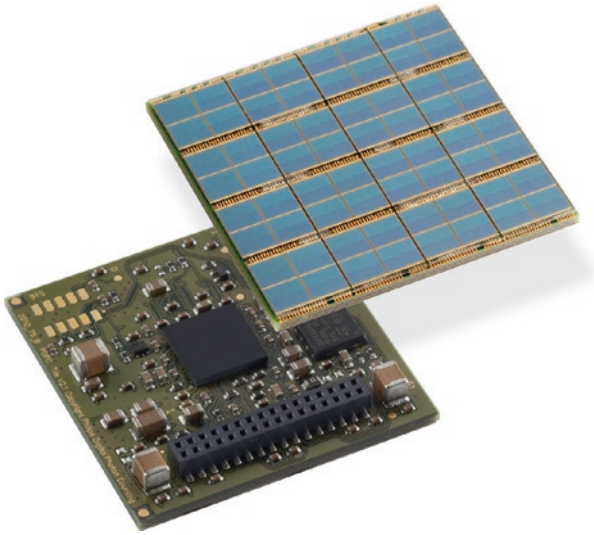

Fig. 5.3 Philips DPC tile sensor with sensor front side (top) and back side (bottom)

directly to a 3.86 × 3.86 × 19 mm^3 LYSO crystal forming 64 couplings (8 by 8) on each tile and a total of 23,040 couplings with 73,728,000 microcells on the entire detector ring.

5.2.2 Philips Digital Photon Counting (PDPC)

The DPC technology that Vereos uses is called Philips Digital Photon Counting (PDPC) which utilizes DPC3200 as the photon counter (see Sects. 1.3.3) [3–5]. For the name "digital," it refers to digital SiPM-based photon detection which is different to analog SiPM based. It is a digital SiPM technology combining SPAD and CMOS technologies together for fully integrated detector design and digital signal generation [5]. That is, each SPAD (microcell) is provided with an active circuit which is able to quench the discharge when a cell is fired by light photons. It allows every cell to be individually activated or inactivated and enables the detection and counting of the breakdown of individual SPADs on-chip, so light photons can be counted directly by the chip giving a pure binary digital signal (0 or 1, Fig. 5.2) without the need for amplification or off-chip analog-to-digital signal processing [3–5]. Some of the fundamentals and principles of digital SiPM technology are introduced in Chap. 3.

For Vereos, the 16 individual die sensors of each tile have the same breakdown voltage which needs only a single bias voltage supply for the tile. The field programmable gate array (FPGA) on the back of each tile (Fig. 5.3) is used to configure its individual die sensors and perform post-processing for timestamp and photon counter, ensuring the proper clock distribution, data collection and concentration, TDC linearization, as well as saturation and skew correction [5].

The die sensor is the piece of silicon device performing the actual data acquisition and photon counting. A single die (with 2 by 2 pixels) contains 100 rows and

128 columns of microcells (SPADs, or the Geiger-mode cells) and delivers the photon count values and a twin time-to-digital converter (TDC) for timestamp generation. Every microcell can detect single scintillation photon being converted into a pure binary output signal measured by the on-chip photon counter and timer. The number of microcells recording a photon is read out as the total number of photons detected by a pixel. As each cell can only detect one photon per acquisition, the number of cells per pixel also defines the maximum photon count value (up to 3200 photons between two cell recharge cycles) [3–6].

Background noise, or say dark count rate (DCR), is measured and managed effectively at the individual SPAD level. The biggest contribution to the overall sensor DCR is caused by only a small percentage of the cells (~10% of the cells are responsible for 70–80% of DCRs). A flash memory chip on the tiles stores calibration data and the inhibit maps to disable individual cells on the sensor dies. On the back of the tile PCB, a temperature sensor is available, which, e.g., can be used to adjust the bias voltage during operation to the current tile temperature. Disabling high dark count rate cells on a small active sensor area leads to significantly reduced overall sensor DCR; therefore, the overall DCR can be greatly reduced by switching off the noisiest cells [3, 5].

For PDPC, each die sensor operates independently from the other sensors. The sensor operates autonomously by running through a configurable event acquisition sequence, which is started by an internal trigger, and the trigger signal defines the moment of timestamp [4, 6]. Only those die sensors that detect sufficient photons reaching the configured thresholds will start the acquisition sequence (Fig. 5.4). In the beginning, a die sensor is in the "ready state," where all its microcells are fully charged, and the system waits for the start of the photon events until a trigger occurs. When the number of photons detected in a silicon pixel becomes higher than the configured threshold, it prompts a timestamp to be saved and begins a validation process to detect a user-configured number of further photons within a certain time. If this validation threshold is exceeded, there is a subsequent integration period before a readout process sends data (four photon count values, one per silicon pixel on the die, and one timestamp per event) to a readout buffer. After readout, the microcells are recharged so that the die is ready for further data acquisition. If the validation threshold was never reached, all microcells are immediately recharged and go back to the "ready state." At the end, the photon counter is read out by summing overall detected photons with a timestamp, and the whole process is entirely digital without need of signal amplification.

5.3 Reconstruction

PET reconstruction of Vereos uses list-mode-based TOF OS-EM algorithm with blobs as basic functions [7, 8]. It utilizes a Monte Carlo–based scatter simulation for scatter correction [9] and Casey averaging for smoothed random estimation [10]. The system applies 2.0 ns, 4.0 ns, and 4.6 ns coincidence windows depending on the transaxial FOVs (256 mm for brain, 576 mm for average size body, and 676 mm for large size body). PET reconstruction with isotropic voxels in standard definition

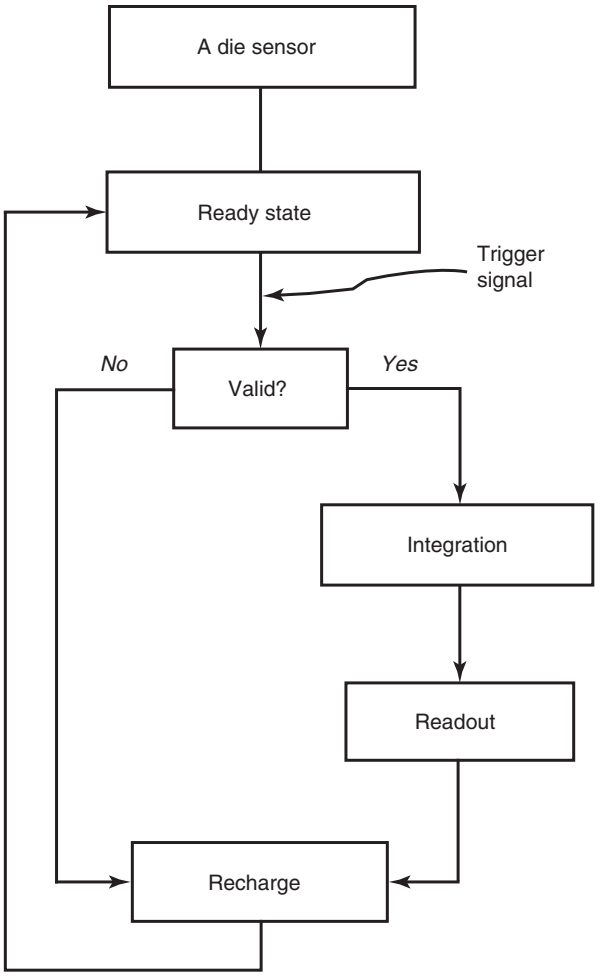

Fig. 5.4 Single event-based data acquisition sequence on each die sensor of the investigated PDPC PET system

(SD) ($4 \times 4 \times 4$ mm^3), high definition (HD) ($2 \times 2 \times 2$ mm^3), and ultrahigh definition (UHD, research only) ($1 \times 1 \times 1$ mm^3) is provided to form 144×144, 288×288, and 576×576 matrix PET images for 576 mm FOV PET. Optional point spread function (PSF) includes Richardson–Lucy, maximum-likelihood resolution recovery implementation, and Gaussian filtering [11–13] that are available for reconstruction, with iteration number and kernel width adjustable. An example of clinical PET on Vereos reconstructed using different voxel sizes compared to the PET performed on Gemini is demonstrated in Fig. 5.5.

For CT reconstruction, dose management is simplified with Philips Healthcare's DoseWise philosophy and the advances embodied in the Ingenuity. A fourth-generation iterative reconstruction technique named *iDose*^{4} [14] is used to provide significant improvements in image quality combined with dose reduction capabilities. A metal artifact reduction for orthopedic implants algorithm (O-MAR) is

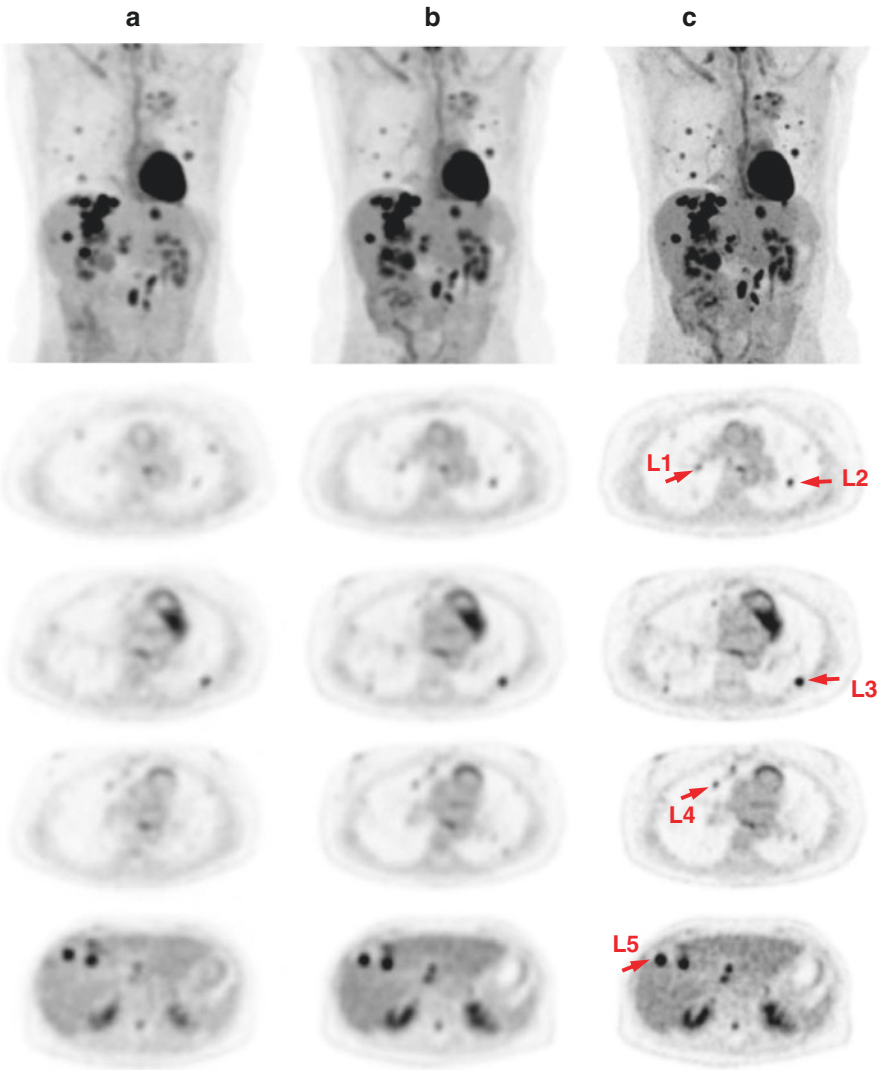

	SUV_{peak}	%	SUV_{peak}	%	SUV_{peak}
L1	0.69	49%	1.03	80%	1.24
L2	1.00	21%	1.21	50%	1.50
L3	2.40	8%	2.59	40%	3.35
L4	0.88	19%	1.05	65%	1.45
L5	4.55	17%	5.33	56%	7.12

Fig. 5.5 Intraindividual comparison of (**a**) SD PET (on Gemini, 75 min p.i., 3i33s) with (**b**) SD PET (on Vereos, 103 min p.i., 3i15s) and (**c**) UHD PET (on Vereos, 103 min p.i., 3i13s) for a clinical patient with extensive metastatic disease in the lung and the liver (BMI = 18.5, 503 MBq FDG, 90 s/bed). (Images were reconstructed using 3D OS-EM TOF)

integrated and optional which can be used as a secondary output for overcoming metal artifacts in addition to the default regular reconstruction. The width of various filtering kernels is adjustable during CT reconstruction.

5.4 Quality Control

PET daily QC procedures use a small, low-activity ^{22}Na source centered in the PET detector field of view (FOV). The daily QC process automatically checks hardware sensors for PET voltages, currents, and temperatures and then performs a short acquisition of PET coincidence events, typically acquiring about 200 million counts. Energy and timing resolution are automatically calculated from event histograms. Energy window was set at 88–120% of 511 keV (450–613 keV), and the coincidence-timing window was set at 4 ns with a delayed coincidence window technique utilized to estimate the random coincidences. Energy histograms with 4 keV bins are used to calculate the energy centroid and width (FWHM). TOF resolution (FWHM) was calculated with a timing histogram with 19.6 ps wide bins [4, 15]. Since the daily QC source is at the center of the FOV, the actual TOF between opposing detector crystals is zero. This results in a timing histogram centered on zero with a width equal to the system TOF resolution. This allowed to use the daily QC count rate as a measure of relative system stability by decay correcting for the 2.6-year ^{22}Na half-life and normalizing to the count rate at the first time point [15]. An average time needed for performing daily PET QC over 12 months is about 10 min.

5.5 System Performance Measurements

5.5.1 Spatial Resolution

Table 5.1 demonstrates the NEMA NU2-2012 [16] spatial resolution of the dPET system, ranging from 3.88 mm and 4.20 mm (in FWHM at 1 cm radial offset in axial and transaxial) to 4.60 mm, 5.75 mm, and 4.92 mm (in FWHM at 20 cm radial offset in axial, transverse radial, and transverse tangential).

Typically, the spatial resolution of a PET system can be parameterized as

$$\mathrm{SR} = K_\mathrm{r} \times \sqrt{R_\mathrm{i}^2 + R_\mathrm{p}^2 + R_\mathrm{a}^2 + R_\mathrm{l}^2}$$

where K_r is usually a factor of 1.2–1.5 that resulted from reconstruction [17], R_i is the intrinsic resolution given by $d/2$ with d as the crystal width, R_p is the error due to positron range (~0.2 mm for 18F), R_a is the error from PET noncollinearity given by 0.0022D with D as the ring diameter, and R_l is the decoding error due to Anger logic positioning localization [18, 19]. Vereos removed the need for Anger logic position decoding due to the 1:1 coupling design; therefore, there is no related degradation in distortions and edge effects ($R_\mathrm{l} = 0$). K_r is adjusted to be 1.43–1.54 for Vereos PET based on measured spatial resolution results.

Table 5.1 NEMA spatial resolution of Vereos

Spatial resolution												
	OSU						QIMP[20]					
	FWHM			FWTM			FWHM			FWTM		
Direction	1 cm	10 cm	20 cm	1 cm	10 cm	20 cm	1 cm	10 cm	20 cm	1 cm	10 cm	20 cm
Axial	3.88	4.22	*4.62*	8.36	8.47	*9.16*	4.17	4.39	4.6	8.8	9.08	9.21
Transverse (radial)	4.2	4.47	*5.75*	8.3	8.8	*10.31*	4.24	4.55	5.84	8.4	8.87	10.43
Transverse (tangential)	4.2	4.36	*4.92*	8.3	8.78	*10.26*	4.24	4.35	4.92	8.4	8.97	9.96

Spatial resolution is measured in millimeters with radial offset at 1 cm, 10 cm, and 20 cm

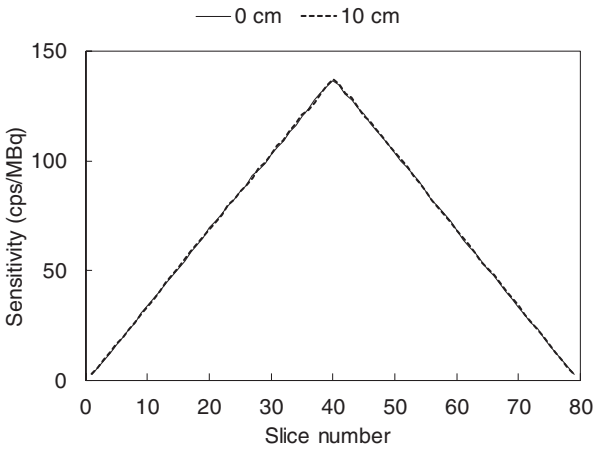

Fig. 5.6 Axial sensitivity profile of Vereos measured in the center of FOV and at 10 cm radial offset

5.5.2 Sensitivity

The average sensitivity of Vereos at the center and 10 cm radial offset the center was 5.5 cps/kBq and 5.5 cps/kBq (measured at OSU, Fig. 5.6) as well as 5.1 cps/kBq and 5.2 cps/kBq (measured at QIMP [20]).

Compared to PMT PET/CT systems (Gemini TF and Ingenuity TF), Vereos reduces the axial FOV from 180 mm to 164 mm, PET overlap from 53% to 39%, and number of crystals by ~20%; these factors lead to a reduced NEMA sensitivity. The clinical performance, however, demonstrated improved image quality and lesion detectability of PET. The observation is consistent to our findings on reducing system sensitivity through sparse-ring configurations on Vereos [21]. Several potential reasons may contribute to this. First, NEMA sensitivity measures system's ability to convert photons to raw counts which takes into account the quantity instead of quality of counts; the reduction of NEMA sensitivity leads to fewer counts instead of worse counts. Second, the PDPC technology enables on-chip light photon detection and direct digital signal output at individual SPAD level without asking for off-chip signal processing; such design minimizes signal noises and

improves the quality of counts. Last but not least, the SNR gain from the excellent 310 ps TOF timing compensates for the somewhat reduced NEMA sensitivity, and this can be articulated by an "effective sensitivity" concept, as follows:

$$S_{\text{eff}}(A) = S_{\text{NEMA}}(A) \times G_{\text{TOF}} / f_{\text{d}}$$

$$G_{\text{TOF}} = \frac{D}{\Delta x} = \frac{2D}{c\,\Delta t}$$

where S_{eff} is the activity-dependent effective sensitivity, S_{NEMA} is the NEMA sensitivity, G_{TOF} is the TOF gain, c is the speed of light, and Δt is the timing resolution, as well as f_{d} is the dead time correction factor. The Vereos system presents robust effective sensitivity which contributes to improved image quality from "better" counts instead of "more" counts. An example of effective sensitivity comparison between PMT PET and DPC PET is shown in Fig. 5.7.

5.5.3 NECR and Count Performance

The overall count loss measurements of Vereos are shown in Fig. 5.8. The measured peak NECR was about 153 kcps at 54 kBq/mL with the corresponding scatter fraction of 32.2%. The system peak true count rate was 878 kcps at 83.2 kBq/mL. With the

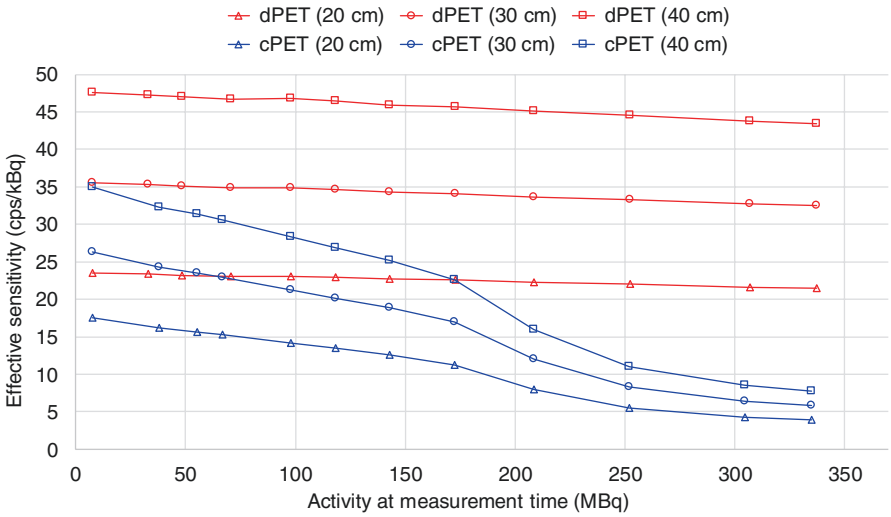

Fig. 5.7 Effective sensitivity of Vereos (dPET) versus Gemini (cPET) as a function of ^{18}F-FDG activities for object diameters of 20, 30, and 40 cm measured using NEMA NEC phantom-based methods [22, 23]. Although Vereos has lower NEMA sensitivity than Gemini, it revealed a much higher (1.3–5.5 × gain) and very robust effective sensitivity over 7–337 MBq ^{18}F-FDG on Vereos than Gemini

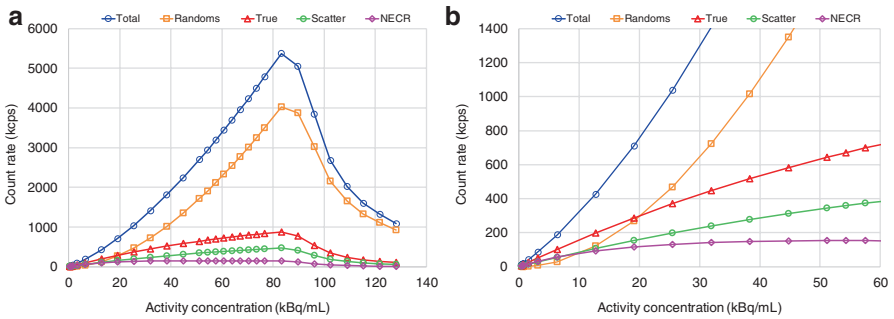

Fig. 5.8 NEMA count rate measurements of total, randoms, true, and NECR as a function of activity concentration in different scales (**a**. 0–140 kBq/mL; **b**. Zoom in with 0–60 kBq/mL range). 3180 MBq ^{18}F was used

introduced 1:1 coupling and vastly increased number of signal processing units, it allows the system to achieve a high peak true count rate with ultrawide dynamic range of activities. It is of note that typically an FDG administration of 259–740 MBq (7–20 mCi) is being widely used in clinical oncology PET in the USA, which indicates a 3.5–10 kBq/mL activity concentration for an average size patient of 75 kg. The capability of Vereos to handle much higher count rates at 10–80 kBq/mL levels would dedicatedly benefit high count rate imaging performance such as cardiac perfusion PET using ^{82}Rb, etc.

5.5.4 TOF Timing Resolution

Figure 5.9 shows the timing resolution measurements of Vereos. The benefit of TOF PET has been well established and became a benchmark technology [24, 25]. The timing resolution was measured at 310 ps when using the ^{22}Na point source in daily QC and 320 ps when using the NEMA NU2-2018 approach [26]. The line source inside the scatter phantom is potentially not perfectly straight and uniformly centered; therefore, its vibrations might cause fluctuation and degradation (~10 ps worse) than the point source-based measurement. As shown in Fig. 5.9b, the timing resolution is very robust for Vereos, while it has a big degradation for the Gemini system when increasing activity concentrations. It indicates that robust and stable SNRs maintain better for the PDPC system than PMT system which eventually contribute to excellent image quality of PET.

Table 5.2 summarizes the system characteristics of Vereos compared to PMT-based PET/CT systems.

5.6 Clinical Applications

5.6.1 Low-Dose PET

Radiation dose of PET is primarily determined by the amount of the radiopharmaceutical administered. While most efforts in PET/CT dose reduction have been predominantly focused on the CT component in the last decades, efforts in reducing

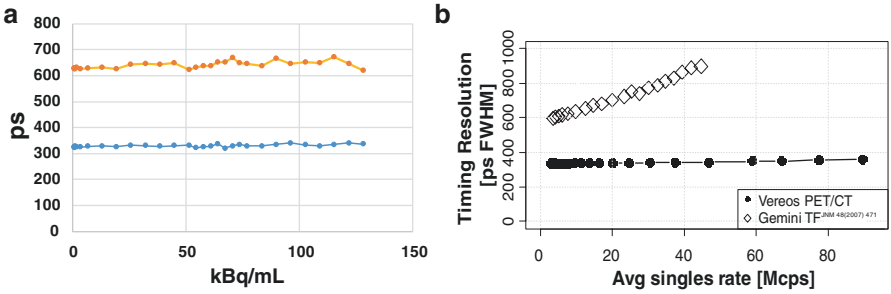

Fig. 5.9 Timing resolution of Vereos. (**a**) Timing resolution (in FWHM and FWTM) measured using NEMA NU2-2018 approach. (**b**) Comparison of timing resolution as a function of increasing activity concentration (or singles rate): Vereos versus Gemini

Table 5.2 Comparison of PET/CT system characteristics: SiPM-based versus PMT-based

PET/CT model	Vereos TF	Ingenuity TF [27]	Gemini TF [28]
Photo detector	SiPM	PMT	PMT
Number of detectors	23,040	420	560
Scintillator	LYSO	LYSO	LYSO
Number of crystals	23,040	28,336	28,336
Crystal size (mm^3)	3.86 × 3.86 × 19	4 × 4 × 22	4 × 4 × 22
Ring diameter (cm)	76.4	90.0	90.3
Axial FOV (cm)	16.4	18.0	18.0
Plane spacing (mm)	1, 2 or 4	2 or 4	2 or 4
TOF timing resolution (ps)	310	502	585
Sensitivity (cps/kBq)	5.5	7.3	6.6
Transverse resolution @ 1 cm (mm)	4.1	4.8	4.8
Transverse resolution @ 10 cm (mm)	4.4	5.1	5.2
Axial resolution @ 1 cm (mm)	3.9	4.7	4.8
Axial resolution @ 10 cm (mm)	4.2	5.2	4.8
Peak NECR (kcps @ kBq/mL)	153 @ 54.3	124.1 @ 20.3	125 @ 17.4
Energy resolution (%)	11.2	11.1	11.5
Scatter fraction at peak NECR (%)	32.2	36.7	27

PET dose have become increasingly important and practicably available [29–33]. The appearance of the emerging solid-state PET/CT systems strengthens such efforts and interest. Figure 5.10 demonstrates examples of low dose (185 MBq/5 mCi) compared to the SOC dose (481 MBq/13 mCi) FDG PET of clinical oncology patients. It revealed that Vereos can successfully provide uncompromised image quality and lesion detectability of PET at 62% reduction of FDG dose from the default SOC.

5.6.2 Fast PET Scanning

Fast scanning allows patients to spend less time on the scanner table to improve patient comfort, reduce motion artifacts, enhance overall patient experiences, and increase

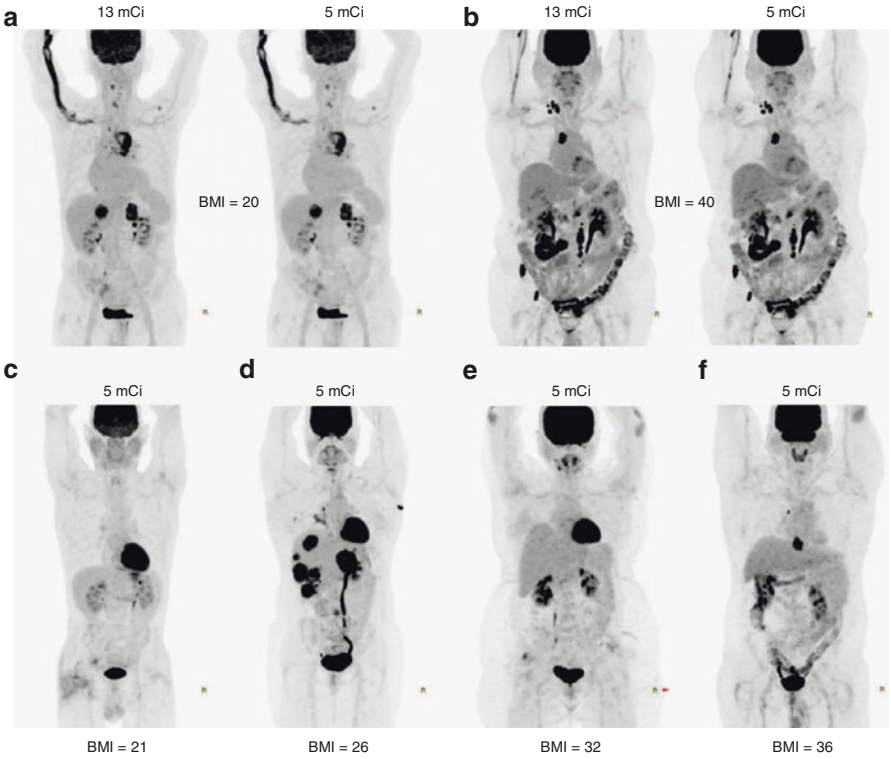

Fig. 5.10 Feasibility of low-dose ^{18}F-FDG PET of clinical oncology patients performed on Vereos with 90 s/bed and reconstructed in HD (2 × 2 × 2 mm^3). The digital MIP PET images showed intraindividual comparison between 13 mCi (actual) and 5 mCi (simu) FDG PET for patient **a** (BMI = 20) and patient **b** (BMI = 40). Lesions on the 13 mCi PET images can all be clearly identified on the 5 mCi PET images without compromising overall image quality. Investigational low-dose FDG PET scans (5 mCi) for validation were performed from below normal to obese patients (**c**, **d**, **e**, and **f**), and even the sub-centimeter FDG-avid lesion conspicuity in the right mediastinum (Patient **f**) is detectable with the Vereos system

the clinical volume. Vereos spends ~15% less time than Gemini or Ingenuity for a typical clinical "nose to mid-thigh" whole-body scanning (1–1.2 m). When further reducing the frame duration (time per bed position) utilizing the advantages of solid-state DPC technology, the acquisition speed can be even faster. Figure 5.11 shows an example of uncompromised image quality of PET at one-tenth the acquisition time.

5.6.3 Low Counts Density PET Simulation

Both low-dose PET and fast PET scanning lead to PET with relatively low counts density. It is challenging and also unethical to practically perform

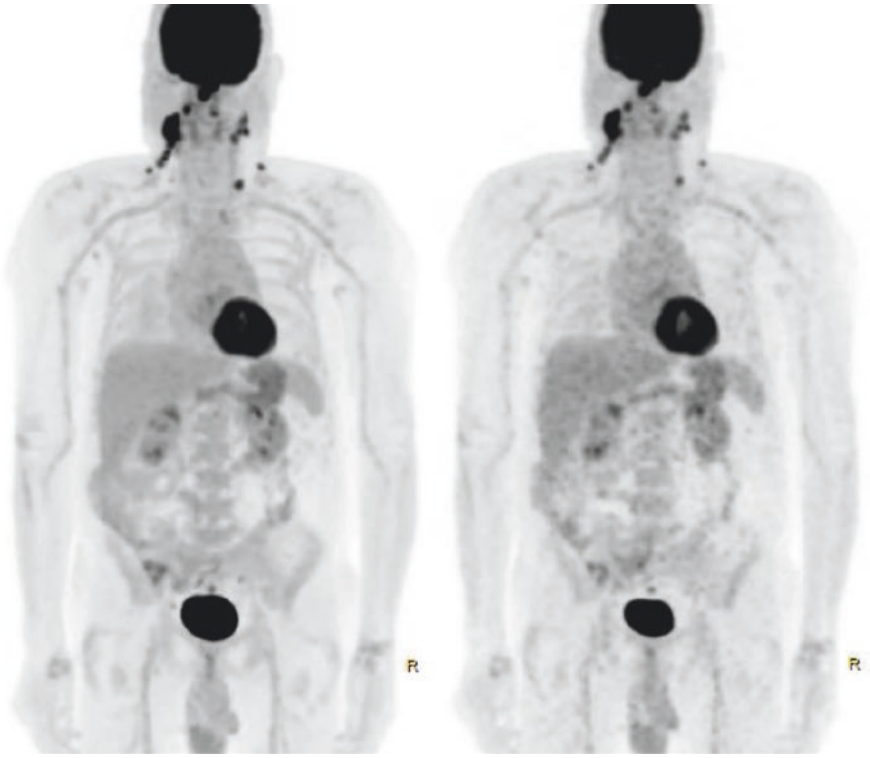

Fig. 5.11 Intraindividual comparison of ^{18}F-FDG PET (498 MBq) of a patient with head and neck cancer and metastatic disease. PET imaging was performed on Vereos with 90 s/bed followed by a 9 s/bed acquisition and reconstructed in $4 \times 4 \times 4$ mm^3. All lesions including small ones are clearly identified on the 9 s/bed PET, which required a total of 1.5 min scan time and saved 90% table time compared to the 90 s/bed (15 min in total) scan

investigational PET imaging by giving patient, especially pediatric, with either different doses or repeated scans of different frame durations via sequential imaging protocols. These difficulties make the performance of dose or speed finding studies challenging especially when there are established SOC procedures and clinical protocols that would be disrupted. It necessitates simulation approaches to enable such for systematic assessment via intraindividual and apple-to-apple comparison.

There are usually several ways of extracting partial counts from the acquired PET raw data to simulate low counts density PET. Figure 5.12 shows an example of using time-, space-, order-, and randomization-based approaches for low counts density PET simulation on Vereos, while Fig. 5.13 shows the corresponding clinical demonstration [34].

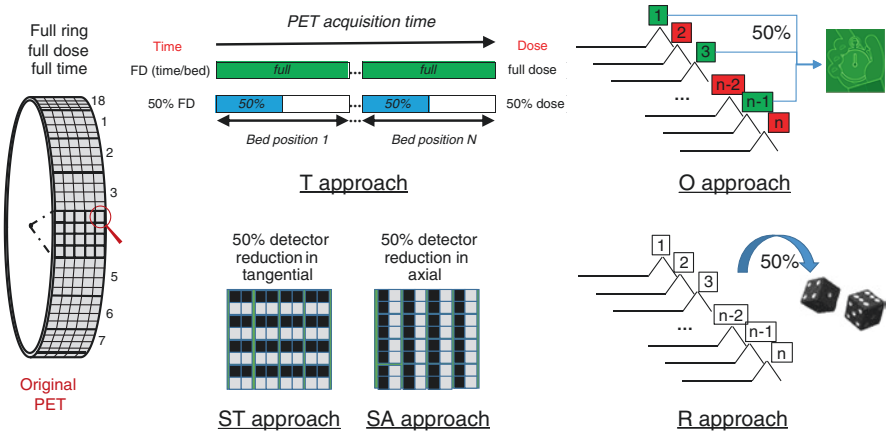

Fig. 5.12 Example of low counts density PET simulation on Vereos with 50% counts reduction using (1) time-based (T approach), half frame duration per bed position; (2) space-based, sparse-ring configurations with every other detector disabled in tangential (ST approach) and axial (SA approach); (3) order-based (O approach), every other prompt event in order is extracted; and (4) randomization-based (R approach), 50% counts by random event selection using a "dice" method

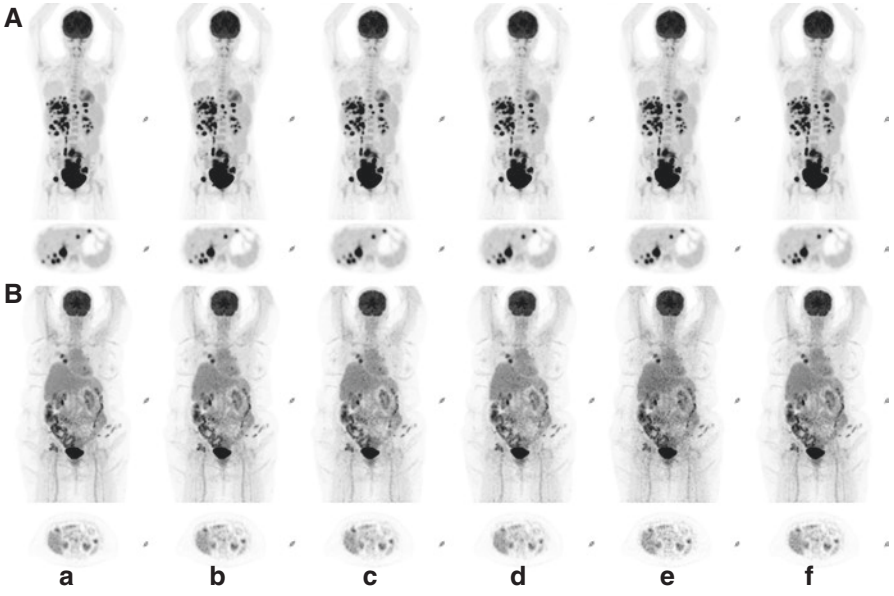

Fig. 5.13 Simulated PET with 50% counts density (b–f) using T-, ST-, SA-, O-, and R- approaches, separately, compared to the original PET (a) of oncology patient **a** (BMI = 14, 436 MBq FDG, 90 s/bed) and patient **b** (BMI = 40, 417 MBq FDG, 90 s/bed)

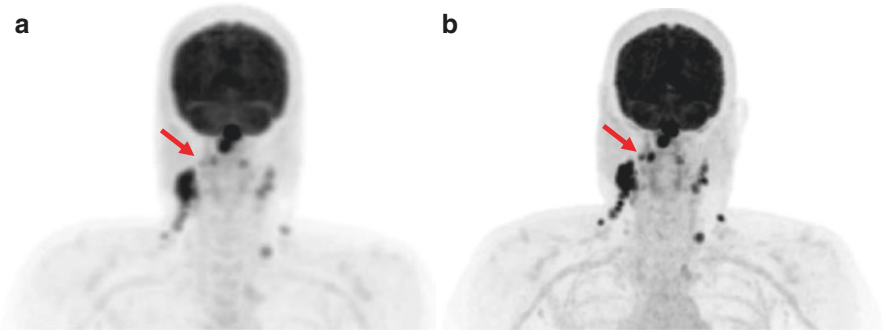

Fig. 5.14 Comparison of lesion detectability between analog PET (Gemini) in SD (**a**) and digital PET (Vereos) in HD (**b**) for a patient with head and neck cancer. The digital PET/CT was performed first (63 min p.i.), and the analog PET was performed thereafter (84 min p.i.), with 498 MBq ^{18}F-FDG and 90 s/bed. ^{18}F-FDG uptake of lymph nodes is enhanced on the digital PET with one of the small nodules (red arrow) being detected by the digital system but not the analog system. This case illustrates the capability of digital PET technology to substantially improve lesion detectability and diagnostic confidence

5.6.4 Lesion Detectability

Lesion detectability is the key and essential for physicians to diagnose, stage, and monitor therapy in oncology patients and molecular imaging. It has been challenging to reliably identify small lesions on PET due to potential limitations on the spatial resolution (conspicuity differentiation), voxel size (PVE), timing resolution (SNR), and reconstruction (CNR, etc.) using PMT-based conventional PET/CT systems. Utilizing the new-generation solid-state PET detection technology and advanced reconstruction algorithms, image can be generated with improved lesion detectability and diagnostic confidence over the analog PET/CT in oncological patients and even better for sub-centimeter lesions [35–37]. Figure 5.14 shows an example of PET lesion detectability of Vereos versus Gemini.

5.7 Conclusion

The PDPC PET enables every digital photon counter sensor to be directly coupled to a single scintillator and leads to higher count rate detection efficiency across a more uniform scintillator distribution compared to conventional PMT PET. The individual PDPC detector controlling greatly reduces the impact of count rate-dependent pileup on energy and timing resolution and provides highly stable performance across a large dynamic range of count rates.

The Vereos system demonstrates excellent performance characteristics and stability which promotes clinical opportunities of providing improved image quality, lesion detectability, diagnostic confidence, and promising capabilities for performing

faster and lower dose PET. The high-definition reconstruction appears to be of major clinical relevance for improved lesion detectability and characterization of lesion heterogeneity without increasing diagnostic ambiguity. It is expected that the system will be developed with larger axial FOV in its future generation.

References

1. Frach T, Prescher G, Degenhardt G, Gruyter R, Schmitz A, Ballizany R. The digital silicon photomultiplier – principle of operation and intrinsic detector performance. In: Nuclear science symposium conference record, N28-5; 2009.
2. Degenhardt C, Zwaans B, Frach T, Gruyter R. Arrays of digital silicon photomultipliers - intrinsic performance and application to scintillator readout. In: Nuclear science symposium conference record (NSS/MIC). IEEE; 2010. https://doi.org/10.1109/NSSMIC.2010.5874115.
3. Schaart DR, Charbon E, Frach T, Schulz V. Advances in digital SiPMs and their application in biomedical imaging. Nucl Inst Methods Phys Res A. 2016;809:31–52.
4. Zhang J, Maniawski P, Knopp MV. Performance evaluation of the next generation solid-state digital photon counting PET/CT system. EJNMMI Res. 2018;8(1):97. https://doi.org/10.1186/s13550-018-0448-7.
5. Haemisch Y, et al. Fully digital arrays of silicon photomultipliers (dSiPM) – a scalable alternative to vacuum photomultiplier tubes (PMT). Phys Procedia. 2012;37:1546–60.
6. Truly digital PET imaging: Philips proprietary Digital Photon Counting technology. Philips Healthcare: Eindhoven; 2016.
7. Wang W, Hu Z, Gualtieri EE, Parma MJ, Walsh ES, Sebok D, et al. Systematic and distributed time-of-flight list-mode PET reconstruction. Proc Nucl Sci Symp Conf Rec. 2006;3:1715–7.
8. Popescu LM, Lewitt RM. Ray tracing through a grid of blobs. IEEE Nucl Sci Symp Conf Rec. 2004;6:3983–6.
9. J. Ye, X. Song and Z. Hu, Scatter correction with combined single-scatter simulation and Monte Carlo simulation for 3D PET. In: 2014 IEEE Nuclear Science Symposium and Medical Imaging Conference (NSS/MIC). Seattle, WA; 2014. pp. 1–3.
10. Casey ME, Hoffman EJ. Quantitation in positron emission computed tomography. A technique to reduce noise in accidental coincidence measurements and coincidence efficiency calibration. J Comput Assist Tomogr. 1986;10:845–50.
11. Richardson WH. Bayesian-based iterative method of image restoration. J Opt Soc Am. 1972;62:55–9.
12. Lucy LB. An iterative technique for the rectification of observed distributions. Astron J. 1974;79:745–65.
13. Zhang B, Olivier P, Lorman B, Tung C. PET image resolution recovery using PSF-based ML-EM deconvolution with blob-based list-mode TOF reconstruction. J Nucl Med. 2011;52(Supplement 1):266.
14. iDose^4 iterative reconstruction technique. Philips Healthcare: Eindhoven; 2011.
15. Vereos PET/CT: focusing on high performance. Philips Healthcare: Eindhoven; 2018.
16. NEMA NU 2-2012: performance measurements of positron emission tomographs (PETs). National Electrical Manufacturers Association: Rosslyn; 2013.
17. Huesman RH. The effects of a finite number of projection angles and finite lateral sampling of projections on the propagation of statistical errors in transverse section reconstruction. Phys Med Biol. 1977;22:511.
18. Saha GB. Performance characteristics of PET scanners. In: Basics of PET imaging. New York: Springer; 2010.
19. Moses WW. Fundamental limits of spatial resolution in PET. Nucl Inst Methods Phys Res A. 2011;648:S236–40.

20. Rausch I, Ruiz A, Valverde-Pascual I, Cal-González J, Beyer T, Carrio I. Performance evaluation of the Philips Vereos PET/CT system according to the NEMA NU2-2012 standard. J Nucl Med. 2018; https://doi.org/10.2967/jnumed.118.215541.
21. Zhang J, Knopp MI, Knopp MV. Sparse detector configuration in SiPM digital photon counting PET: a feasibility study. Mol Imaging Biol. 2018; https://doi.org/10.1007/s11307-018-1250-7.
22. Mao Y, Miller M, Bai C, et al. Evaluation of a TOF resolution measurement method using standard NEMA NEC phantom. J Nucl Med. 2017;58(supplement 1):436.
23. Wang GC, Li X, Niu X, Du H, Balakrishnan K, Ye H, et al. PET timing performance measurement method using NEMA NEC phantom. IEEE Trans Nucl Sci. 2016;63(3):1335–42.
24. Karp JS, Surti S, Daube-Witherspoon ME, Muehllehner G. The benefit of time-of-flight in PET imaging: experimental and clinical results. J Nucl Med. 2008;49(3):462–70.
25. Conti M. Focus on time-of-flight PET: the benefits of improved time resolution. Eur J Nucl Med Mol Imaging. 2011;38(6):1147–57.
26. NEMA NU 2-2018: performance measurements of positron emission tomographs (PET). National Electrical Manufacturers Association: Rosslyn; 2018.
27. Kolthammer JA, Su KH, Grover A, Narayanan M, Jordan DW, Muzic RF. Performance evaluation of the ingenuity TF PET/CT scanner with a focus on high count-rate conditions. Phys Med Biol. 2014;59(14):3843–59.
28. Surti S, Kuhn A, Werner ME, Perkins AE, Kolthammer J, Karp JS. Performance of Philips Gemini TF PET/CT scanner with special consideration for its time-of-flight imaging capabilities. J Nucl Med. 2007;48(3):471–80.
29. Zhang J, Binzel K, Ross P, Hall N, Knopp MV. An anatomical adaptive acquisition approach (A5) for PET/CT. J Nucl Med. 2011;52:424.
30. Alessio AM, Sammer M, Phillips GS, Manchanda V, Mohr BC, Parisi MT. Evaluation of optimal acquisition duration or injected activity for pediatric 18F-FDG PET/CT. J Nucl Med. 2011 Jul;52(7):1028–34.
31. Schaefferkoetter JD, Yan J, Townsend DW, Conti M. Initial assessment of image quality for low-dose PET: evaluation of lesion detectability. Phys Med Biol. 2015;60(14):5543–56.
32. Yan JH, Schaefferkoetter J, Conti M, Townsend D. A method to assess image quality for Lowdose PET: analysis of SNR, CNR, bias and image noise. Phys Med Biol. 2015;60(14):5543–56.
33. Gatidis S, Schmidt H, la Fougère C, Nikolaou K, Schwenzer NF, Schäfer JF. Defining optimal tracer activities in pediatric oncologic whole-body 18F-FDG-PET/MRI. Eur J Nucl Med Mol Imaging. 2016;43(13):2283–9.
34. Zhang J, Zhang B, Knopp MV. Low counts density PET simulation using time-, space-, order- and randomization-based approaches on a SiPM digital photo counting TOF PET/CT. In: IEEE nuclear science symposium and medical imaging conference (NSS/MIC); 2019 Nov 30.
35. Nguyen NC, Vercher-Conejero JL, Sattar A, Miller MA, Maniawski PJ, Jordan DW, et al. Image quality and diagnostic performance of a digital PET prototype in patients with oncologic diseases: initial experience and comparison with analog PET. J Nucl Med. 2015;56(9):1378–85.
36. Wright CL, Binzel K, Zhang J, Knopp MV. Advanced functional tumor imaging and precision nuclear medicine enabled by digital PET technologies. Contrast Media Mol Imaging. 2017;5260305. https://doi.org/10.1155/2017/5260305.
37. López-Mora DA, Flotats A, Fuentes-Ocampo F, Camacho V, Fernández A, Ruiz A, et al. Comparison of image quality and lesion detection between digital and analog PET/CT. Eur J Nucl Med Mol Imaging. 2019;46(6):1383–90.

Siemens Biograph Vision 600

6

Michael E. Casey and Dustin R. Osborne

6.1 Introduction

This chapter is devoted to the Siemens Biograph Vision 600. The Vision is the latest generation of PET/CT from Siemens Healthineers and the first to use silicon photomultipliers (SiPMs) as the light sensing mechanism in the PET detectors. In addition, the CT unit is the Siemens Definition with up to 128 slices. Both the PET and CT are integrated into a single water-cooled unit with integrated operator software. This chapter describes the architecture, physical performance, and clinical performance of the system shown in Fig. 6.1.

Fig. 6.1 The Siemens Biograph Vision 600

M. E. Casey (✉) · D. R. Osborne
Siemens Medical Solutions, Knoxville, TN, USA

University of Tennessee Graduate School of Medicine, Knoxville, TN, USA
e-mail: michael.e.casey@siemens.com

J. Zhang, M. V. Knopp (eds.), *Advances in PET*,
https://doi.org/10.1007/978-3-030-43040-5_6

6.2 Architecture

Hardware Description

The most important component of a PET system is the detector. In the Vision, the detector consists of an array of 3.2 × 3.2 × 20 mm lutetium oxyorthosilicate [1] (LSO) crystals packaged as 20 crystals radially and 10 crystals axially. As shown in Fig. 6.2, the detector is further subdivided into mini-blocks of 5 × 5 crystals optically coupled to a 4 × 4 array of SiPMs. The 16 × 16 mm array of SiPMs completely covers the 16 × 16 mm array of LSO crystals. Light is contained within a mini-block using 3M ESR reflector [2]. A custom analog application-specific integrated circuit (ASIC) coupled directly to the SiPM array senses the gamma ray arrival time and encodes crystal position for each mini-block. The time pickoff signals from four mini-blocks are combined and sent to one time digitizer (TDC). For each mini-block, the energy signals are combined with a charge weighting scheme that encodes the crystal location. Further weighting of the mini-block signals ultimately produces four position signals that are digitized by four analog-to-digital converters (ADCs).

A detector electronics assembly (DEA) contains 16 detectors (two radially by eight axially) along with the TDCs and ADCs for time and position determination. Nineteen DEAs are arranged in an 82 cm diameter cylinder to form the tomograph. When a gamma ray strikes a crystal, the DEA determines which crystal was involved and the time the event was detected to within 13.02 picoseconds. If the energy of the event is within the preset energy window, the arrival time, crystal position, and gamma ray energy information is transmitted from the DEA to the coincidence processing unit via optical fiber.

When a 511 keV gamma ray strikes an LSO crystal, the gamma may scatter out of the initial crystal to an adjacent crystal. As long as the gamma ray scatters within

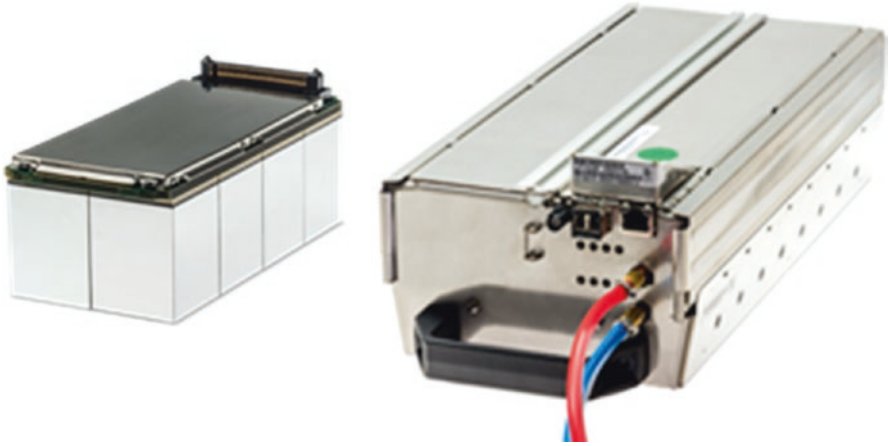

Fig. 6.2 Left, the detector with SiPM. Right, a detector electronics assembly containing 16 detectors and associated electronics

Table 6.1 Biograph Vision 600 physical characteristics

Crystal size	3.2 × 3.2 × 20 mm
Crystals per ring	760
Number of crystal rings	80
Detector ring diameter	82 cm
Axial length	26.3 cm
Time window	4.73 ns
Energy window	435–585 keV

a mini-block, all of the energy will be conserved, and the event will be positioned to the center of the energy spread. The mini-block is a fairly small group of crystals so there is a reasonable chance the event could scatter out of the mini-block. In the case the event does scatter to an adjacent mini-block within the detector, the DEA adds the energy from both mini-blocks and positions the event in the crystal with the highest energy, preserving that event.

The time, position, and energy information of each single event are transmitted from the DEAs to the coincidence processing unit. This unit forms coincident events by comparing the arrival times of the single events. Two events form a coincident event if the arrival times are within 4.73 nanoseconds. The line connecting the two crystals forming the coincident event intersects the positron annihilation. The difference in arrival times further localizes the annihilation to a region along the line. Each coincident event contains the time and position information along with the energy of the two single events. A fiber-optic transmits the coincident events to the reconstruction and acquisition computer where they are stored in order of occurrence (list mode).

There is a possibility that two single events will randomly occur with arrival times less than 4.73 nanoseconds apart. These events are indistinguishable from the true coincidence events. To estimate the number of randomly occurring events, each pair of events is also tested to find which pairs fall into a delayed time window. Since the delayed window rejects any events due to positron annihilations, the total number of events falling in the delayed window will be an accurate estimate of the number of randomly occurring events.

As stated earlier, the detector is most important component of a PET system. Table 6.1 presents a summary of the key physical characteristics of the Biograph Vision 600.

6.3 Data Processing

6.3.1 Data Organization

Raw data are initially stored in list mode. The list contains the events, elapsed time information, bed position information, and physiological gating information. For static imaging, the list can be converted to a sinogram and stored. For other more complex imaging, the histogramming occurs during the reconstruction process.

A static sinogram consists of 520 elements, 50 radial angles, 815 (direct and oblique) planes, 33 prompt, and one delayed time bin. Each time bin is 143.2 picoseconds or 2.1 cm. All 33 bins encompass a time window of 4.73 nanoseconds. As random events occur independently, only one time bin is needed. To estimate the number of randomly occurring events in a prompt time bin, the total in the random bin is simply divided by the number of prompt bins.

TOF information localizes the annihilation to a region along the line of response. Each radial angle of the sinogram can be thought of as an uncorrected sample of the final image where the radial direction is high resolution and the time direction is a lower resolution. In the case of the Biograph Vision, the 3.2 mm crystals allow a radial bin of 1.6 mm. In the orthogonal direction, the 143.2 picosecond bin allows a sampling of 2.1 cm. Each radial angle is a different sample of the same image. When images from adjacent angles are overlaid, many of the pixels coincide and can be added. Combining adjacent angles allows fewer radial and azimuthal sinogram angles with no loss in reconstructed resolution [3–5]. For this reason, the number of transaxial angles can be reduced to 50. This reduction ultimately allows faster reconstruction times than would be required with a more conventional organization.

6.3.2 Reconstruction

Two major methods for image reconstruction are provided, an iterative method and a deterministic method. The primary method of choice for most clinical imaging is the iterative method, while the deterministic method, FBP, is provided for special imaging situations.

The iterative reconstruction method uses a fully three-dimensional ordinary Poisson ordered subset reconstruction [6, 7] with optional TOF and point spread function (PSF) modeling [8]. In expectation maximization (EM) reconstruction, the algorithm progresses by first simulating the collected data from a prototype image, then comparing the simulated data to the collected data, and adjusting the prototype image accordingly. The term ordinary Poisson means that the collected data are left unchanged, thus preserving the Poisson statistics of the collected events. In ordered subset EM (OS-EM), the algorithm uses a subset of the radial angles for each image update. The subset of fewer radial angles allows a faster simulation and image update, thus speeding up the algorithm.

Point spread function (PSF) modeling can be optionally enabled. The model for the point spread function is obtained by imaging a ^{22}Na point source at multiple positions across the field of view and then fitting with a Gaussian function. Details of the process are described in Panin [5]. With PSF modeling enabled, the reconstruction models the emissions from each image pixel using the fitted Gaussian. Alternately, when PSF is not enabled, the emissions are assumed to remain within the pixel. Typically, PSF modeling produces smoother images with more vivid structures. However, the slower convergence can result in Gibbs ringing at sharp edges [9].

In special imaging situations, a deterministic reconstruction may be desired. To meet this need, a TOF FBP is included. After correcting the collected data for randoms, normalization, distortions, and attenuation, the algorithm uses FORE rebinning [10] to convert the three-dimensional TOF sinogram to a two-dimensional TOF sinogram. Then two-dimensional FBP produces the final image.

6.3.3 Randoms

Randomly occurring coincidences within the on-time or prompt time window add a count rate-dependent background to the image. To correct, the reconstruction uses an estimate of the number that occurs in the delayed time window described earlier. The delayed coincidences use the same data path as the on-time coincidences. This ensures that the estimate is precise and varies only due to the Poisson random process. Since the estimate is a random process, using it directly could add additional noise to the image. To mitigate this possibility, the estimate is smoothed using a variance reduction algorithm [11]. The reconstruction algorithm then uses this improved estimate in the model of the acquired data.

6.3.4 Normalization

The circular arrangement and the modular grouping of the detectors cause different crystals to have varying sensitivity to the gamma rays. Also, more counting losses occur with higher radioactivity in the system. A normalization corrects for these differences and provides accurate quantitation at all activity levels. It is important that the dead time correction be crystal specific as individual crystals in a detector can respond differently [12]. As the normalization is recalibrated daily, each collected data set includes a specific normalization.

6.3.5 Scatter

Some of the 511 keV gamma rays resulting from the positron annihilations will interact with the attenuation media and scatter or change direction. In the process, the gamma rays also lose energy. If enough energy is lost, the lower level energy discriminator will reject the event. The accepted events will add an object-dependent background to the image, reducing contrast.

As the scattered events are indistinguishable from non-scattered events, an estimate of the scattered events must be obtained by a model [13, 14]. The physics of scattering is well known. The Single Scatter algorithm simply uses the emission image as the source of radioactivity and traces the gamma rays through the attenuation image (μ-map). At each voxel in the image, the gamma can either be scattered or not. Ultimately, the scattered events are tallied and form a scatter sinogram.

Since the initial emission image contains both scattered and non-scattered events, the initial estimate of scatter will be too large. However, this estimate can be subtracted from the initial data, and the simulation repeated until the estimated scatter is correct.

If all the activity were contained in the scanner FOV, the scatter simulation would be very precise. However, most objects are longer than the scanner axial length. Since the scanner cannot "see" activity beyond the FOV, it cannot be included in the simulation. However, by scaling the simulated scatter to match measured scatter, the algorithm refines the estimate. Using the fact that radioactivity only exists in the object being scanned, the μ-map can be segmented to distinguish between the regions where radioactivity exists and where none exists. Since the scattering process mispositions the line of response, scatter occurs in the air region. By scaling the scatter estimate to match the measured scatter in this region, the estimate can be refined.

6.3.6 Attenuation Correction

When a 511 keV gamma ray interacts with matter, one of two possibilities results. Either the gamma ray is absorbed and a photoelectron results or the gamma ray can scatter. With water (or tissue), the possibility of a photoelectric interaction is negligible. Any photon lost along the initial path will be scattered. Some of the scattered photons will exit the scanner, others will be rejected due to energy loss, and some will be accepted and contribute to the scatter described in the previous section. In any case to produce a quantitative image, the reconstruction algorithm needs a map of the probability that scattering (attenuation) can occur.

In PET/CT, the CT system provides this map. A CT image also is a map of attenuation. However, the X-ray energy of the CT is much lower than the 511 keV gamma ray. Fortunately, a simple algorithm can convert the X-ray image to a 511 keV μ-map [15]. This algorithm simply converts the CT image pixel from units of Hounsfield to 511 keV μ using a linear transformation. The CT image pixels are converted in intensity and interpolated to match the PET image grid.

6.3.7 Continuous Bed Motion

The 26 cm axial length of the detector is significantly shorter than most patients. To acquire an image of an entire patient torso, the scanner would normally acquire several images, moving the patient couch or bed for each so that the images overlap. In some cases, mismatch in the overlapped images can cause image artifacts. To simplify acquisition planning and mitigate the artifacts, Siemens Healthineers provides a continuous bed motion acquisition where the bed slowly traverses the full extent of the desired image. To accomplish this, the system forms a virtual sinogram with an axial length set at acquisition time. As the bed moves from plane to plane of the sinogram, the events are placed appropriately. Reconstruction of this data

proceeds as described above except for normalization. For the image to be correct, crystal efficiencies, dead time correction, and decay correction must be included in the normalization data [16].

6.4 Performance

The National Electrical Manufacturers Association publication NU 2-2018 "Performance Measurements of Positron Emission Tomographs" describes a unified set of measurements of physical characteristics of PET. These measurements were designed to allow comparison of PET tomographs with different designs. The following section describes the measurements and summarizes the results for the Vision 600 obtained by groups from two centers [17, 18].

6.4.1 Spatial Resolution

Spatial resolution measures the ability of the tomograph to reproduce a small point of radioactivity. NEMA NU 2-2012 describes using a source made by forming a 1 mm × 1 mm cylinder of ^{18}F in a capillary tube. The source is made by using the capillary action of the tube to acquire a small drop of liquid. If the drop is too large, then the length in the tube exceeds 1 mm. Moses [19] suggested an approximation for spatial resolution where the source size is added in quadrature to other components. For systems with larger crystals, the added length was negligible. However, for systems with smaller crystals, the added length could be significant. For this reason, the authors of NEMA NU 4-2008 [20] designed a ^{22}Na source that has an extent of 0.3 mm. This source was also suggested as an alternative to the ^{18}F source by the authors of NEMA NU 2-2018 [21].

Data from the source are collected at the center of the axial FOV and at one eighth the axial FOV from the end. For these two axial positions, data are also collected at 1, 10, and 20 cm from the center of the transverse FOV. The two axial measurements are averaged in the final report. Reconstruction for the images is FORE rebinned FBP with a ramp filter. The pixel size used is 0.825 × 0.825 × 0.823 mm. Table 6.2 summarizes resolution data collected from the two centers.

6.4.2 Sensitivity

System sensitivity measures the number of positron annihilations detected by the scanner. The measurement is performed by filling a 70-cm-long plastic tube with ^{18}F and placing it in the scanner. The tube is surrounded by five concentric metal tubes that provide material to annihilate the positrons. After each of five measurements, a tube is removed. The attenuation of the annihilation photons by the metal is found by fitting the five measurements. The result will be the number of annihilations detected if there was no attenuation. Two measurements are made, one with the tube

Table 6.2 Spatial resolution

	Center	System A [17]		System A [17]		System B [18]	
	Isotope	^{22}Na		^{18}F		^{22}Na	
	Distance (cm)	FWHM	FWTM	FWHM	FWTM	FWHM	FWTM
Radial	1	3.5	6.8	3.7	7.4	3.5	6.9
Tangential	1	3.6	6.9	3.7	7.2	3.7	6.9
Axial	1	3.5	7.1	3.8	7.6	3.6	7.2
Radial	10	4.5	8.4	4.6	8.8	4.6	8.5
Tangential	10	3.9	7.0	3.9	7.3	3.9	7.0
Axial	10	4.3	8.7	4.3	9.2	4.3	8.8
Radial	20	5.8	10.5	6.0	11.1	5.8	10.5
Tangential	20	3.5	6.4	3.6	7.0	3.5	6.4
Axial	20	4.4	9.4	4.6	10.2	4.4	9.6

Table 6.3 System sensitivity (kBq/Mbq)

Position	System A [17]	System B [18]
0	16.4	15.1
10	16.3	15.6

placed at the axis of the scanner and a second with the tube parallel to but 10 cm offset from the axis (Table 6.3).

6.4.3 True, Scatter, and Random Rates

This test assesses the ability of a tomograph to accurately measure activity given a range of activities. Since the occurrence of random coincidences follows a square relation with activity, higher activities produce more random coincidences than lower activities. Also, scatter fractions can change due to event pileup in the detectors. This test measures the true coincidence rate, the random event rate, and fraction of scatter produced by a 20-cm-diameter, 70-cm-long phantom. The activity is placed in a plastic tube parallel to the axis of the phantom but offset by 4.5 cm. The phantom is placed along the axis of the scanner.

True coincidences from positron annihilations are the signal that produces the image. Yet, because the true coincidences are limited, image noise also results. At the same time, random coincidences and scattered events contribute only to the image noise but not to the image. Noise equivalent count rate (NECR) is a figure of merit that better predicts image noise and uses all three types of events [22]. For the specified phantom, at a given activity, a higher NECR results in lower image noise.

Figure 6.3 shows a typical plot of true, random, and scatter coincidences as well as a plot of NEC computed from the three. Table 6.4 summarizes the measurements taken at both centers.

Reconstructing this data and comparing the images to the know activity gives a measure of the accuracy of the tomograph. Since all corrections are applied during reconstruction, this test also tests the integrity of the corrections. The

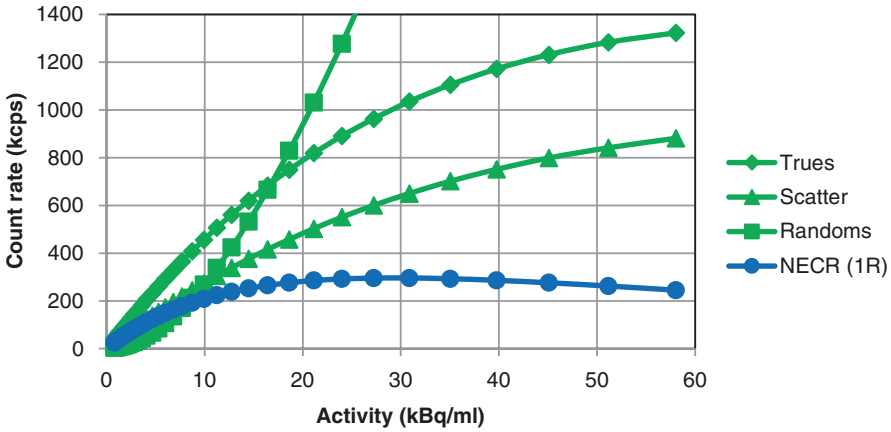

Fig. 6.3 Plot of measured true, random, and scatter coincidences with calculated NEC

Table 6.4 Summary of NECR and scatter fraction

Parameter	System A [17]	System B [18]
Peak NECR (kcps)	306	296
Activity at peak (kBq/ml)	32.6	30.9
Scatter fraction at low activity	37%	37%
Scatter fraction at peak NECR	39%	39%

mean bias measured on System A was 2.9% at peak true rate, while the mean bias on System B was around 3% at peak NECR.

Scatter fraction, the ratio of the accepted scatter to the total of true and scatter coincidences, should be a function of only the phantom makeup and the scanner energy window. However, as the detector count rate increases due to higher activity, event pileup can cause the scatter fraction to change. For this reason, the NEMA NU 2-2018 [21] requires a report on scatter fraction at both low activity and at peak NECR. Both Systems A and B [17, 18] measured 37% at low activity and 39% at peak NECR.

6.4.4 Time Resolution

Time resolution measures the scanners' ability to localize a positron annihilation along the line of response. Again, event pileup in the detector can compromise the time resolution. NEMA NU 2-2018 [21] describes a procedure for calculating the time resolution using the data collected in the test described above. Figure 6.4 shows a typical measurement of time resolution. Both Systems A and B [17, 18] measured 210 ps FWHM at low activity, and System B [18] measured 215 ps at peak NECR.

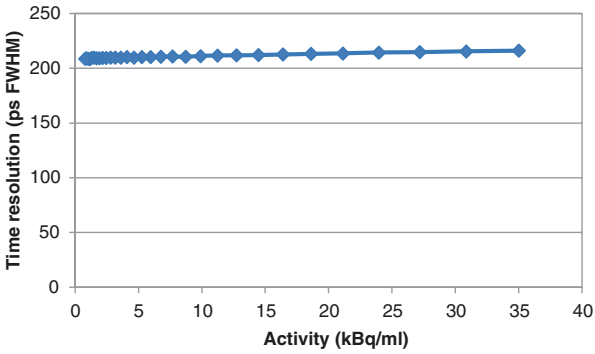

Fig. 6.4 A typical measurement of time resolution showing a slight increase up to peak NECR

Table 6.5 Results from image quality phantom test

	Contrast (%)		Background variability (%)	
Sphere size	4 to 1	8 to 1	4 to 1	8 to 1
10	93.1	86.8	6.4	6.0
13	73.5	77.2	5.0	5.0
17	79.0	85.0	4.0	3.9
22	87.0	89.8	3.1	3.3
28	86.3	87.4	2.7	3.0
37	89.4	89.6	2.2	2.2
Lung residual	3.4	3.5		

6.4.5 Image Quality

The image quality test specified in NEMA NU 2-2018 allows scanners with different designs to be compared when the imaging task is constant. The phantom consists of a 23 × 30 mm body containing six hollow spheres ranging from 10 to 37 mm internal diameter and a central cylinder insert simulating lung. According to the procedure, the spheres are filled either four or eight times the background concentration. The background concentration is specified to be 5.3 kBq/cc, while the imaging time is set by the axial bed step of the scanner. For the Biograph Vision, the imaging time is 237 seconds.

Analysis of the measurement proceeds by drawing ROIs on the spheres and comparing to ROIs drawn on the background. The report provides the contrast and background variation. The choice of image reconstruction method will affect the measurement. In the data presented below, the method was OP-OS-EM with eight iterations and five subsets and included both TOF and PSF modeling. Table 6.5 shows the results of the image quality measurement made on System A [17].

6.5 Clinical Applications

SiPM technology has revolutionized PET imaging with advanced performance characteristics described earlier in this chapter. The benefit of these performance enhancements is made readily apparent when examining how they are applied to

clinical applications and patient care. This section will specifically focus on the benefits of the SiPM technology implementation on the Biograph Vision PET/CT platform applied to clinical techniques and the potential improvements that can be seen with these technologies. The Siemens Healthineers Biograph Vision was released with acquisition and processing tools that enhances and takes full advantage of the scanner's improved performance and capabilities.

Fundamentally, each of the applications discussed for the Biograph Vision platform benefits from key technological developments in spatial resolution and sensitivity. These improvements are a product of significant improvements in detector technology, smaller crystals, and an increased axial field of view, as well as timing electronics that allow for state-of-the-art, time-of-flight (TOF) measurements. It has been shown numerous times and as far back as the 1980s that taking into account TOF results in an effective increase in signal-to-noise ratio (SNR) and, subsequently, effective sensitivity gains [23].

The uncertainty in photon position along a line of response is given by:

$$\Delta x = \frac{\Delta t \cdot c}{2}$$

where Δt is the difference in arrival times between the first and second detector and c is the speed of light. We can determine the best possible localization accuracy of a given system by using the system timing resolution as the highest achievable Δt for a given PET system.

The prior generation of Biograph systems, based on standard photomultiplier tubes, has a NEMA-tested timing resolution of 535 picoseconds (ps). For a system with a 535 ps timing resolution, the uncertainty in event positioning along any line of response is approximately 8 centimeters. Although 535 ps is state of the art for a PMT-based platform, the new SiPM Vision platform specifies a timing resolution of 214 ps and has been NEMA tested to show a timing resolution performance range of 210–215 ps which gives us an estimated uncertainty in event positioning of only 3 cm [17].

Clinically, this translates to improved image quality and contrast in regions that are larger than the minimum uncertainty along a line of response. For the PMT-based system, the use of TOF information will show the greatest impact on contrast in the body of the patient with the effective improvements increasing with larger patient size. As seen in Fig. 6.5, the differences in image contrast and event localization can be seen in the abdomen images and will be especially noticeable in the larger patients.

The reduced uncertainty in positioning on the SiPM Biograph Vision platform provides positioning accuracy that can not only noticeably improve body imaging contrast but can also provide enhanced contrast in anatomical regions on the order of the size of an adult head, which averages approximately 7 inches wide and 9 inches long. Figure 6.6 shows a reconstruction on the Vision platform with and without time of flight taken into consideration. Increased contrast is immediately noticeable over the entire body, with improved detail shown in a head and neck lesion, as well as fine details seen in the spine. Cardiac imaging may also see benefits of improved TOF measurement accuracy, as the average heart size is within the

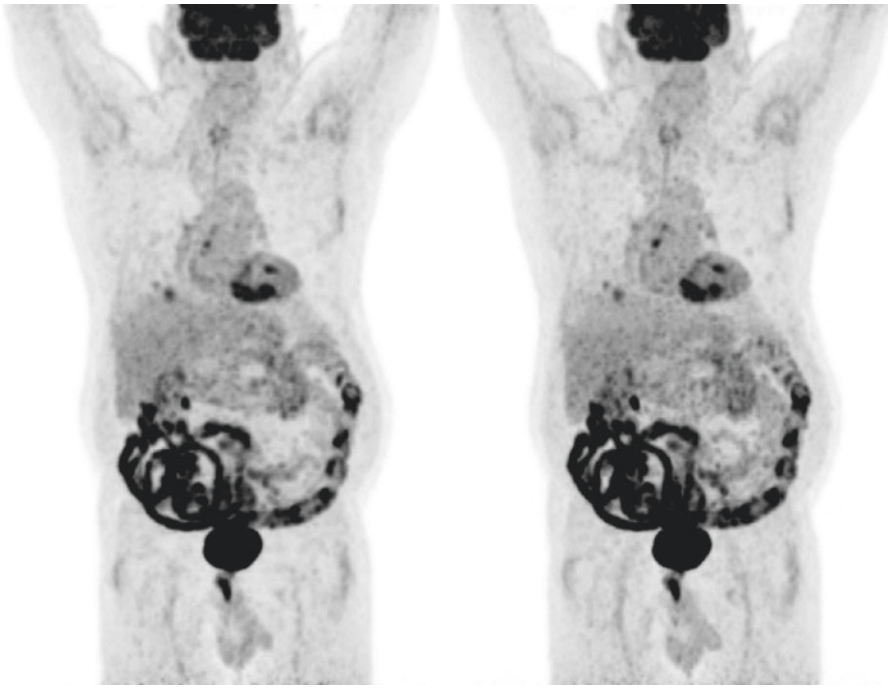

Fig. 6.5 Comparison of images without (left) and with (right) time of flight taken into account. Changes to contrast and event localization can be seen in the comparison. (Image courtesy of The University of Tennessee Medical Center)

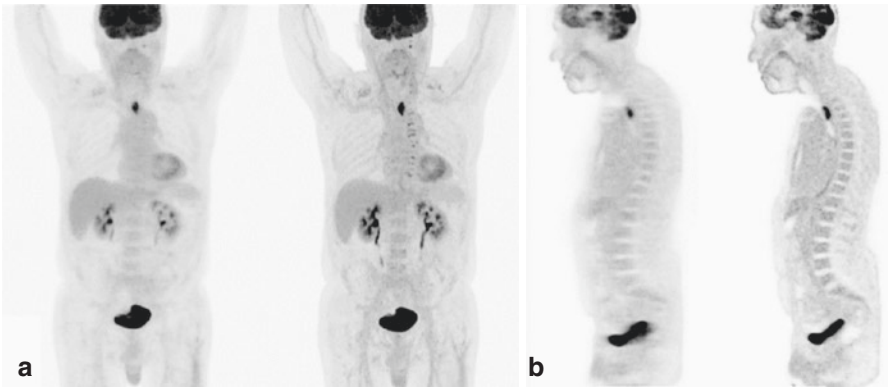

Fig. 6.6 A comparison of point spread function reconstructions on the Vision platform with and without time of flight. (**a**) Improvements in the small head and neck lesion as well as in the heart. (**b**) Improvements to the whole-body imaging with fine details in the spinal column as well as the significant contrast enhancements in the brain. (Images courtesy of Siemens Healthineers)

range of 5 inches long and 3.5 inches wide where TOF gains would serve to improve quantitative accuracy and image quality with increased contrast.

The latest generation of SiPM-based detectors provides state-of-the-art resolution with a detector array of 3.2 mm × 3.2 mm × 20 mm. NEMA testing with a Na-22 point source at 1 cm off-center has indicated a transverse resolution of 3.6 mm FWHM showing excellent high-resolution performance [2]. Higher resolution not only translates into the ability to see smaller objects in the final reconstructed images but also impacts quantitative imaging by reducing the impact of partial volume effects that can have a profound effect on regions of interest drawn on the data [24].

6.5.1 Continuous Bed Motion

Continuous bed motion (CBM) methodologies were first proposed by Dahlbom et al. in 1992 as a way to potentially improve image quality in PET imaging with the concept integrated into a clinical PET system in 2000 [25, 26]. A CBM implementation for PET/CT was presented in 2002 by Townsend et al. [26–28]. Over the next few years, technological advancements in data processing and electronics were made related to CBM [29, 30], but it would be 10 years from the initial clinical PET/CT prototype in 2002 before the first commercially available implementation would be made available on the Biograph mCT Flow platform [31–33].

Traditional step-and-shoot acquisition methods define a series of overlapping bed positions, whereby the bed moves to the bed location and acquires data for a predetermined time before moving to the next bed position. With continuous bed motion PET, the imaging table moves continuously through the PET FOV at a speed (mm/s) along an axial range selected by the technologist. This motion is similar to that of a computed tomography (CT) system but at significantly slower speeds. With this type of acquisition, each part of the patient will move through the central part of the detector ring where the imaging performance is optimum for any PET system, resulting in an improved axial sensitivity profile [34, 35]. A comparison of the standard step-and-shoot range selection (left) versus the CBM axial range selection scheme (right) is shown in Fig. 6.7.

One of the key technological achievements that makes CBM acquisition possible is appropriate data processing and corrections to accurately position events as the bed moves through the FOV [16, 29, 30]. The impact of time of flight on continuous bed motion can be appreciated with the improved accuracy of event localization under these unique acquisition conditions. The CBM acquisition mode enables the ability to adjust local axial image quality and tune the acquisition to a specific application and patient needs.

On the Biograph Vision platform, users can select up to four ranges along the axial extent of the acquisition, for which the bed speed can be modified within each range to either acquire more slowly or more quickly over a defined region

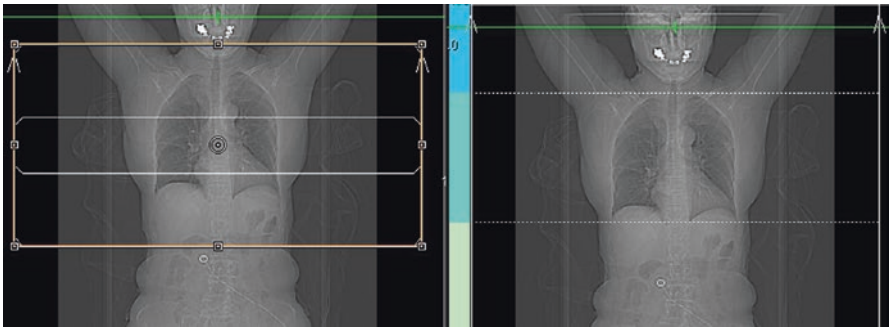

Fig. 6.7 Comparison of traditional step-and-shoot range selection (left) versus continuous bed motion range selection (right). The continuous bed motion image shows the clean layout of selecting multiple speed ranges across the axial extent to be imaged. (Images courtesy of The University of Tennessee Medical Center)

depending on the specific needs of the patient. A key clinical example of using these defined axial ranges is for cardiac or respiratory gating where you may want to slow down over the regions of the lung or heart to collect more counts to make the gated image less noisy or to be able to reconstruct a higher resolution image matrix [36]. The use of SiPM technology with CBM technology enables patient-specific protocol selection that maximizes throughput and reduces patient radiation doses.

The additional TOF effective sensitivity gains offered by the Biograph Vision SiPM system translate into three potential clinical options related to routine clinical imaging. The first is to reduce the injected dose to the patient and keeping imaging protocols the same, thereby reducing overall patient radiation exposure. The second is to keep the injected dose the same but reduce the scan time to improve patient workflow and efficiency. The third and final option keeps dose and scan times the same but results in overall improved image quality because of a significant increase in counts.

The resolution improvements are also apparent in standard CBM imaging on the Vision platform and are maximized, if the sensitivity gains are used to acquire more data per scan. The Vision platform enables routine use of significantly higher image matrix sizes of 440 × 440 compared to the standard PET image sizes of 200 × 200 or 256 × 256. The improved sensitivity and resolution, combined with CBM, enable robust multirange protocols to collect data that is adequate for the reconstruction of both standard and high-resolution data in a single data acquisition pass.

6.5.2 Respiratory and Cardiac Gating

With respiratory and cardiac gating, the imaging data collected is synchronized to a waveform collected from respiratory monitoring devices or those monitoring cardiac echocardiogram (ECG) signals. These signals provide information about the physiological pattern that is then used to either reconstruct phase-based four-dimensional

(4D) gated images that are used to show the motion of the physiology or as amplitude-based gated images that freeze the motion at a specific point in time to create a motion-free static image [37]. With both gating methods, sensitivity is critical to getting the counts needed to compensate for either count losses, as happens with amplitude-based methods, or splitting counts across time bins as occurs with standard phase-based gating. With these standard methods, it is almost always necessary to increase scan time (step-and-shoot) or decrease bed speed (CBM) in order to compensate for the count losses that occur; however, with the improved sensitivity of the Siemens Healthineers SiPM platform, these images can be acquired in a shorter time and with improved image quality.

New to the Vision platform is a hybrid gating technique that uses amplitude-based gating with an optical flow algorithm to reconstruct images using 100% of the collected counts [38]. This new algorithm first generates an amplitude-gated image to use as a reference image. The optical flow algorithm then deblurs the remaining static data until it matches the reference image. This technique enables reconstruction of motion-frozen images without the typical count losses of approximately 30% that are experienced with traditional amplitude-based gating methods. Figure 6.8 shows a comparison of amplitude-based gating vs. the new optical flow

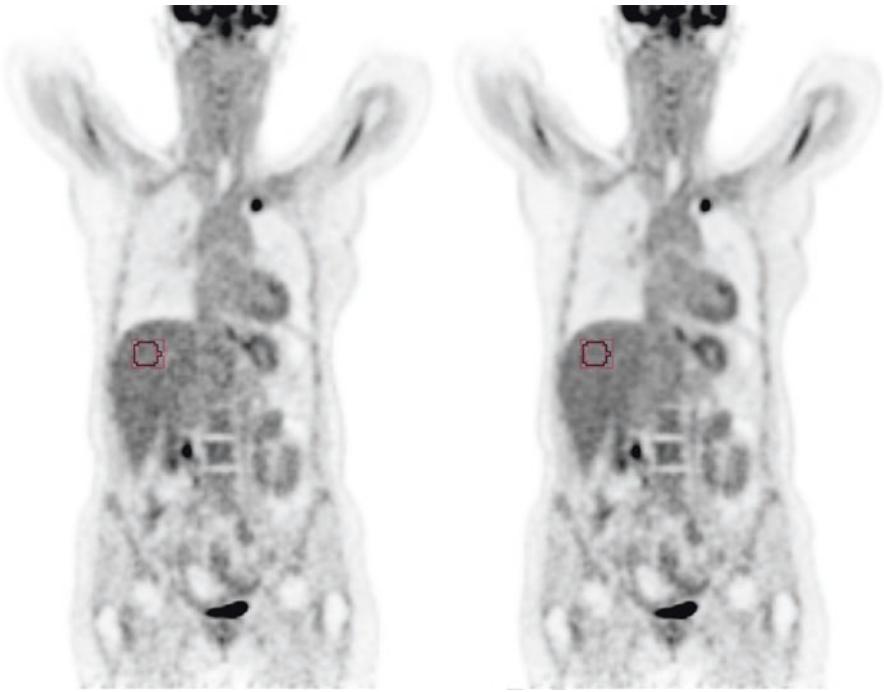

Fig. 6.8 Comparison of standard amplitude-based gating (left) versus OncoFreeze (right). The ROI drawn in the liver showed a decrease in standard deviation to mean of approximately 33% using OncoFreeze since all of the counts acquired during the study could be used in the reconstruction. (Images courtesy of The University of Tennessee Medical Center)

hybrid algorithm, called OncoFreeze with the liver ROI showing a reduction of approximately 33% in standard deviation to mean in this example with OncoFreeze vs. traditional amplitude-based gating.

The use of amplitude-based gating techniques improves quantitative accuracy of regions of interest by limiting the smearing of the counts from a given lesion along the direction of motion. When respiratory or cardiac motion effects are present, the resulting smearing of the counts will reduce the values measured by a region of interest, with maximum voxel values typically affected the most [37]. The improved resolution on the Vision platform further increases quantitative accuracy by reducing the impact of partial volume effects on small lesion measurements and combined with the improved sensitivity opens up further use of these techniques to provide better matching of gated PET and CT data as well as more routine use of motion correction techniques in radioisotope therapy monitoring [39, 40].

6.5.3 Parametric Imaging

From the inception of PET imaging, the potential for robust quantitative analysis was recognized. Those that developed the technology saw the potential for PET to enable true quantitative assessment of radiotracer metabolism within a patient using kinetic modeling techniques [41]. The use of kinetic modeling techniques enables the possibility of quantifying true metabolic utilization rates [42]. In the case of 18F-fluorodeoxyglucose (18F-FDG) imaging, quantification using parametric imaging can provide pixel values that correlate with true metabolic rates of glucose utilization observed during the tracer uptake period.

The gold standard for current semiquantitative PET is the standard uptake value (SUV), which normalizes the activity concentration acquired by the scanner by the specific patient's weight and injected dose given by:

$$\mathrm{SUV} = \frac{\text{Activity concentration}\left(\mathrm{Bq/ml}\right)}{\text{Injected dose}\left(\mathrm{Bq}\right)} \times \text{Patient weight}\left(\mathrm{g}\right)$$

This provides a useful semiquantitative value that enables assessment and monitoring of disease but is limited in its ability for delineation of disease and global comparison across patient populations [43]. The use of kinetic modeling techniques with parametric imaging enables the possibility of quantifying true metabolic utilization rates.

With traditional step-and-shoot PET systems, dynamic studies were mostly limited to single-bed position scans. Data are collected dynamically over the region of interest from the time of injection until 1–2 hours postinjection. The data are then processed dynamically for the purposes of generating time activity curves to use in subsequent modeling. Although powerful, single-bed position dynamic imaging is limited only to analysis of that specific region and does not provide capabilities for whole-body parametric analysis.

The use of continuous bed motion technology enables the ability to robustly perform whole-body parametric imaging [44, 45]. This is done by performing multiple bed passes over the patient during the course of the uptake period. To acquire input function information, models can be used, or a single-bed dynamic acquisition over the heart can be used to generate the input function TAC, just as in standard step-and-shoot dynamic scans. For our CBM parametric studies, we perform a dynamic, single-bed acquisition over the heart during the injection that lasts approximately 6 minutes, followed by 11 passes that decrease in bed speed over the course of the remaining 44 minutes of uptake. Figure 6.9 shows our resulting input function TACs and dynamic images acquired on our PMT-based system.

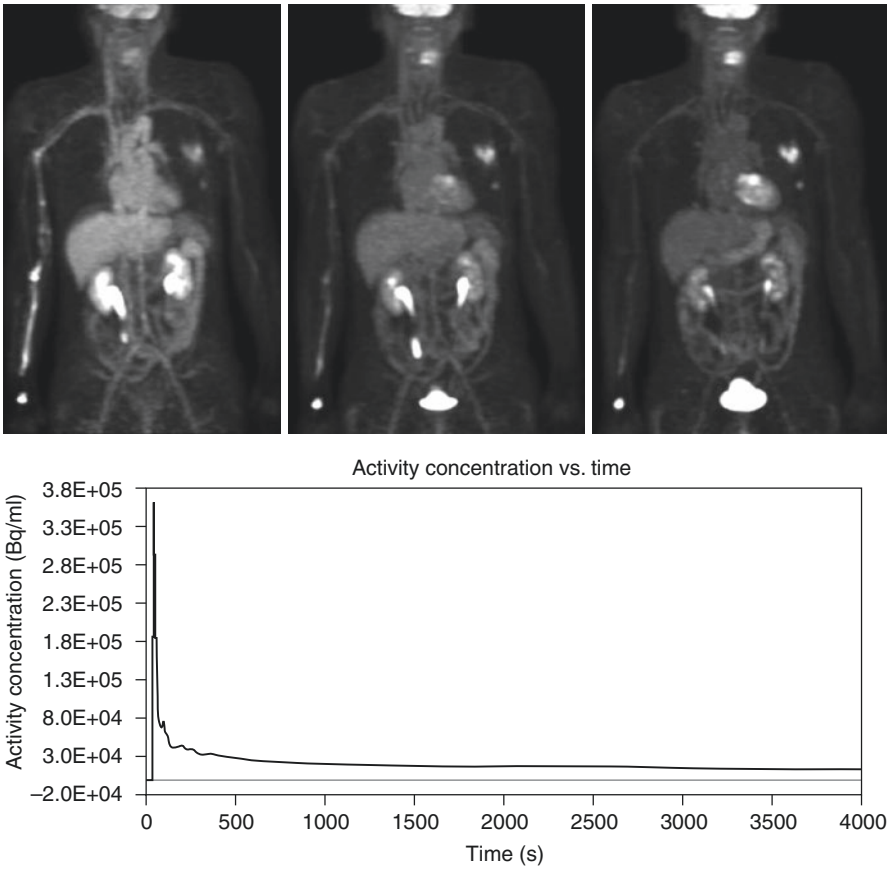

Fig. 6.9 Dynamic reconstructions at different time points during a multi-pass continuous bed motion parametric data acquisition (top). The lower image shows the automatically generated, image-derived input function time activity curve created by the automated aorta segmentation software built into the Siemens parametric analysis package. (Images courtesy of The University of Tennessee Medical Center)

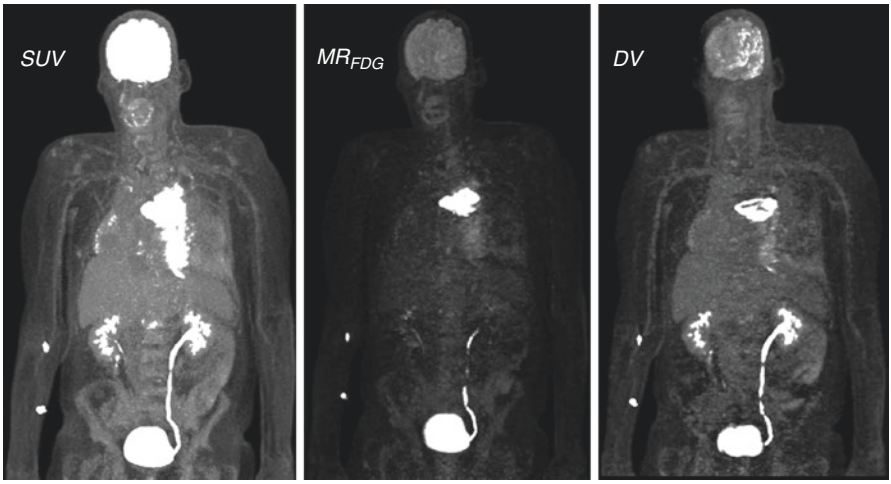

Fig. 6.10 Left standard SUV image. Middle metabolic uptake rate image. Right blood volume image

Resolution also plays a similar role as described in other applications above, as partial volume effects also are critical concerns when performing dynamic PET data analysis. A necessary element required for any kinetic modeling is an arterial input function, which aside from actually drawing arterial blood samples is commonly derived from the PET data by drawing a region of interest in the aorta, left ventricle, or other area that can serve as a valid representation of the true arterial input function [46]. These small regions of interest typically are impacted by partial volume effects requiring appropriate corrections to not inadvertently bias the final modeling results [47].

The difficulty with parametric studies, aside from the long scan times, has long been the need for external data processing to generate the appropriate input function TACs and having appropriate staff with modeling expertise in order to yield the final quantitative results desired. These have long been relegated to only a small number of institutions with specific research interests in the area of parametric PET imaging. Recently, Siemens Healthineers has released a new parametric imaging suite that enables automation of a number of these tasks, including a built-in Patlak modeling interface that generates parametric PET images (Fig. 6.10) with voxels that represent metabolic rates of glucose utilization and distribution volume information, in addition to standard SUV images.

6.6 Conclusion

The Biograph Vision SiPM PET/CT platform provides state-of-the-art imaging, characterized by its state-of-the-art 214 ps timing resolution that leads to the most

accurate event positioning in the industry. The TOF gains associated with this technological development enables improvements in a number of key clinical applications where sensitivity impacts acquisition modes and image quality, such as continuous bed motion imaging, physiological gating, and parametric imaging. Most exciting with this technology is the potential to propel quantitative PET to a new level, with robust dynamic image acquisition and parametric image processing that will certainly lead to enhanced image analysis and new clinical tools for the diagnosis and monitoring of disease.

References

1. Melcher CL, Schweitzer JS. Cerium-doped lutetium oxyorthosilicate: a fast, efficient new scintillator. IEEE Trans Nucl Sci. 1992;NS-39(4):502–5.
2. Cho S, Mintzer R. Silicon-photomultiplier TOF-PET Detector IEEE NSS-MIC, Atlanta M-07-1.
3. Vandenberghe S, et al. Fast reconstruction of 3D time-of-flight PET data by axial rebinning and transverse mashing. Phys Med Biol. 2006;51:1603–21.
4. Panin VY, Defrise M, Casey ME. Restoration of fine azimuthal sampling of measured TOF projection data. In: 2010 IEEE nuclear science symposium conference record (NSS/MIC). IEEE; 2010.
5. Panin VY, Aykac M, Hong I. TOF data compression on high time resolution clinical scanner. In: 2018 IEEE nuclear science symposium, Sydney.
6. Comtat C, et al. OS-EM-3-D reconstruction strategies for the ECAT HRRT. In: 2004 IEEE NSS MIC conf. rec., vol. 6. Rome; Oct. 2004. p. 3492–96.
7. Hudson HM, Larkin RS. Accelerated image reconstruction using ordered subsets of projection data. IEEE Trans Med Imaging. 1994;13(4):601–9.
8. Panin VY, et al. Fully 3-D PET reconstruction with system matrix derived from point source measurements. IEEE Trans Med Imaging. 2006;25(7):907–21.
9. Rahmim A, Qi J, Sossi V. Resolution modeling in PET imaging: theory, practice, benefits, and pitfalls. Med Phys. 2013;40(6):064301.
10. Defrise M, Casey ME, Michel C, Conti M. Fourier rebinning of time-of-flight PET data. Phys Med Biol. 2005;50(12):2749–63.
11. Panin VY. Monotonic iterative algorithms for crystal efficiencies estimation from normalization data and single rates estimation from compressed random coincidence data. In: 2013 nuclear science symposium, Seoul.
12. Aykac M, Panin V, Bal H. Crystal-based deadtime correction for Siemens next generation SiPM based PET/CT scanner. In: 2017 IEEE nuclear science symposium, Atlanta.
13. Watson CC. New, faster, image-based scatter correction for 3-D PET. IEEE Trans Nucl Sci. 2000;47(1):1587–94.
14. Watson CC. Extension of single scatter simulation to scatter correction of time-of-flight PET. IEEE Trans Nucl Sci. 2007;54:1679–86.
15. Carney JP, Townsend DW, Rappoport V, Bendriem B. Method for transforming CT images for attenuation correction in PET/CT imaging. Med Phys. 2006;33(4):976–83.
16. Panin VY, Smith AM, Hu J, Kehren F, Casey ME. Continuous bed motion on clinical scanner: design, data correction, and reconstruction. Phys Med Biol. 2014;59:6153–74.
17. van Sluis J, de Jong J, Schaar J, Noordzij W, van Snick P, Derckx R, Borra R, Willemsen A, Boellaard R. Performance characteristics of the digital Biograph Vision PET/CT system. J Nucl Med. 2019;60:1031–6.
18. Reddin J, Scheuermann J, Bharkhada D, Smith A, Casey M, Conti M, Karp J. Performance evaluation of the SiPM based Siemens Biograph Vision PET/CT System. In: 2018 IEEE nuclear science symposium, Sydney.

19. Moses WW. Fundamental limits of spatial resolution in PET. Nucl Instrum Methods Phys Res A. 2011;648(Supplement 1):S236–40.
20. NEMA Standards Publication NU 2-2008. Performance measurements of small animal positron emission tomographs. Rosslyn: National Electrical Manufacturers Association; 2008.
21. NEMA Standards Publication NU 2-2018. Performance measurements of positron emission tomographs (PET). Rosslyn: National Electrical Manufacturers Association; 2018.
22. Strother SC, Casey ME, Hoffman EJ. Measuring PET scanner sensitivity: relating countrates to image signal-to-noise ratios using noise equivalent counts. IEEE Trans Nucl Sci. 1990;37(2):783–8.
23. Budinger TF. Time-of-flight positron emission tomography: status relative to conventional PET. J Nucl Med. 1983;24(1):73–8.
24. Soret M, Bacharach SL, Buvat I. Partial-volume effect in PET tumor imaging. J Nucl Med. 2007;48(6):932–45.
25. Dahlbom M, et al. Methods for improving image quality in whole body PET scanning. IEEE Trans Nucl Sci. 1992;39(4):1079–83.
26. Dahlbom M, Reed J, Young J. Implementation of true continuous 2D/3D whole body PET scanning. In: IEEE nuclear science symposium conference record. Lyon; 2000.
27. Brasse D, et al. Continuous bed motion acquisition on a whole body combined PET/CT system. In: 2002 IEEE nuclear science symposium conference record; 2002.
28. Townsend DW, et al. Continuous bed motion acquisition for an LSO PET/CT scanner. In: IEEE nuclear science symposium. Rome; 2004.
29. Newport DF, et al. Continuous tomography bed motion data processing apparatus and method. Google Patents; 2005.
30. Burbar Z, et al. Continuous bed motion data processing for a resolution LSO PET/CT scanner. In: 2005 IEEE nuclear science symposium conference record; 2005.
31. Schatka I, et al. A randomized, double-blind, crossover comparison of novel continuous bed motion versus traditional bed position whole-body PET/CT imaging. Eur J Nucl Med Mol Imaging. 2016;43(4):711–7.
32. Rausch I, et al. Performance evaluation of the Biograph mCT Flow PET/CT system according to the NEMA NU2-2012 standard. EJNMMI Phy. 2015;2(1):26.
33. Osborne DR, et al. Quantitative and qualitative comparison of continuous bed motion and traditional step and shoot PET/CT. Am J Nucl Med Mol Imaging. 2015;5(1):56–64.
34. Saha GB. Basics of PET imaging : physics, chemistry, and regulations. 2nd ed. New York: Springer; 2010. xiv, 241 p.
35. Weissleder R, et al. Molecular imaging: principles and practice. Shelton: PMPH USA; 2010.
36. Acuff SN, Osborne D. Clinical workflow considerations for implementation of continuous-bed-motion PET/CT. J Nucl Med Technol. 2016;44(2):55–8.
37. van Elmpt W, et al. Optimal gating compared to 3D and 4D PET reconstruction for characterization of lung tumours. Eur J Nucl Med Mol Imaging. 2011;38(5):843–55.
38. Hong I, et al. The strategy of elastic motion corrections. In: IEEE nuclear science symposium conference record; 2013.
39. van der Vos CS, et al. Improving the spatial alignment in PET/CT using amplitude-based respiration-gated PET and respiration-triggered CT. J Nucl Med. 2015;56(12):1817–22.
40. Osborne DR, et al. 90Y liver radioembolization imaging using amplitude-based gated PET/CT. Clin Nucl Med. 2017;42(5):373–4.
41. Phelps ME, et al. Tomographic measurement of local cerebral glucose metabolic rate in humans with (F-18)2-fluoro-2-deoxy-D-glucose: validation of method. Ann Neurol. 1979;6(5):371–88.
42. Morris ED, Endres CJ, Schmidt KC, Christian BT, Muzic RF Jr, Fisher RE, Kinetic Modeling in Positron Emission Tomography, in Emission Tomography: The Fundimentals of PET and SPECT. 2004;499–540.
43. Kinahan PE, Fletcher JW. Positron emission tomography-computed tomography standardized uptake values in clinical practice and assessing response to therapy. Semin Ultrasound CT MR. 2010;31(6):496–505.

44. Osborne DR, Acuff S. Whole-body dynamic imaging with continuous bed motion PET/CT. Nucl Med Commun. 2016;37(4):428.
45. Karakatsanis NA, Garibotto V, Rager O and Zaidi H, Continuous bed motion Vs. step-and-shoot acquisition on clinical whole-body dynamic and parametric PET imaging. In: 2015 IEEE nuclear science symposium and medical imaging conference (NSS/MIC). San Diego; CA, 2015, pp. 1–6.
46. Chen K, et al. Noninvasive quantification of the cerebral metabolic rate for glucose using positron emission tomography, 18F-fluoro-2-deoxyglucose, the Patlak method, and an image-derived input function. J Cereb Blood Flow Metab. 1998;18(7):716–23.
47. Zanotti-Fregonara P, et al. Image-derived input function for brain PET studies: many challenges and few opportunities. J Cereb Blood Flow Metab. 2011;31(10):1986–98.

Part III

Future Prospective of PET/CT Instrumentation and Technology

Future Prospects of PET Instrumentation and Technology

7

Suleman Surti and Joel S. Karp

7.1 Introduction

Recently, most major vendors have introduced new digital PET/CT systems based on detectors with silicon photomultiplier (SiPM) technology. Compactness and flexibility of SiPMs in coupling to scintillator arrays has led to improvements in both spatial and timing resolution [1] of the latest PET systems. In addition to improvements in detector performance, the digital PET/CT systems retain also the significant developments made in PET imaging over the last two decades, including CT-based attenuation correction, lutetium-based scintillators with high sensitivity and fast timing characteristics, and fully 3D iterative time-of-flight (TOF) informed reconstruction leading to quantitative images with high signal-to-noise ratio. Geared toward oncologic FDG studies, these digital PET/CT systems can perform whole-body surveys in 10–15 minutes with excellent image quality for heavy as well as light patients due to the improved TOF resolution.

However, there is still a need for higher sensitivity for improved performance where the injected dose and scan time are limited and especially for dynamic imaging where short time frames are required to capture the fast kinetics, but the statistical uncertainties of the data can lead to errors in the biologic parameter estimation. The axial length of modern commercial PET scanners ranges between 15 and 26 cm leading to a sensitivity of 0.6–2% (or 6–20 kcps/MBq), as specified by the 70-cm-long NEMA line source measurement. Increasing the axial field of view (AFOV) is a logical step to improved sensitivity. Not only would this benefit FDG studies but also broaden the application of PET to radiolabeled compounds with isotopes that have long half-lives, which limit the dose, and low positron fraction, which reduces the sensitivity of detection. In addition, the axial length of commercial PET scanners limits our ability to observe temporal changes in the tracer kinetics to a single

S. Surti (✉) · J. S. Karp
University of Pennsylvania, Philadelphia, PA, USA
e-mail: surti@pennmedicine.upenn.edu; joelkarp@pennmedicine.upenn.edu

J. Zhang, M. V. Knopp (eds.), *Advances in PET*,
https://doi.org/10.1007/978-3-030-43040-5_7

organ, which has been shown to be important in monitoring the progression of disease, whereas a longer AFOV system would allow dynamic imaging to study disease that affects multiple organ systems.

7.2 Design Considerations for Long AFOV PET Systems

A major drawback of early PET scanners with interplane septa, known as 2D imaging, was the low system sensitivity. The advent of fully 3D PET data acquisition methods (without septa) [2], especially after the introduction of Lu-based scintillators [3], represented a big leap in the system sensitivity (up to a factor of five times gain) for similar scanner geometry. Even with this gain, PET scanners were not efficiently detecting all the emitted annihilation events with only a modest axial field of view. This can be explained by considering the relatively low probability of detection or intrinsic sensitivity for a point source in air placed at the center of the scanner. For example, a scanner with an axial FOV of 16 cm and detector thickness of 20 mm has an intrinsic point sensitivity of 5%, which translates to a (NEMA) line source sensitivity of 5.7%. Figure 7.1 shows the point source in air sensitivity that is calculated as a function of the detector thickness for varying scanner axial length (AFOV). Since using greater than 3-cm-thick scintillation crystals shows diminishing gain in

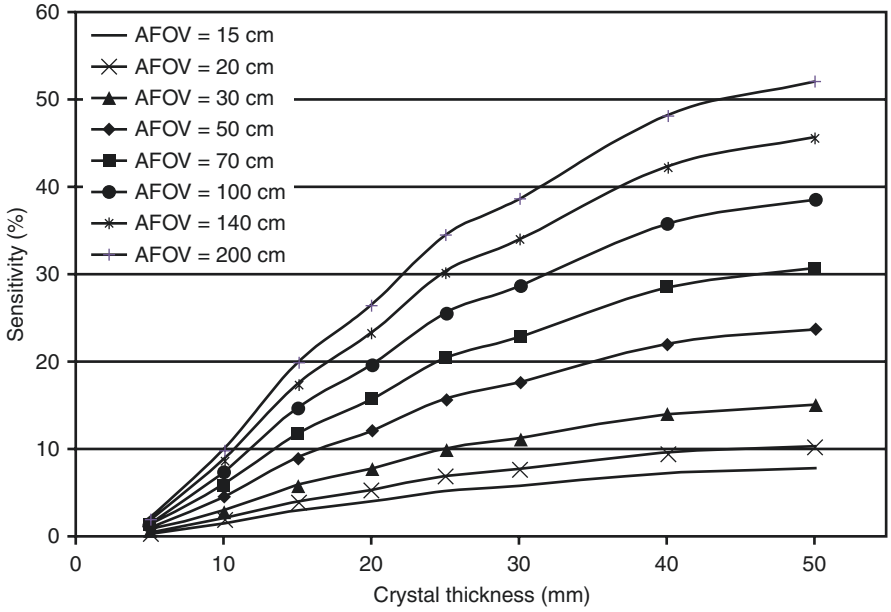

Fig. 7.1 Plot of calculated point source sensitivity versus crystal thickness for varying scanner axial length or axial field of view (AFOV). The scanner diameter was fixed at 85 cm, and LSO was used as the scintillator material. Calculations were performed for a point source in air placed at the center of the scanner

sensitivity, a better design strategy to increase the system sensitivity is to increase the scanner axial length. For a fixed crystal volume, one can generally achieve higher system sensitivity by increasing the scanner axial length instead of crystal thickness [4]. Also note that thicker crystals may lead to degraded spatial resolution depending on the detector design. As early as the 1990s, commercial whole-body PET scanners with 25-cm axial length were available, albeit with a non-Lu-based scintillator [5, 6]. Currently, at least four commercial manufacturers offer whole-body PET scanners with an axial length in the range of 20–30 cm: Siemens with the Biograph mCT (21.6 cm) and Biograph Vision (26.3 cm), GE with the Discovery MI (20 cm and 25 cm), United Imaging with the uMI 550 (24 cm) and uMI 780 (30 cm), and Canon (formerly Toshiba) with the Celestion (19.6 cm) and Cartesion Prime (25 cm). For ^{18}F-FDG oncology imaging where the uptake is assumed to be at steady state at 1 hour after injection, a clinical scanner with 20–30-cm AFOV is adequate to achieve a whole-body survey in 10 minutes with bed translation.

Figure 7.2 shows simulation results for the percentage of annihilation events reaching the detector surface as a function of scanner AFOV for varying imaging setups: (A) point source in air placed at the center of the scanner; (B) point source placed in 2-m-long water-filled, cylindrical phantoms of varying diameters; and (C) uniformly distributed source in 200-cm-long water-filled, cylindrical phantoms of varying diameters. A 20-cm-diameter phantom emulates a patient with low body-mass index (BMI), whereas a 40-cm-diameter phantom emulates a patient with high BMI.

Setup A represents an idealized situation for a single organ imaging without attenuation, while setup B realistically models attenuation that will be present in clinical

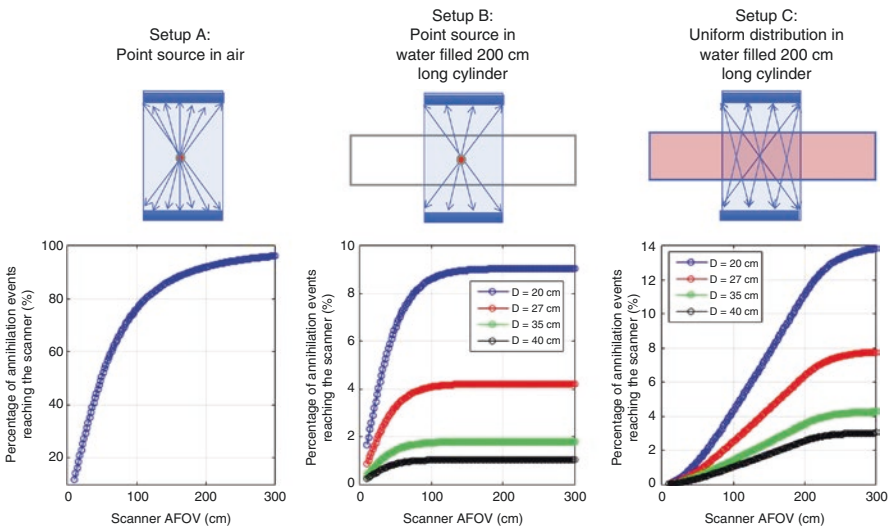

Fig. 7.2 Percentage of annihilation events reaching the scanner for three different setups calculated as a function of scanner AFOV. Results are shown for cylindrical phantoms with four different diameters

Table 7.1 Relative sensitivity with selected scanner axial field of view (AFOV) calculated for different source distributions

Scanner axial field of view (cm)	20	70	100	140	200
Point source in air placed at the center of AFOV	1	2.8	3.3	3.7	4.0
Point source placed at the center of AFOV in a 20-cm-diameter phantom	1	2.4	2.7	2.8	2.8
Uniform source distribution in a 20-cm-diameter phantom	1	10	18	29	46
Uniform source distribution in a 35-cm-diameter phantom	1	14	24	38	58

The phantoms were 200-cm-long cylinders

studies. In this imaging setup, the gain in sensitivity is not significant for scanner longer than 100 cm. Setup C represents the scenario of total-body imaging with the activity distributed throughout the FOV together with attenuation where we see continued gain in scanner as long as 200 cm. Table 7.1 summarizes the expected relative gains in sensitivity for these imaging scenarios for a few representative scanner lengths.

Hence, while extending the axial FOV of a PET system is largely an engineering task, there are some important design choices to be made: relative importance of sensitivity vs. axial coverage and whether the goal is a reduction in scan time or dose or an improvement in image quality. These design goals will vary depending on the task, and so a scalable design that allows for building systems with different axial FOV will provide maximum flexibility. Commercially, there are some systems available today, such as the GE Discovery MI, that provide such an option, but they are restricted to a modest range of 15–25 cm. With an increased number of detector and electronics channels necessary for designing a long axial FOV system, the reliability will be at premium. Finally, system software and hardware will have to handle much larger data sets with billions of lines of response, thereby requiring faster processing and larger data storage. Fortunately, modern computing processing hardware can meet the increased needs of TB-PET.

7.2.1 Development of TB-PET Scanners

The idea of improving modern PET system sensitivity by significantly increasing the axial length (beyond 30 cm) has been investigated quite extensively in recent years via Monte Carlo simulations [4, 7–12]. At least two prototype scanners were also built in the past with >50-cm axial length: one using BGO crystals and an axial length of 68.5 cm [13] and the other using LSO crystals and an axial length of 53 cm [14]. However, these systems did not have the advanced technology available in modern systems and did not transition to clinical use. In 2015, the NIH-funded EXPLORER consortium was formed that has resulted in two long axial FOV PET, both of which have recently demonstrated human imaging: the uEXPLORER scanner developed by the United Imaging Healthcare (Shanghai, China) in collaboration with the UC Davis team and the PennPET Explorer scanner developed at the University of Pennsylvania in collaboration with KAGE Medical (Wayne, PA) and

Philips Healthcare (Cleveland, Ohio). The uEXPLORER scanner is composed of eight detector rings for a 195-cm total axial FOV and has a reported spatial resolution of 2.9 mm and TOF resolution of 420 ps [15]. The PennPET scanner is based on a scalable design and was initially tested in a prototype configuration of three rings with gaps between rings with an overall axial FOV of 64 cm [16]. The scanner has a spatial resolution of 4 mm and TOF resolution of 250 ps. The PennPET Explorer is being expanded to six rings that will enable an axial FOV of 140 cm for a wider variety of TB-PET imaging.

7.2.2 First Human Studies: Benefits for Clinical Imaging and Therapy

Initial human ^{18}F-FDG studies on both these devices have demonstrated many of the fundamental benefits that were expected during their development [15, 16]. Superior image quality with fine structural details is visible in these studies when compared to images from state-of-the-art clinical scanners, indicating potential to better guide clinical treatment. Subsampling of these patient data set studies also demonstrates the ability to produce diagnostic quality images with either very short scan durations (1–2 minutes) or with dramatically reduced injected radiotracer activity. Such short scan durations can dramatically improve clinical throughput – though significant infrastructure and workflow changes will be needed to make it effective. Decreased scan times may also obviate the need for sedation in pediatric patients, decreasing the cost and risk of such procedures. With sub-minute imaging, the ability to perform breath-hold PET will also open up, benefitting characterization of small pulmonary nodules where partial volume effects dominate. Reduced injected radiotracer activity leads to a reduction in radiation dose opening up areas such as serial imaging of patients and pediatric patients, as well as new indications for PET/CT imaging, particularly in benign diseases.

Increased sensitivity of TB-PET allowing high-quality images at very low activity levels also opens up areas such as delayed ^{18}F-FDG imaging, demonstrated out to 10 hours on the uEXPLORER [15] and to 23 hours on the PennPET Explorer [17], where different uptake kinetics between malignant and normal tissues could be utilized for improved detection of the disease. Imaging such low levels of ^{18}F-FDG after 12 half-lives also indicates that TB-PET could be utilized to image radiotracers with a low-yield positron-emitting isotope such as ^{124}I (23% positron abundance and a 4.2-day half-life) and ^{90}Y (0.0032% positron abundance and a 64-hour half-life), both of which have theranostic applications. Imaging of ^{124}I in patients with thyroid cancer may allow lesion dosimetry where a dose to a tumor is prescribed rather than simply selecting a safe whole-body dose based on current dosimetry protocols. Imaging ^{90}Y after targeted radioembolization with ^{90}Y microspheres could enable dosimetry-based guidance of therapy. With marked therapeutic radiopharmaceutical growth, the imaging capabilities of TB-PET could guide development of targeted agents.

7.2.3 First Human Studies: Benefits for Research

The significantly higher sensitivity of TB-PET can also be leveraged for research applications, with the clinical applications described above easily adapted in research applications such as brain imaging for neurologic research or imaging targets with low density using PET isotopes with low positron yield and/or long half-lives. As an example, cell-tracking studies of immunotherapy performed over several days using ^{89}Zr or ^{64}Cu could allow in vivo evaluation of these relatively slow biologic processes.

Simultaneous imaging of major organs in the body will enable whole-body dosimetry studies and provide data for any refinements needed in the kinetic modeling techniques. As an example, two research patients injected with experimental radiotracers have been scanned on the PennPET Explorer, and dynamic images demonstrate the expected emptying of radiotracer from the gall bladder [17]. The presence of the heart in the same dynamic images provides an adequate input function for kinetic modeling, of particular importance for brain imaging where current modern scanners must rely on small neck vessels for image-derived input functions. Combined with the fine temporal sampling, relatively noise-free time-activity curves of both input functions and organs were generated. Improvements in kinetic analysis from TB-PET may advance our understanding of radiotracer uptake and facilitate biologic insights, particularly when combined with delayed imaging.

Simultaneous imaging of multiple organs will also enable new approaches for studying the physiologic or pathophysiologic interactions between organs, including the brain and spinal cord, and the heart and brain. It is anticipated that TB-PET, made possible by scanners with axial coverage of at least the major organs (head to pelvis, or about 1 m), will help elucidate complex interactions between these seemingly disparate organs. Further discussion about these applications can be found in [18, 19].

7.2.4 Alternative Approaches for TB-PET

Currently, in addition to the two systems developed within the EXPLORER consortium, there are several ongoing or proposed efforts to develop cost-effective long axial FOV systems. However, these systems will be based on alternative technology in contrast to the Explorer project that uses existing technology adapted from state-of-the-art commercial PET/CT. One proposal is to use an inexpensive scintillator in standard long AFOV geometry. A disadvantage of this design when it was proposed was the lack of TOF imaging capability due to the slow luminescence process in BGO [20]. However, recent work has shown evidence that TOF imaging is possible with BGO by detecting the fast Cherenkov photons that are emitted by the electrons created upon the absorption of the 511-keV annihilation photons in the BGO crystal [21–23]. While the timing resolution at full-width at half-maximum (fwhm) level is comparable to LSO, the low probability for detecting the Cherenkov photons leads

to long tail in the timing spectrum, indicating that a small percentage of detected coincidence events will actually achieve this TOF performance. Another proposal is to use long plastic tube detectors along the axial direction [24]. The TOF information along the ends of the plastic detector not only provides the axial position of an event within the detector, but together with another coincident detector, it also provides the TOF information along the line of response as needed for TOF PET. While plastic is very inexpensive and provides a fast timing signal for TOF, a significant disadvantage of this system is the low detection efficiency of plastic for 511-keV photons, leading to the need for a thick or multilayer detector to achieve reasonable system sensitivity.

Alternatively, modern PET/CT detectors (LSO/LYSO scintillator + SiPM) can be used to develop "inexpensive" long AFOV systems by reducing the total amount of detector that is used. As shown previously [4], designs using a fixed crystal volume as that used in current commercial PET systems but using thinner crystals (<20 mm thick) and extending the scanner AFOV can achieve similar or slightly higher system sensitivity. For instance, a commercial scanner using 20-mm-thick LSO/LYSO and having a 25-cm axial FOV could be extended to a 50-cm-long systems while reducing the crystal thickness to 10 mm. Along similar lines, there have been several proposals for using LSO/LYSO-based detectors in a sparse arrangement (gaps, axially and/or transaxially) [25–30], thereby reducing the detector cost while achieving longer axial FOV coverage. The many lines of response and redundancy of information in fully 3D data allow one to reconstruct artifact-free images from such arrangements. The idea of using gaps between detector rings was tested in the prototype configuration of the PennPET Explorer [16] with gaps between the rings corresponding to a data loss of 30 percent of each ring. These studies demonstrated that high-quality, artifact-free images can be generated with such data loss. While the sensitivity of such systems (thin crystals or sparse detector arrangement) will be reduced, they will provide the ability to perform dynamic whole-body imaging, a key to TB-PET.

7.3 Conclusion

Early TB-PET studies have already demonstrated the advantages in both clinical and research applications. In clinical settings, a long axial FOV scanner could benefit routine clinical care when the high sensitivity is appropriately leveraged, e.g., injecting a lesser activity for pediatric patients or for a radiotracer in limited supply, or faster scans to increase throughput in a busy clinical practice. In addition, studies performed with experimental research radiotracers illustrate the benefits and opportunities from the combination of large axial coverage and high sensitivity. These early studies provide proof of concept for many proposed applications and should help to motivate more vendors to develop long AFOV scanners. It will require many further investigations at many more institutions to demonstrate the full advantages of a long axial FOV PET scanner and to determine the value of the increased benefits relative to the increased cost.

References

1. Surti S, Karp JS. Advances in time-of-flight PET imaging. Phys Med. 2016;32:12–22.
2. Karp JS, et al. Continuous-slice PENN-PET: a positron tomograph with volume imaging capability. J Nucl Med. 1990;31:617–27.
3. Herzog H, et al. NEMA NU2-2001 guided performance evaluation of four siemens ECAT PET scanners. IEEE Trans Nucl Sci. 2004;51:2662–9.
4. Surti S, Werner ME, Karp JS. Study of PET scanner designs using clinical metrics to optimize the scanner axial FOV and crystal thickness. Phys Med Biol. 2013;58:3995–4012.
5. Karp JS, et al. Whole-body PET scanner using curve-plate NaI(Tl) detectors. J Nucl Med. 1998;39(5):50.
6. Adam LE, et al. Performance of a whole-body PET scanner using curve-plate NaI(Tl) detectors. J Nucl Med. 2001;42(12):1821–30.
7. Badawi RD, et al. The effect of camera geometry on singles flux, scatter fraction and trues and randoms sensitivity for cylindrical 3D PET – a simulation study. IEEE Trans Nucl Sci. 2000;47(3):1228–32.
8. Eriksson L, et al. An investigation of sensitivity limits in PET scanners. Nucl Instrum Methods Phys Res A. 2007;580(2):836–42.
9. Hunter WCJ, et al. Parametric design study of a long axial field-of-view PET scanner using a block-detector tomograph simulation of a cylindrical phantom. In: IEEE nuclear science symposium and medical imaging conference. Orlando; 2009.
10. MacDonald LR, et al. Effective count rates for PET scanners with reduced and extended axial field of view. Phys Med Biol. 2011;56(12):3629–43.
11. Eriksson L, et al. Towards sub-minute PET examination times. IEEE Trans Nucl Sci. 2011;58(1):76–81.
12. Poon JK, et al. Optimal whole-body PET scanner configurations for different volumes of LSO scintillator: a simulation study. Phys Med Biol. 2012;57(13):4077–94.
13. Watanabe M, et al. A high-throughput whole-body PET scanner using flat panel PS-PMTs. IEEE Trans Nucl Sci. 2004;51(3):796–800.
14. Conti M, et al. Performance of a high sensitivity PET scanner based on LSO panel detectors. IEEE Trans Nucl Sci. 2006;53(3):1136–42.
15. Badawi RD, et al. First human imaging studies with the EXPLORER total-body PET scanner∗. J Nucl Med. 2019;60(3):299–303.
16. Karp JS, et al. PennPET Explorer: design and preliminary performance of a whole-body imager. J Nucl Med. 2020;61:136–43. https://doi.org/10.2967/jnumed.119.229997.
17. Pantel AR, et al. PennPET Explorer: human imaging on a whole-body imager. J Nucl Med. 2020;61:144–51. https://doi.org/10.2967/jnumed.119.231845.
18. Cherry SR, et al. Total-body imaging: transforming the role of positron emission tomography. Sci Transl Med. 2017;9(381):eaaf6169.
19. Karp JS, et al. Total-body PET: a “holistic” approach to molecular imaging. In: PET COE Newsletter. Society of Nuclear Medicine & Molecular Imaging; 2019.
20. Zhang Y, Wong WH. System design studies for a low-cost high-resolution BGO PET with 1-meter axial field of view. J Nucl Med. 2017;58(supplement 1):221.
21. Brunner SE, Schaart DR. BGO as a hybrid scintillator/Cherenkov radiator for cost-effective time-of-flight PET. Phys Med Biol. 2017;62(11):4421–39.
22. Brunner SE, et al. Studies on the Cherenkov effect for improved time resolution of TOF-PET. IEEE Trans Nucl Sci. 2014;61:443–7.
23. Kwon SI, et al. Bismuth germanate coupled to near ultraviolet silicon photomultipliers for time-of-flight PET. Phys Med Biol. 2016;61:L38.
24. Moskal P, et al. Time resolution of the plastic scintillator strips with matrix photomultiplier readout for J-PET tomograph. Phys Med Biol. 2016;61(5):2025–47.
25. Yamaya T, et al. A proposal of an open PET geometry. Phys Med Biol. 2008;53:757–73.

26. Zhang J, Knopp MI, Knopp MV. Sparse detector configuration in SiPM digital photon counting PET: a feasibility study. Mol Imaging Biol. 2019;21(3):447–53.
27. Karakatsanis NA, Zein SA, Nehmeh SA. Evaluation of image quality and quantitation in a clinical pet scanner with a uniformly sparse detector rings configuration. In: 2018 IEEE nuclear science symposium and medical imaging conference proceedings (NSS/MIC); 2018.
28. Vandenberghe S, et al. PET 20.0: a cost-efficient, 2 mm spatial resolution total body PET with point sensitivity up to 22% and adaptive axial FOV of maximum 2.00 m. Eur J Nucl Med Mol Imaging. 2017;44(Suppl 2):S305.
29. Zhang Z, et al. Preliminary investigation of optimization-based image reconstruction for TOF PET with sparse configurations. In: Fully three-dimensional image reconstruction in radiology and nuclear medicine, vol. 11072. SPIE; 2019.
30. Daube-Witherspoon ME, et al. Reconstruction performance for long axial field-of-view PET scanners with large axial gaps. In: Fully three-dimensional image reconstruction in radiology and nuclear medicine, vol. 11072. SPIE; 2019.

Index

J. Zhang, M. V. Knopp (eds.), *Advances in PET*,
https://doi.org/10.1007/978-3-030-43040-5